#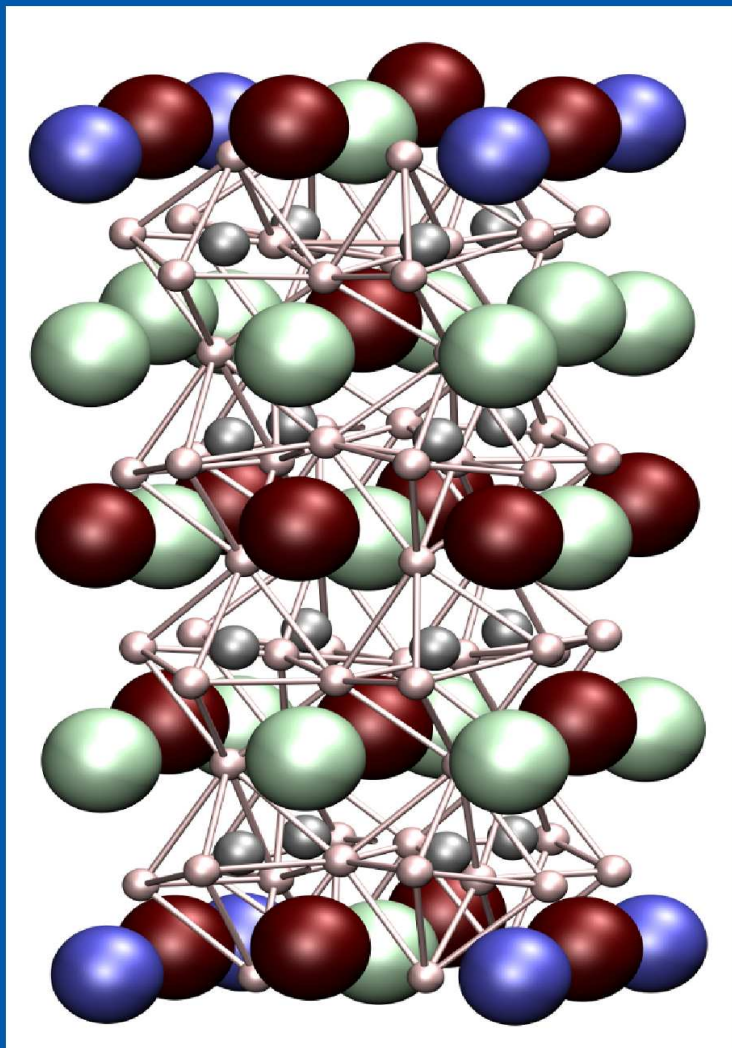 First-principles calculations on the structural and thermodynamic stability of $(Na_{1/2}Bi_{1/2},Ba)TiO_3$ and $Pb(Zr,Ti)O_3$

TECHNISCHE
UNIVERSITÄT
DARMSTADT

Material- und Geowissenschaften
Materialwissenschaften

First-principles calculations on the structural and thermodynamic stability of $(Na_{1/2}Bi_{1/2},Ba)TiO_3$ and $Pb(Zr,Ti)O_3$

First-principles Untersuchungen zur strukturellen und thermodynamischen Stabilität von $(Na_{1/2}Bi_{1/2},Ba)TiO_3$ und $Pb(Zr,Ti)O_3$

Genehmigte Dissertation von Dipl.-Ing. Silke Hayn aus Darmstadt, geboren am 27.6.1983

1. Gutachten: Prof. Dr. Karsten Albe
2. Gutachten: Prof. Dr. Jürgen Rödel

Tag der Einreichung: 29. Oktober 2012
Tag der Prüfung: 11. Februar 2013

Darmstadt — D 17
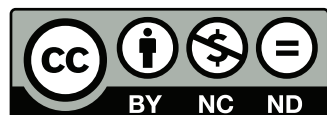
Titelbild: Modell der relaxierten F1E123 Struktur von BNT6BT (siehe Kapitel 4).

Für meine Mutter

Contents

List of Figures

Abstract

Piezoelectric materials couple polarization P_α and mechanical strain $\epsilon_{\beta\delta}$ [1]. The technologically most used piezoelectric material system is the ferroelectric $PbZr_{1-x}Ti_xO_3$ (PZT) [2,3]. Due to the toxicity of lead oxide, and to obtain properties beyond the range of PZT [2], such as a higher temperature of depolarization, larger Young's modulus or higher cohesive stress, current research on ferroelectric materials devotes large resources to the identification of new lead-free materials [3].

The aim of this thesis is to improve the understanding of lead-free ferroelectric perovskite materials and eventually to guide the search for new ferroelectric materials. This is done by analyzing the structure and thermodynamic stability of different ferroelectric perovskite materials, focusing on PZT as reference and $(Na_{1/2}Bi_{1/2}TiO_3)_{1-x}$-$(BaTiO_3)_x$ (BNT-BT). Ferroelectricity is an intrinsic material property that occurs only in materials with certain crystal structures [1]. Therefore, atomistic simulations are an appropriate tool to analyze ferroelectric materials. In this thesis the structure and thermodynamic stability of different ferroelectric perovskites are analyzed based on density functional theory (DFT) calculations.

As a first step chemical ordering and its influence on relaxation is analyzed. Chapter 3 shows that although chemical ordering is preferred in thermodynamic equilibrium for PZT, the driving force is too small to overcome diffusion barriers in bulk materials. In Chapter 4 a combination of DFT calculation and high resolution transmission electron microscopy (HRTEM) is used to analyze the cation distribution in BNT-BT. Finally, the solid solution BNT-BT is modeled according to the atomic distribution found in Chapter 4, and cation displacement is used as a measure of ferroelectricity. It is found, that the instabilities of the cation sites are a bilinear function of lattice parameter and composition. Also traits of the region showing improved ferroelectric properties are identified.

CHAPTER 1

Introduction

This chapter starts with a brief introduction of ferroelectric materials and their theoretical description. Afterwards an overview of the literature on ferroelectric materials and their simulation is given. The chapter is concluded by a section summarizing the open questions that will be analyzed in this thesis.

1.1 Physical Background

1.1.1 Polarization and ferroelectricity

Dielectric materials can be polarized by an electric field. Changes in polarization are measured by the permittivity tensor χ,

$$\chi_{\alpha\beta} = \frac{dP_\alpha}{dE_\beta} \, ,\tag{1.1}$$

where dP_α denotes the change of the polarization vector and dE_β the change of the electric field vector [1]. In addition to the polarization induced by an electric field, materials can also show spontaneous polarization if the structure does not have a center of symmetry and its centers of positive and negative charge do not coincide [4]. Spontaneous polarization is expressed in reference to the centrosymmetric structure by the following equation,

$$P_{\text{eff}} = \int_0^1 d\lambda \frac{dP}{d\lambda} \, ,\tag{1.2}$$

where λ is a dimensionless adiabatic time, P the polarization and P_{eff} the effective polarization [5]. The value $\lambda = 0$ describes the centrosymmetric reference state while $\lambda = 1$ identifies the polarized state. If two energetically equivalent polarized states exist, the material can be switched between these by an electric field. A material that shows switchable spontaneous polarization is a ferroelectric material.

All ferroelectric materials are also piezoelectric in the poled state [4]. Due to the piezoelectric effect mechanical strain results in a change of polarization. If the application of an electric field results in mechanical strain, the behavior is called the inverse piezoelectric-effect. In piezoelectric materials polarization P_α and mechanical strain $\epsilon_{\beta\delta}$ are coupled via the piezoelectric tensor $\gamma_{\alpha\beta\delta}$ [1]:

$$\gamma_{\alpha\beta\delta} = \frac{dP_\alpha}{d\epsilon_{\beta\delta}} \, .\tag{1.3}$$

The ferroelectric properties of a material are directly connected to its crystal structure [1]. The appearance of ferroelectricity can be seen as a disruption of a paraelectric centrosymmetric structure [6].

In Figure 1.1 a centrosymmetric structure and possible disturbances of this structure can be seen. The most left picture represents a prototypic centrosymmetric structure. The structure is built from elements represented by A. The atoms are in average on positions represented by circles. The structure has lattice parameters represented by the frame. In subfigure (b) some average atomic positions are displaced (represented by arrows). In subfigure (c) the lattice parameters of the structure are
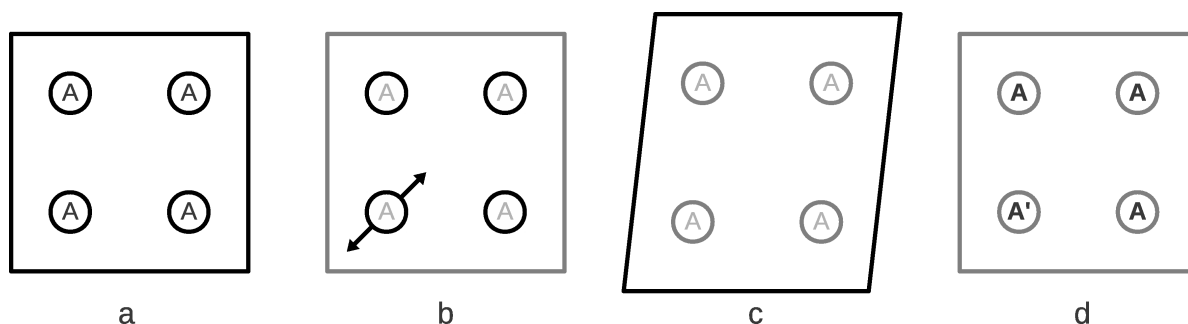
Figure 1.1: *Schematic representing possible distortions of a centrosymmetric prototype structure.*

changed (represented by the distorted frame). In subfigure (d) chemical distribution disrupts the structure (represented by an inhomogeneous distribution of different types of elements A and A'). The displacement of the average atom position seen in subfigure (b) can lead to a spontaneous polarization [1]. Changes of the lattice parameters are very often observed together with a ferroelectric displacement [6]. A displaced atom position can favor a change in lattice constants, as can changes in lattice constant favor the displacement of an atom position. Chemical order on its own can result in ferroelectricity, but also influences atomic displacement and lattice parameters [7]. On the other hand a change in lattice parameters and atomic displacement can result in the favoring of a specific ordering. Atomistic simulations can be used to analyze these disturbances as a whole or individually while keeping other disturbances fixed.

For more details please see the the book chapter by Resta and Vanderbilt [1] and the review article by Dove [6] and references therein.

1.1.2 Distortions in the perovskite structure

The perovskite crystal structure

Ferroelectricity can be observed in non-centrosymmetric crystal structures. An important structure is the distorted perovskite. Technically used ferroelectrics and most new ferroelectric materials exhibit this structure type [3,8].

The perovskite structure can be adopted by oxides of the composition ABO_3, where A and B denote different cations while O stands for oxygen. The symmetry of the ideal prototype structure shown in Figure 1.2 is $Pm\bar{3}m$. The A-atom of the ABO_3 formula unit is positioned at the corner of the unit cell, the B-atom is positioned at the body center of the unit cell and the oxygen atoms are situated at the face centers of the unit cell [8]. Therefore, the B-site cation is coordinated by 6 oxide ions
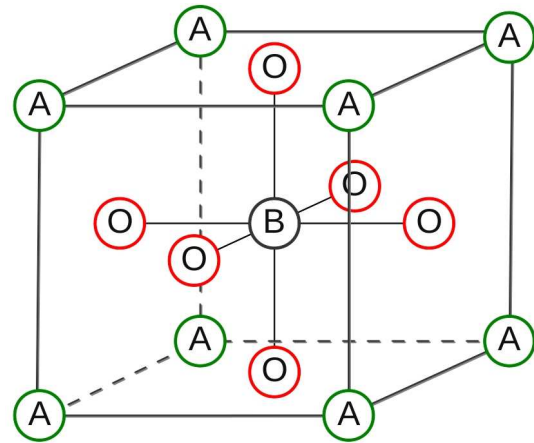
Figure 1.2: *The ABO$_3$ perovskite structure.*

forming an octahedron. The nearest neighbors of the A-site cation are also oxide ions but the coordination polyhedron is a cuboctahedron formed by 12 oxygen anions. The A-site allows for the occupation with larger cations than the B-site. The ideal prototype structure is cubic, centrosymmetric and paraelectric.

The Goldschmidt tolerance factor considers the cubic perovskite structure built from atoms in the rigid spherical atom model. It is calculated from the atomic radii of the perovskite structure,

$$t = \frac{r_A + r_O}{\sqrt{2}(r_B + r_O)} \ , \tag{1.4}$$

where r_A denotes the radius of the A-site cation, r_B the radius of the B-site cation and r_O the radius of the oxygen anion [9]. A perovskite material that shows a tolerance factor of 1 is closely packed in the rigid spherical atom model.

The ferroelectric phase transition

A possible distortion of a prototype centrosymmetric structure is a displacement of the average atomic positions. In the perovskite structure the tolerance factor shown in equation 1.4 can be used as a first assessment of atomic displacements [9].

In a pure material with a tolerance factor of 1 the cubic structure is expected to be stable. If the tolerance factor deviates from 1, but stays in the interval between 0.88 and 1.09, non-cubic perovskite structures occur, but the cubic structure is unstable. A tolerance factor of larger than 1 can be interpreted in the way that in the cubic structure the B-site cation is too small for the space inside the oxygen octahedra. Therefore, the B-site cation has the possibility to displace. A tolerance factor smaller than 1 indicates that the A-site cation has too much space in its coordination poly-hedron. Thus, the A-site cation can displace.

Together with a displacement of the average atomic position, a change in lattice parameters is often observed in ferroelectric perovskites [8]. A material with a tol-

erance factor of larger than 1 is often tetragonal. A displacement of the B-site cation relative to the oxygen atoms along the c-axis results in a strengthening of one B-O bond stabilizing the structure. In addition an elongation of the c-axis relative to the other axis is often observed [8]. A material with a tolerance factor smaller than 1 is often rhombohedrally distorted. Displacement of the A-site cation is seen along the $\langle 111 \rangle$ direction, while the unit cell is elongated along this direction. In addition, tilting of the oxygen octahedra reduces the space for the A-site cation [8].

Materials of the distorted perovskite structure usually undergo a temperature dependent paraelectric-ferroelectric phase transition [8]. Above the transition temperature the average structure is cubic with all atoms in average on their high symmetric sites. Below the transition temperature the structure is distorted and some atomic positions are in average displaced from their high symmetric sites. The displaced atoms are located in a double well potential.

The shape of the double well potential and interaction between neighboring atoms determines the character of the paraelectric-ferroelectric phase transition [6,10]. If the potential barrier is much higher than the atomic interaction one speaks of the order-disorder limit [4,6]. At high temperatures the atoms reside in one or the other of the wells with random occupation. At lower temperatures the atoms prefer to occupy the same side of the double well potential. This type of phase transition can be described by the spin-$\frac{1}{2}$ Ising model [6,11].

In the displacive limit the forces between atoms are much larger than the forces due to the local potential [4,6]. At high temperatures the atoms show thermal vibration about the high symmetric position. Upon cooling, the average position of each atom moves away from the high symmetric position. This type of transition can be described by the Landau theory [6,12].

The temperature dependent paraelectric-ferroelectric phase transition in perovskite materials is considered to be a mixture of a disorder-order and displacive phase transition [6]. An example for a mostly order-disorder phase transition is $BaTiO_3$ [6,13], while the transition of $PbTiO_3$ is mostly displacive [6,14]. In atomistic simulation the displacive character can be modeled in a small cell size. For the disorder-order character of the phase transition different distributions are needed that have to be modeled in larger cells.

A phase transition from a paraelectric to a ferroelectric phase can also be observed upon volume changes in addition to changes in temperature. Average atomic displacements, their amplitude and appearance, are connected to the "space" the atoms have. Calculations of ferroelectric materials show that the potential barrier between the wells is diminished at lower volumes [15]. Early experimental studies of ferroelectric properties support these calculations, they suggested that ferroelectricity is diminished under pressure [16].

The morphotropic phase boundary

Ferroelectricity occurs when the average atomic position of the atoms is displaced from their position in the centrosymmetric structure [6]. It is possible that increased ferroelectricity is observed if more atoms contribute to ferroelectricity. Based on the tolerance factor [9] either the A-site or the B-site cation of a perovskite material can displace. However, in solid solutions of materials with different tolerance factors more atoms might contribute to the ferroelectricity [8].

In the technologically most used ferroelectric material $PbZr_{1-x}Ti_xO_3$ (PZT), $PbTiO_3$ with a tolerance factor larger than 1 is mixed with $PbZrO_3$ with a tolerance factor smaller than 1. In the resulting solid solution a so called morphotropic phase boundary (MPB) separates the $PbZrO_3$ rich rhombohedral phase and the $PbTiO_3$ rich tetragonal phase. Close to this boundary the piezoelectric properties are improved, as the piezoelectric constant shows a peak [2]. Similar boundaries are observed in other piezoelectric materials [3,8]. Originally, the phase boundary was called morphotropic as a structural change occurs with a concentration change [8]. However, in current literature the name MPB is also used to denote a general boundary between a ferroelectric and a second (not necessarily ferroelectric) phase, if that boundary shows improved piezoelectric properties [17].

The improved piezoelectric properties have been explained by means of possible polarization directions in different crystal structures [8]. It has been postulated that at the MPB tetragonal and rhombohedral structures coexist [18–20]. In the ferroelectric phases the cations (A,B) are displaced in reference to the anions (O) creating a polarization. In the tetragonal structure displacement occurs along the $\langle 100 \rangle$ direction. In the rhombohedral structure displacement is observed along the $\langle 111 \rangle$ direction. Therefore, the polarization vector can take six possible directions in the tetragonal structure and eight possible directions in the rhombohedral structure. Thus, the polarization vector can take a total of 14 directions at the MPB [8]. Due to the increased number of directions more grains of a piezoelectric device are able to adopt a polarization close to an overall electrical field. Thus, the effective polarization is increased [8].

Another possible explanation of the improved properties is that at the MPB an electric field can easily induce a phase transition between the rhombohedral and the tetragonal phase associated to a large strain [21]. A miniaturization of ferroelectric domains could occur close to the MPB, also allowing for more grains to contribute to the effective polarization [20]. The most recent theory proposes that the enhanced piezoelectric properties observed at the MPB are associated with a free-energy flattening due to easy paths of polarization rotation and extension [22].

The position of the MPB is pressure dependent [16,23]. It was proposed that the substitution of differently sized cations induces a "chemical" pressure (positive or negative) in the material, which is comparable to a hydrostatic pressure [24].

Chemical order on the cation sublattices

The ideal perovskite structure can be adopted by materials that can be described by the formula unit ABO_3. For materials in which one crystallographic site is occupied by different cations the site occupation can result in chemical ordering. Different ordering might be preferred, depending on the mixed crystallographic site [7,25]. In experiments and calculations, B-site order is seen most commonly in aliovalent solid solutions [26–30]. A-site order is rarer observed than B-site order [7,25,31].

Density functional theory (DFT) calculations find huge barriers for cation site vacancy migration (7.73 eV for Mn in $LaMnO_3$, 9.84 eV for Ti in $BaTiO_3$ and 5.82-6.00 eV for Ba in $BaTiO_3$) [32,33]. Based on these calculations, it is assumed that diffusion in perovskites is kinetically hindered, and thus, can be considered negligible below the Curie temperature. Perovskite ceramics are mostly processed at elevated temperatures [34]. At these temperatures the perovskite forms in the cubic structure and transforms to ferroelectric structures upon cooling. Cation distributions installed above the Curie temperature in the prototypical cubic structure will thus be relevant for material composition and structure in the ferroelectric regime.

A driving force towards chemical order can exist, if the same crystallographic site is occupied by cations that are considerably different in charge, size or electron configuration.

The perovskite structure (shown in Figure 1.2) can be divided into an A-site, B-site and O-site sublattice. For the ideal cubic structure, the A-site sublattice is cubic primitive, as is the B-site sublattice. The O-site sublattice is cubic face centered. In mixed perovskites one or more of these sublattices can be occupied by different atoms. The behavior of lattices is mostly influenced by long range effects, for example differently charged atoms [35]. Charged lattices result in a Coulomb energy favoring a homogeneous distribution of the differently charged atoms [25].

In addition to the long range effects of lattices, the local environment also influences atomic distribution. The local symmetry of an atom strongly influences the possibilities of the atom to displace. It is determined by the position of the surrounding atoms and their properties such as charge, size and chemical bonding. For understanding the influence of local environments in the perovskite structure, it is helpful to have a closer look at the oxygen environment [7,25].

In the ideal perovskite structure the oxygen anion is situated in the center of a flattened octahedron formed by four A atoms in one plane and two B atoms on opposite sites of that plane (see Figure 1.3). In B-site mixed solid solutions the four A-sites are occupied by the same cation, while the B-sites can be occupied by cations of the same or different type. If the B-sites are occupied by the same element, the oxygen environment is centrosymmetric, and thus, without relaxation possibilities. If the B-sites are occupied by two different elements the oxide ion might relax towards the smaller or more positively charged ion [7,25].

(a) 2A/2A′(trans) (b) 2A/2A′(cis)
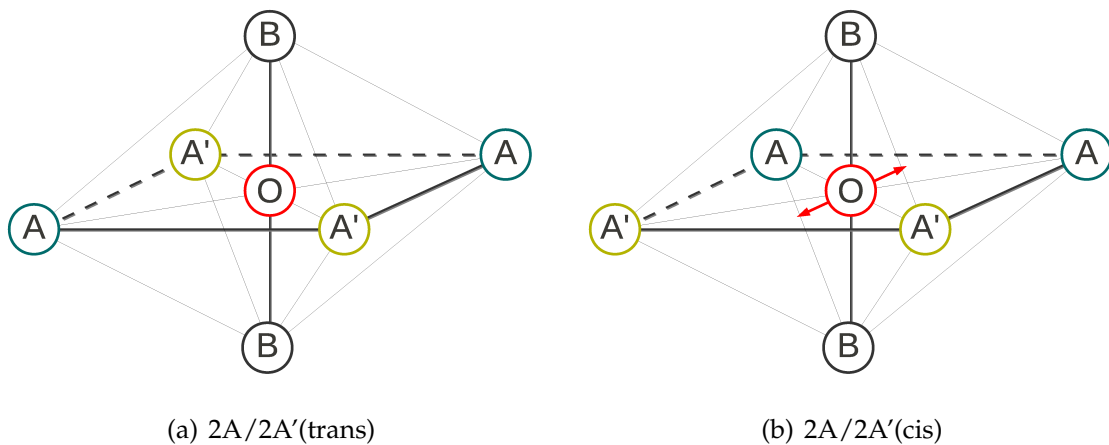
Figure 1.3: *Oxygen environment in the ABO$_3$ perovskite structure. Two occupations in an A-site mixture are shown.*

In A-site mixed perovskites the B-site cations next to the oxygen atoms are the same, while the occupation of the four in-plane A-sites can vary. The number of possible oxygen environments in A-site mixed perovskites is larger than in B-site mixed perovskites. In Figure 1.3 two possible occupations are displayed. Subfigure (a) shows a centrosymmetric environment with no displacement possibilities for the oxygen anion. The oxygen environment shown in subfigure (b) is not centrosymmetric, the oxygen anion could displace toward the A′ or A rich face if either atom type is preferred. The displacement possibilities of all atoms are influenced by their local symmetry. This is not only valid for the anions, for which it was exemplary shown in this paragraph, but also for the cations.

In ferroelectric materials long range and local effects might favor the same type of order, or different types. Which type of order is preferred depends on the crystallographic site that is occupied by different atom types and on the properties of the atom types mixed [7,25].

For more details please see the book by Jaffe [8], the review article by Dove [6], the articles by Knapp [7] and King [25] and references therein.

1.1.3 Landau theory and lattice dynamics

The Landau theory is a mathematical formalism that is used to describe phase transitions. It can be used to describe the displacive paraelectric to ferroelectric phase transitions as a function of temperature [6].

In this theory a phase transition is characterized by a parameter called the order parameter. The order parameter has to contain all information about the degree of order or extent of deformation in the low-temperature phase [6,10,12]. For ferroelectric materials the polarization is mostly used as order parameter [6]. According to the theory, the free energy of a system close to a phase transition can be expressed as a low order Taylor expansion in terms of the order parameter and terms that couple the order parameter with other physical quantities. The expression is truncated at the lowest order that is theoretical possible. Thus, the Gibbs free Energy reads as follows:

$$G(\eta) = G_0 + \frac{1}{2}\alpha\eta^2 + \frac{1}{4}\beta\eta^4 + \frac{1}{2}\zeta\epsilon\eta^n + \frac{1}{2}\epsilon^2 \, , \tag{1.5}$$

With G the free energy, η the order parameter, G_0 the free energy of the system for $\eta = 0$, ϵ the strain, α, β, ζ and C constants, n equals 1 or 2 depending on the symmetry of the strain in relation to the order parameter [6]. In this equation the first three terms stem from the Taylor expansion truncated after the fourth order term, the last two are strain variables. For a phase transition to occur the parameter α has to change sign [6].

For investigating the displacive character of a phase transition, soft modes in the phonon dispersion can be used [6]. The central idea of the soft mode theory is that in the high-temperature phase there is a lattice vibration for which the frequency falls to zero on cooling towards the transition temperature [6,10]. A vanishing frequency implies a vanishing restoring force against the corresponding deformation. Thus, this vibration is called a soft mode. The atomic displacements associated to the soft mode are the same as the deformation of the structure in the low temperature phase [6,36].

DFT calculations can be used to study the phonon dispersion of the perovskite structure [37–41]. Such and similar lattice dynamic calculations [42,43] can be used to obtain a Landau description for the analyzed system. The use of lattice dynamic calculations to discern the stability of the cubic perovskite structure is further elaborated in the methodology chapter (Chapter 2).

For more details please see the review article by Dove [6] and references therein.

1.2 Piezoelectric materials

Piezoelectric materials used in technological applications are often solid solutions of perovskite materials [3,8]. It is common to use acronyms as names for their chemical formula like $PbZr_{1-x}Ti_xO_3$ (PZT). In this thesis the used chemical formula are

according to the IUPAC rules, while the used acronyms are those most commonly used in the Sonderforschungsbereich SFB 595 "Electrical Fatigue in Functional Materials".

The technologically most used piezoelectric material system is PZT [2,3]. It can be found in various applications such as actuators and sensors. Examples of ferroelectrics in applications are: atomic microscopes, ultrasound generators, piezoelectric motors, ink-jet printers and fuel injectors [44].

Current research on ferroelectric materials devotes large resources to the identification of new lead-free ferroelectric materials [3]. This is in part due to the toxicity of lead oxide, a main component of PZT [45]. Lead-free alternatives reduce the risks during production, while also opening up the field of bio-applications to ferroelectric materials. Moreover, there is an interest in materials with properties beyond the range of PZT [2], such as a higher temperature of depolarization, larger Young's modulus or higher cohesive stresses (see [3] and references therein).

To discover new materials with properties that are comparable to PZT or that surpass it, a thorough understanding of why the material shows its piezoelectric properties is needed. In the following an overview of the existing literature on PZT is given and questions that remain open are pointed out. Afterwards the literature on one lead-free alternative $(Na_{1/2}Bi_{1/2}TiO_3)_{1-x}$-$(BaTiO_3)_x$ (BNT-BT) is presented. The last part of this Literature overview covers studies aiming to predict material compositions with improved ferroelectric properties.

1.2.1 Lead zirconate titanate

PZT is a solid solution of A-site active $PbZrO_3$ [43] and A and B-site active $PbTiO_3$ [2,43]. Figure 1.4 shows the quasi-binary phase diagram proposed by Jaffe [8]. Above the Curie temperature the structure is a paraelectric cubic perovskite, while distorted perovskite structures are observed below the Curie temperature. $PbTiO_3$ and the titanium rich phase show tetragonal ferroelectric distortion up to about $55\%PbZrO_3$ content. Pure $PbZrO_3$ is orthorhombic and antiferroelectric. In the solid solution with $PbTiO_3$ it becomes ferroelectric and rhombohedrally distorted up to a concentration of about $45\%PbTiO_3$ [8].

The rhombohedral and tetragonal phases are separated by the so called morphotropic phase boundary (MPB). Close to this boundary the piezoelectric properties are improved, as the piezoelectric constant shows a peak [2]. Concentrations close to the MPB have been in the focus of diffraction studies for many years. The existence of a coexistence region [18,19], a monoclinic phase [46,47] or nanodomains [20] have been postulated. Until now the exact structure in the morphotropic region remains a matter of discussion [48–51].
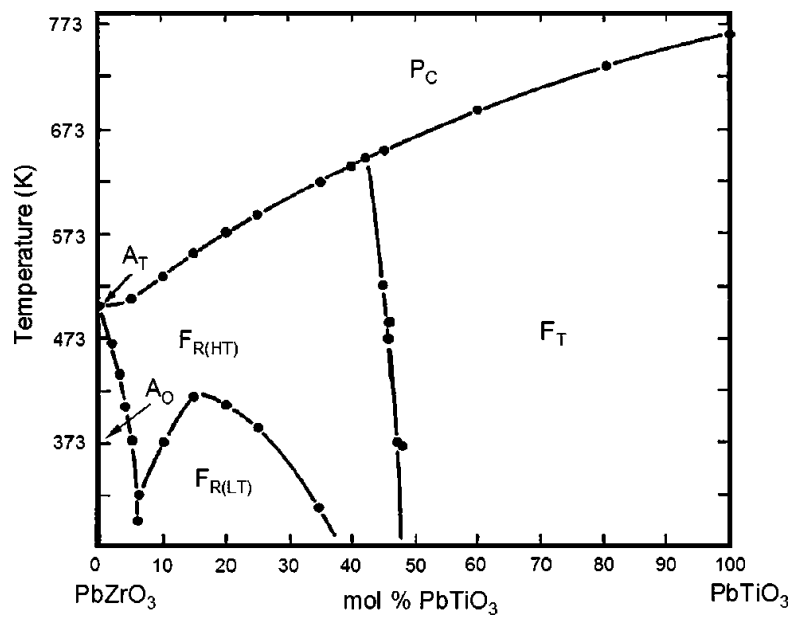
Figure 1.4: *Technical phase diagram of PZT. Reprinted with the permission from Appl. Phys. Lett., **88** 072912. Copyright 2006 American Institute of Physics.*

The position of the MPB and appearance of ferroelectricity is pressure dependent. Studies on Zr-rich PZT showed that the phase transition from the ferroelectric phase to the paraelectric cubic phase results in a volume decrease and can be triggered by the application of pressure [16,23]. More recent studies proposed that compositional changes can be thought of as applying pressure to the material [52]. It is proposed that the substitution of differently sized cations induces a "chemical" pressure (positive or negative) in the material comparable to a hydrostatic pressure [24]. Recent analysis of the high pressure behavior of $PbTiO_3$ showed an initial decrease of tetragonality with increasing pressure, followed by an increase of tetragonality at even higher pressures [53]. This has led to the proposition of "electronic" high pressure (more than 30 GPa) ferroelectricity. Theoretical studies proposed a pressure induced "MPB" in $PbTiO_3$ [54] that is "brought down" to ambient pressure in PZT due to the "chemical pressure" induced by Zr [17]. However, this interpretation was questioned, as the high pressure behavior of $PbTiO_3$ was discovered to be more complex [55].

The PZT solid solution is a homovalent B-site mixed perovskite. Ti and Zr atoms are generally considered to be randomly distributed in PZT, due to the cations identical oxidation states [29]. However, experimental and theoretical studies have found contradicting results. An experimental study on epitaxial thin films of $PbZr_{0.2}Ti_{0.8}O_3$ observed a preference of {110} B-site planes that are solely occupied by titanium [56]. The authors attribute this cation ordering to substrate-film-interactions. First-principles calculations on the thermodynamics of PZT found evidence for cation ordering together with negative mixing energies. Sághi-Szabó and Cohen [57] calculated $Pb(Zr_{1/2}Ti_{1/2})O_3$ with B-site cations ordered along the [100] and [111] direc-

tions and found a positive mixing energy for [100] and a negative mixing energy for [111] ordering. This suggests a stabilization of long-range order along the [111] direction. Zinenko and Sofronova performed Monte-Carlo simulations within an ionic-crystal model to study cation ordering [58]. They calculated PZT in different permutations for two concentrations and concluded that ordering only occurs at temperatures below 250 K.

The finding of a negative mixing energy for ordered structures questions the complete solubility shown in the phase diagram by Jaffe. The validity of the phase diagram is further questioned by an experimental study finding that the width and concentration of the MPB is dependent on processing conditions [19]. Bellaiche and coworkers constructed an effective Hamiltonian fitted to structural parameters from virtual crystal approximation (VCA) calculations and identified a monoclinic phase close to the MPB [59]. Based on the same Hamiltonian, it was found that short-range order has an effect on the width of the MPB [60]. The MPB region is wider if clustering occurs, and smaller in rocksalt order. To resolve these discrepancies, it has been proposed [61] to treat the diagram by Jaffe [8] as a technical phase diagram.

Rossetti *et al.* recently proposed an equilibrium phase diagram for PZT [61]. The diagram was computed from a low-order Landau expansion in an approximation of the theory of regular solutions. The authors argue that the phase diagram by Jaffe can only be observed if atomic diffusion is fully frozen and the transformation is diffusionless. According to the contact rule [62] the single-phase fields of the phase diagram must be separated by two-phase regions rather than line boundaries. The equilibrium phase diagram of Rossetti replaces the MPB and paraelectric to ferroelectric transition lines by miscibility gaps. The gaps expand with increasing atomic exchange interaction parameter and decreasing temperatures. From the measured positive heats of formation [63] they derived a regular solution behavior with a positive interaction parameter as first approximation. Using a high enough atomic exchange interaction parameter for the modeling of the phase diagram leads to a miscibility gap that reaches into the paraelectric cubic phase. However, the validity of Rossetti's measured enthalpies of mixing has been questioned by Jacob *et al.* who calculated excess Gibbs energies from derived thermodynamic activities [64]. Their excess Gibbs energies are lower by a factor of 5 than the enthalpies of mixing measured by Rossetti, a discrepancy they deem too high to be resolved by excess entropy of mixing. In addition, they find the cubic solid solution to be intrinsically stable, thus contradicting the immiscibility in this phase.

From the presently available literature on PZT it can be deduced, that - although the material has been under scientific scrutiny for decades - some unexplained aspects and discrepancies remain. Opinions on cation order in PZT deviate. While the B-site occupation is generally considered to be disordered [29], experimental [56] and

theoretical [57,58] studies found indications of order. The phase diagram of PZT in thermodynamic equilibrium is unknown. A model calculation exists that focuses on the phases below the Curie temperature [61]. However, there are indications that thermodynamic equilibrium cannot be reached at these temperatures [32,33]. In addition the model is questioned by another work [64].

The appearance of ferroelectricity and the position of the MPB in PZT is pressure dependent [16,23]. It was proposed that compositional changes can be thought of as applying a "chemical" pressure to the material. However, the pressure behavior of ferroelectric materials is not fully understood [17,53–55].

In this thesis these topics are addressed in Chapters 3 and 5. The PZT system is mainly analyzed in Chapter 3. Cation order is analyzed in cubic PZT, comparing configurations qualitatively in different supercells in Section 3.2 and quantitatively within a specific supercell in Section 3.3. The thermodynamics of cubic PZT are assessed from first-principles to validate the assumption of a fully miscible solid solution with positive heat of mixing in the paraelectric regime in Section 3.4. In Chapter 5 the dependence of ferroelectricity on pressure and its relation to the composition is analyzed on a different material system.

1.2.2 Bismuth sodium titanate - barium titanate

$(Na_{1/2}Bi_{1/2}TiO_3)_{1-x}$-$(BaTiO_3)_x$ (BNT-BT) is the solid solution of tetragonal $BaTiO_3$ with rhombohedral $Na_{1/2}Bi_{1/2}TiO_3$ (BNT) [65]. In comparison to $PbTiO_3$ the tetragonal distortion of $BaTiO_3$ is smaller, as is the piezoelectricity. It is still used as only few tetragonal perovskites have been identified so far [3]. BNT is used as the rhombohedral material of the solid solution, as one of the elements occupying the A-site is bismuth. Bismuth has a similar electronic structure as lead including the so called "lone-pair" that is said to play an important role in lead based ferroelectrics [3].

The structure of the systems is not clearly resolved (see [66] and references therein). BNT was reported to be antiferroelectric by Takenaka [65], but today the peculiarities attributed to antiferroelectricity are considered signs of relaxor behavior [31]. BNT is a rhombohedral ferroelectric with high remanent polarization and high coercive field at room temperature [67,68]. Single crystals showed rhombohedral or pseudocubic symmetry depending on synthesis and stoichiometry [31]. In a recent study on ceramics, formation of tetragonal platelets in a rhombohedral matrix was observed [69]. $BaTiO_3$ is a well known ferroelectric that has been in the focus of experimental and theoretical research [8,70]. At room temperature it is tetragonal and B-site active [43]. $BaTiO_3$ forms a homogeneous solid solution with BNT.

Depending on processing conditions, a morphotropic phase boundary (MPB) in the BNT-BT system is known to exists at concentrations between 0.04 mol% and

0.08 mol% [71–75]. In this composition range, anomalies in X-ray diffraction, dielectric measurements, Raman and infrared spectroscopy were reported [65,71–75]. These anomalies could be due to chemical order. Typically, tetragonal and rhombohedral phases coexist at the MPB, but the presence of a rhombohedral phase and a cubic phase at the MPB was also reported [73]. These compositions show relaxor behavior and they reveal different temperatures for depolarization (T_d) and different maximum dielectric constants (T_m). This provides evidence for the existence of an additional phase between the ferroelectric and paraelectric phase [65,72,75]. The recent work by Jo [66] shows that the structure of the system differs considerably in the unpoled and the poled state, a behavior usually found in relaxors. In addition, the MPB evolves from a boundary in the unpoled sample into a morphotropic region in the poled sample.

In BNT-BT aliovalent cations are located at the A-site (Na^+, Bi^{3+} and Ba^{2+}). In B-site mixed perovskites chemical ordering is observed when a sufficient charge difference between the elements occupying the B-site exists [76]. In A-site mixed perovskites ordering is rarely observed. Knapp, King and Woodward presented that {100} order is preferred in A-site mixed perovskites, but a charge difference of two, as observed in BNT-BT, is not sufficient without additional factors favoring order [7,25]. However, chemical ordering is reported in the BNT-BT system. In BNT a very low degree of long-range order is observed [31]. Other work finds a similar order in nanometer sized domains embedded in a disordered matrix [77].

In a theoretical study based on first-principles calculations and the cluster-expansion method, various permutations of the atomic arrangements in pure BNT [78] were analyzed and an ordered structure with "crisscross" rows of Na and Bi cations perpendicular to [001] and of space group P4_2/mmc was predicted. Another first-principles study [79] presents density functional theory (DFT) calculations on $BaTiO_3$, $Bi_{1/2}Na_{1/2}TiO_3$ and $Bi_{15/32}Na_{15/32}Ba_{1/16}TiO_3$ but only for one ordered permutation of each system without allowing for structural relaxation. X-ray diffraction studies of single crystals suggested the existence of an ordered phase based on a $Bi_{0.4463}Na_{0.4913}Ba_{0.0625}TiO_3$ model [71].

It can be concluded that BNT-BT is a relaxor material that shows promising ferroelectric properties, but its atomic structure is not yet resolved. To increase the knowledge on the BNT-BT system it is analyzed in this thesis using atomistic computer-simulations.

Possible chemical ordering is analyzed for BNT and morphotropic BNT-BT in Chapter 4. The material system is used to analyze the relationship of volume and composition to ferroelectric activity in Chapter 5. In the same chapter also a characteristic of a composition region with improved ferroelectric properties is postulated.

1.2.3 Predicting morphotropic compositions

The prediction of material systems that show a MPB and its composition is one aim of current research. Mixing of tetragonally or rhombohedrally distorted materials is one strategy to mimic the MPB of $PbZr_{1-x}Ti_xO_3$ (PZT).

The tolerance factor

To identify rhombohedrally and tetragonally distorted materials the Goldschmidt tolerance factor (equation 1.4) is often used as a guideline. For example, Eitel *et al.* analyzed various potential counterparts in solid solutions with $PbTiO_3$ [80,81]. The materials $BiMeO_3$, with Me standing for scandium, indium or yttrium, were analyzed as the tolerance factor indicated a possible rhombohedral distortion. A MPB was found in the solution of $PbTiO_3$ with $BiScO_3$. Also a correlation between T_C and the tolerance factor was found. Another work by Suchomel and Davies analyzed $PbTiO_3$-$Bi(B'B'')O_3$ showing a MPB [82]. They observed a correlation of the composition at the MPB with the tolerance factor of the materials.

The tolerance factor has also been used to guide calculations. For example, DFT calculations verified that $BiAlO_3$ is rhombohedral and that $BiGaO_3$ is tetragonal, as indicated by the tolerance factor [83]. Therefore, a solid solution of these materials might be of interest.

Solid solution calculations

The tolerance factor is successfully used as a guide to identify tetragonal and rhombohedral structures that might show a MPB [80–83]. To predict the composition of the MPB, DFT calculations of solid solutions could be used [52,84].

Existing calculations are based on the assumption that the rhombohedral and tetragonal phases coexist at the MPB. Translating this information to DFT calculations means: In solid solution calculations the MPB is positioned at the composition where rhombohedral and tetragonal phases show the same energy [52,84]. As mentioned before the exact structure of PZT at the MPB is unclear. Within the explained assumption, DFT calculations would be able to locate a line boundary as well as a composition within a coexistence region. It might also be possible to gather some hint on the composition region of a monoclinic phase between a rhombohedral and tetragonal phase.

Íñiguez *et al.* performed calculations on solid solutions of $BiScO_3$-$PbTiO_3$ and PZT using the virtual crystal approximation (VCA) [84]. Comparing the energies of the structures they could identify the MPB concentration. Grinberg and Rappe used supercells to calculate solid solutions of $AgNbO_3$ with $PbTiO_3$, $BaTiO_3$ and

BaZrO$_3$ [52]. They used the comparison of different structures to predict the MPB compositions.

In preparation of this thesis the work of Íñiguez *et al.* [84] and Grinberg and Rappe [52] was repeated for PZT in order to validate and benchmark the computational framework. The simulations could be reasonably well reproduced. The MPB is predicted with an accuracy of 1-12 mol% which is comparable to the accuracy of the work by Íñiguez *et al.* [84] who predict the MPB with an accuracy of 10%. During this benchmarking process it came apparent that the predicted MPB strongly depends on the choice of parameters that influence the ferroelectricity of a material like the volume, symmetry and relaxation.

Combination of experimental studies and DFT calculations

A major work by Grinberg *et al.* [85] combines experimental findings correlated to the tolerance factor and DFT solid solution calculations. They analyzed solid solutions of PbTiO$_3$ with (Pb/Bi)BO$_3$, B standing for different B-site cations.

PbTiO$_3$ is seen as the tetragonal partner in the solid solution showing a collinear displacement of lead atoms. Adding another perovskite introduces the element B in addition to Ti on the crystallographic B-site. Due to different elements on the B-site, Pb will show a tendency of favorably moving towards one element type, disrupting the collinear displacement of Pb atoms. The driving force away from one B-site cation type is called the Pb-B repulsion and quantified as a function of atomic radii and B-site displacement.

The authors postulate that at the MPB the cost induced by collinear Pb displacement and the Pb-B repulsion are equal. As a zeroth approximation the cost induced by collinear Pb displacement is considered to be constant. Thus, an equation is obtained that calculates the PbTiO$_3$ concentration of the MPB as a function of atomic radii and B-site displacement. The equation is fitted to experimental and DFT data with an accuracy of 15% in the PbTiO$_3$ concentration of the MPB. The fit can be improved by fitting different equations to solid solutions of PbTiO$_3$ with BiBO$_3$ or PbBO$_3$.

The equation obtained by Grinberg *et al.* explains the previously observed qualitative correlation of the MPB concentration to the tolerance factor in PbTiO$_3$-Bi(B′B″)O$_3$ materials [82]: The tolerance factor, which is calculated from atomic radii, approximates the dependence to the atomic radii.

However, the method shows some disadvantages. First, it is not clearly explained how the value for the atomic B-site displacement is chosen. Second, the accuracy of the calculated PbTiO$_3$ concentration of the MPB is not very good. Improving the accuracy narrows the material systems the model can be applied to, while also increasing the necessary input data.

This approach has not yet been transfer to lead-free systems, which might be due to the following obstacles. For example a large amount of input data is necessary, that is not yet accessible for lead-free materials. More importantly, the work is strongly based on the specific behavior of the lead-containing perovskite material $PbTiO_3$. A direct transfer to lead-free materials would be possible if a lead-free material is found that shows similarities to $PbTiO_3$ in the properties used for the model. However, the transfer would only be useful if this material would also be a material connected to perovskite lead-free systems with good piezoelectric properties.

Predictions on lead-free materials

A promising lead-free ferroelectric material system is BNT-BT [65]. It is the solid solution of tetragonal $BaTiO_3$ with rhombohedral BNT, thus, structural traits of PZT are present. It also shows a MPB with improved piezoelectric properties [65]. A literature overview was presented in Section 1.2.2.

Literature that discussed design rules for ferroelectric materials is less extensive for lead-free materials than for lead-containing materials. As for the lead based materials a correlation to the tolerance factor was analyzed. Experimental works on BNT based material found a correlation of the MPB composition to the tolerance factor [68,86]. However, the calculated relationship of the structure to the tolerance factor of lead-free perovskites is shown to be non-monotonic [52,87]. Thus, a theoretical explanation of the experimentally observed behavior has not been published yet.

$SnAl_{1/2}Nb_{1/2}O_3$ is proposed as a potential lead-free ferroelectric that might be possible to be synthesized [88]. The position of a potential MPB in a solid solution of this materials is predicted using the $PbTiO_3$ based correlations by Grinberg [85]. However, the validity of that transfer is questionable.

DFT solid solutions calculations to predict the composition of the MPB comparable to the calculations on lead based materials were published for silver solid solutions [52] and $Na_{1-x}K_xNbO_3$ (KNN) [89]. For the silver solid solutions no comparison to experimental data is offered, the work on KNN does not predict the MPB with the best piezoelectric properties. The work on KNN can also be interpreted in the way that parameters influencing the ferroelectricity of a material like chemical ordering, volume and relaxation, severely influence the predicted compositions of the MPB.

Methods to predict the composition of MPB have been developed for lead-based materials [52,84,85], but a transfer to lead-free materials has not yet been fully successful [87,89]. Experimental studies on lead-based materials find a monotonic relationship of the materials structure to the tolerance factor, that is explained by theoretical studies [82,85]. Based on these findings predictions of the MPB for lead-based

materials are within an accuracy of 15 % of the experimentally observed compositions [52,84,85]. Theoretical studies on lead-free materials on the other hand show a non-monotonic relationship between the materials structures and the tolerance factor [52,87]. As the tolerance factor is an indication of atomistic parameters it follows that the relationship of the ferroelectric structure to atomistic parameters differs for lead-based and lead-free materials. It is possible that due to this difference a direct transfer of methods predicting the MPB developed for lead-based materials to lead-free materials was not yet successful.

In this thesis the relationship of atomic parameters influencing the structure of lead-based and lead-free materials are analyzed. Chemical ordering and relaxation are analyzed in Chapters 3 and 4 for PZT and BNT-BT respectively. Volume and atomic displacements are analyzed in Chapter 5 for BNT-BT.

1.3 Open questions

In this thesis the structure and thermodynamic stability of $PbZr_{1-x}Ti_xO_3$ (PZT) and $(Na_{1/2}Bi_{1/2}TiO_3)_{1-x}$-$(BaTiO_3)_x$ (BNT-BT) are investigated. From the overview presented in this chapter the following main questions remain open:

- Does PZT show chemical B-site order? Is PZT a fully miscible solid solution?

- Does BNT-BT show chemical A-site order?

- What is the ferroelectric instability in BNT-BT? Can stability calculations of the BNT-BT system be used to narrow the composition region with improved ferroelectric properties?

CHAPTER 2

Methodology

The properties of ferroelectric materials are closely connected to their atomic structure [8]. Therefore, atomistic simulations on many levels of approximation, are an excellent tool to analyze ferroelectric materials. Ferroelectricity occurs because the centrosymmetric structure is unstable and distorts [6], these distortions can be modeled and analyzed separately or as whole [90–94].

In this chapter atomistic material modeling methods used to simulate ferroelectric perovskites are described. The chapter starts with a description of quantum mechanic methods, afterwards classical simulation methods are introduced.

2.1 First-principles calculations

2.1.1 Theory

This subsection is largely based on the review article by Payne *et al.* [95], for more details please see the article and references therein.

In first-principles calculations a solid is treated as a many-body system composed of electrons and nuclei in terms of quantum mechanics, without introducing any empirical parameters. To predict the electronic and geometric structure of a solid, the quantum-mechanical total energy of a system is calculated, and subsequently minimized with respect to the electronic and nuclear coordinates [95].

As the mass of the electron is much smaller than the mass of the nuclei, the response of the electrons to movement of the nuclei can be considered instantaneous. Therefore, the Born-Oppenheimer approximation can be applied to separate the electronic and nuclear coordinates in the many-body wave function [95]. This approximation simplifies the many-body problem, however, further simplifications are used to allow for accurately and efficiently performed total energy calculations.

In this subsection the following simplifications are presented. Firstly, density functional theory (DFT) is presented, which is used to model electron-electron interactions, together with an approximation needed to perform calculations. Afterwards, the importance of periodicity to quantum mechanic calculations is introduced. Finally, interactions with ions are presented.

Density functional theory

The basic concepts of DFT were laid out and proven by Hohenberg and Kohn [96] and Kohn and Sham [97]: The total energy of an electron gas is an unique functional of the electron density, this is also true in the presence of a static external potential. The minimum value of the total energy functional is the ground-state energy of the system. The electron density that yields the minimum value is the exact single-particle ground state density [95,96].

To determine the set of wave functions ψ_i that minimize the Kohn-Sham functional the Kohn-Sham equations are used:

$$\left[\frac{-\hbar^2}{2m} \nabla^2 + V_{\text{ion}}(r) + V_H(r) + V_{XC}(r) \right] \psi_i(r) = \epsilon_i \psi_i(r) \, , \qquad (2.1)$$

with ψ_i the wave function of electronic state i, ϵ_i the Kohn-Sham eigenvalue and *r* the electronic coordinates. The static electron-ion potential V_{ion} and the Hartree potential V_H can be calculated exact. The exchange-correlation potential V_{XC} is not known precisely, it is a measure of interaction between electrons [95,97]. The equations

represent a mapping of the interacting many-electron system onto a system of non-interacting electrons moving in an effective potential due to all the other electrons [95].

The Kohn-Sham equations are solved self-consistently. The occupied electronic states have to generate a charge density that produces the electronic potential that was used to construct the equations. Thus, it is formally possible to replace the many-electron problem by an equivalent set of self-consistent one-electron equations. However, the exchange-correlation potential V_{XC} has to be approximated [95,97].

The simplest approach to approximate the exchange correlation functional is the local density approximation (LDA). It is assumed that the exchange correlation energy per electron at point r in the electron gas ($\epsilon_{XC}(r)$) is the same as the exchange correlation energy per electron in a homogeneous gas with the same density as the electron gas at point r [95,97]:

$$\epsilon_{XC}(r) = \epsilon_{XC}^{\mathrm{hom}}[n(r)] \ . \tag{2.2}$$

In the LDA the exchange correlation energy of an electronic system is constructed based on this assumption [95,97].

The LDA assumes that the exchange correlation energy is purely local [95]. Another approximation is the generalized gradient approximation (GGA) [98]. It is also local but compared to the LDA it additionally takes into account the gradient of the electronic density at coordinate r [98].

Periodicity

With the before mentioned simplifications it is possible to separate the electronic coordinates from the ionic coordinates, and map the many-body problem onto a set of single-particle equations [95]. However, an infinite number of non interacting electrons moving in the potential of an infinite number of ions remains to be considered. Therefore, DFT calculations of solid state focus on periodic systems [95].

In a periodic system only a finite number of electrons have to be considered. Additionally Bloch's theorem can be used. Bloch's theorem states that in a periodic solid electronic wave functions can be written as the product of a cell-periodic part and a wavelike part [4,95]. The cell periodic part of the wave function can be expanded by using a basis set consisting of a discrete set of plane-waves whose wave vectors are reciprocal lattice vectors of the crystal $\vec{G}$. Each electronic wave function can be written as a sum of plane-waves [95]:

$$\phi_i(r) = \sum_{\vec{G}} c_{i,\vec{k}+\vec{G}} \exp\left[i(\vec{k}+\vec{G}) \cdot r\right] \ . \tag{2.3}$$

Electronic states are allowed only at a set of k-points determined by the boundary conditions that apply to the bulk solid.

The Bloch theorem changes the problem of calculating an infinite number of wave functions to one of calculating a finite number of electronic wave functions at an infinite number of k-points [95]. However, it is possible to represent the electronic wave functions over a region of k-space by the wave functions at a single k-point. Thus, only a finite number of k-points have to be considered to calculate the electronic potential. The more k-points are considered, the more exact the calculated total energy will be. To reduce the needed calculation time convergence studies are performed to determine the needed number of k-points to represent a system with adequate accuracy.

Bloch's theorem states that the electronic wave functions at each k-point can be expanded in terms of a discrete plane-wave basis set. The coefficients for the plane-waves with small kinetic energy are typically more important than those with large kinetic energy. Thus the plane-wave basis set can be truncated to include only plane-waves that have kinetic energies less than some particular cutoff energy [95]. To determine the required cutoff energy convergence studies are performed.

The usage of Bloch's theorem requires the modeling of periodic systems. However, some interesting effects are non-periodic, such as a single defect of a surface. To still use the mentioned simplifications supercells are often used [95]. A supercell is constructed by using a simulation cell larger than the unit cell. In this supercell the subcells can differ. For example one subcell could hold a defect. Calculating a defect this way means that instead of one single defect an array of defects is modeled [95]. The distance between defects would be determined by the size of the supercell. Supercells will be further discussed on the example of modeling solid solutions.

Interactions with ions

Bloch's theorem states that the electronic wave functions can be expanded using a discrete set of plane-waves. However, a very large number of plane-waves are needed to expand the tightly bound core orbitals. In addition the valance electrons show wave functions that are rapidly oscillating in the core regions. To follow the wave functions a large basis set is needed [95].

The pseudo-potential theory approximates the collective system of nuclei and core electrons by an effective, much smoother, potential [99]. The Kohn-Sham equations are then solved for the valence electrons only. This method reduces the number of wave functions to be calculated, since the pseudo-potentials only have to be calculated and tabulated once for each atom type [99].

A different approach is the augmented-plane-wave method (APW) [99]. The approach divides space into atom-centered augmentation spheres and a bonding region outside the spheres. Inside the augmentation spheres the wave functions are taken as some atom-like partial waves. In the bonding region envelope functions are defined [99].

Mainly used in this thesis is the projector augmented wave (PAW) approach [100]. It is a generalization of the pseudo-potential and the APW approach [99,100].

The ion-ion interaction is calculated electrostatically. Coulomb interaction is long ranged in real-space and in reciprocal space [4]. Thus, to calculate the Coulomb energy of the ionic system is difficult [95]. For periodic lattices a rapidly convergent method was developed by Ewald [4,95]. The infinite summation is replaced by two infinite summations, one over lattice vectors and the other over reciprocal lattice vectors. For appropriate parameters the two summations become rapidly convergent in their respective spaces [4,95].

2.1.2 Application

DFT calculations are used to calculate the eigenenergies E_i of a micro-state i. Input parameter is an initial structure of the analyzed micro-state, given as a simulation cell with periodic boundary conditions. The volume of the micro-state V is given for the simulation cell. The number of particles N is infinity due to the periodic boundary condition, different elements appear in the relation given in the simulation cell. As DFT is a ground state calculation method the temperature of the calculated micro-states is considered to be $0\,\mathrm{K}$.

Based on the simulation cell structure, the potential of the ion cores is constructed by superposition of potentials for different atoms. The electron density is then calculated according to the ion core potential in a scheme of self-consistency until the energetic deviance reaches a predefined limit. The atomic forces are used to calculate new positions for the ion cores in so called ionic steps. This cycle is repeated until a predefined criteria is reached. If either the the atomic forces are below a predefined value, or the energy change differs less than a predefined value the structure is called relaxed and the cycle is stopped [91,101]. The cycle can also be stopped if a preset value of ionic steps is reached. Setting the number of ionic steps to zero means that the energy and the atomic forces of the input structure are calculated but no relaxation is allowed.

As shown in Section 1.1.1 ferroelectricity is connected to distortions of the centrosymmetric prototype structure. Possible distortions are atomic displacement, changes in lattice parameters and change in composition. DFT calculations can be

used to analyze these distortions. Changes in atomic position and lattice parameters are analyzed by either allowing the structure to relax, distorting the structure to analyze the energy change, or distorting the structure and allowing it to relax. The distortion of lattice parameters and atomic position can be analyzed separately or jointly. These distortions are always analyzed in a fixed composition. A varying composition is analyzed in solid solution calculations presented later in this subsection.

The package to perform DFT calculations used in this work is Vienna ab-initio simulation package (VASP) [101]. The VASP code is used as it is very efficient in the calculations of larger systems.

Exchange correlation functional

As mentioned in the theory subsection, DFT calculations rely on an approximation for the exchange correlation functional.

An analysis of different approximations for the exchange correlation functional has been performed for the typical ferroelectric materials $BaTiO_3$ and $PbTiO_3$ (see [102] and references therein). For both materials fully relaxed calculations within the LDA result in a too small volume; the lattice parameter is underestimated by 1-2 %. Relaxed calculations using the GGA [103] to approximate the exchange-correlation functional result in larger volumes. The relaxed volumes of GGA calculations are larger than calculations based on LDA, sometimes they are also larger than the experimental volume. In the case of $PbTiO_3$ the usage of the GGA obtains a so-called "supertetragonal" high-volume phase not observed in experimental studies [102,104].

Both approximations show parameters closer to experimental values if calculations are performed at experimental volume. LDA is usually used for ferroelectric systems, commonly at experimental volume [102]. For this study LDA is preferred, as its error is known and systematic. All calculations presented in this thesis are performed within the LDA, while keeping in mind the underestimation of volume.

Modeling solid solutions

In this thesis materials in which one crystallographic site is occupied by different types of atoms are analyzed. Examples are the pure perovskite materials $Na_{1/2}Bi_{1/2}TiO_3$ (BNT) and solid solutions like $PbZr_{1-x}Ti_xO_3$ (PZT) and $(Na_{1/2}Bi_{1/2}TiO_3)_{1-x}$-$(BaTiO_3)_x$ (BNT-BT). Different approaches exist to model materials where different elements occupy the same crystallographic site. In this thesis the virtual crystal approximation (VCA) [105,106] and the supercell approach are used.

VIRTUAL CRYSTAL APPROXIMATION   In DFT calculations the properties of the elements can be based on pseudo-potentials as input. VCA introduces the idea of using instead of the pseudo-potential of an actual element a pseudo-potential that is generated to approximate the properties of different elements. Thus, the VCA introduces a virtual atom upon which mixing can occur [105–107].

Modeling a specific material is reflected in the input structure of the DFT calculations. In the perovskite structure A, B and oxygen atoms are occurring in the ratio 1:1:3. A simple pure phase perovskite is modeled with a five atom unit cell in which the A-site is occupied by one element, the B-site by another and the O-sites by oxygen. To model a solid solution either the A-site or B-site atom is replaced by a virtual atom. For example, the replacement of the B-site cation would result in the modeling of a B-site mixed perovskite. In such a calculation the virtual atom would be identified by a pseudo-potential that is a mixture of the elements that are supposed to be mixed on this lattice site. To model a solid solution different pseudo-potentials are generated for different compositions. One of these pseudo-potentials is then used together with the pseudo-potentials of the other cation type and the oxygen to define the analyzed system [106]. Using the VCA, compositional changes can be accomplished in a homogeneous atomic distribution. Thus, the VCA can be used to change the composition without distorting the structure.

A disadvantage inherent in the method is that only average properties can be analyzed, but not the local structure [84]. Applications mainly focus on the mixing of homovalent atoms with little differences in atomic radii. It is expected that charge differences and large size differences result in local changes that influence the average structure. An average analysis of the structure might neglect such structural changes [84].

SUPERCELL APPROACH   The other method to calculate materials in which one crystallographic site is occupied by different atoms used in this thesis makes use of supercells [102]. In this approach the number of crystallographic sites is increased. To do so the unit cell is multiplied along the directions of space forming a supercell consisting of subcells. Supercell calculations can be used to assess various topics in DFT calculations for example defects and surfaces. In this subsection only their use for the modeling of solid solutions is explained.

Figure 2.1 shows schematically in two dimensions how a pure phase material is modeled by one unit cell, and a mixed material by a supercell. The cell used for calculations is marked in red, additional atoms are drawn resulting from the periodic boundary conditions.

Transferred to the perovskite structure a supercell is built out of 5 atom subcells, to create more crystallographic sites [102]. If all atomic sites in the supercell are occupied by the same atoms as in the unit cell the same calculation results are
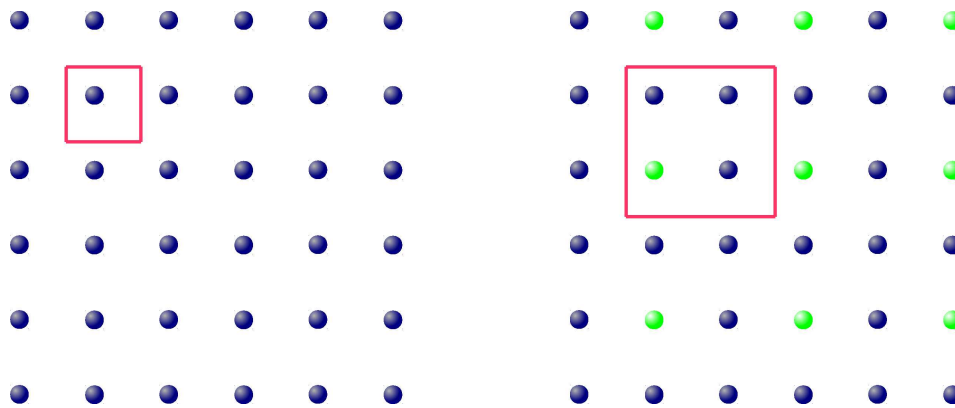
Figure 2.1: *Schematic illustrating the supercell approach. A pure phase material modeled by a unit cell and mixed material modeled by a supercell is shown. The cell used for calculations is marked in red.*

expected. If new properties are observed, for example octahedral tilting, the unit cell of the analyzed phase is larger than the 5 atom cell. To use the supercell to model a perovskite solid solution the cation sites are occupied by different atom types in different subcells. Thus, composition and occupation are variables in the analyzed system. Naturally, the composition can only be changed in steps.

As mentioned in the previous subsection, DFT calculations of solid state rely on the modeling of periodic systems. Supercell calculations model a periodic system. However, the simulation cell is not necessarily the unit cell of the analyzed system. Therefore, the problem of chemical order is introduced. All solid solutions modeled with the supercell approach show chemical ordering. This means that supercell calculations do not model a statistical occupation of crystallographic sites in a solid solution. Additionally, the supercell approach has an effect on the analyzed symmetries. Chemical order imposes a symmetry on the calculated structure. Therefore, selected symmetries can only be calculated in some occupations, different occupations can result in different symmetries.

In first-principles methods the input structure imposes symmetry constraints on the calculations [101,102,108]. Two factors are important: The geometry of the input structure, and the distribution of different elements in a supercell. The geometry of the input structure influences the relaxation possibilities of the calculation due to periodic boundary conditions. In general, a smaller supercell results in more restricted relaxation possibilities. The distribution of elements in the supercell influences the symmetry of the structure. The symmetry of a structure influences its relaxation possibilities. Thus, the site occupation also imposes symmetry constraints. DFT calculations in different symmetry constraints might obtain different structures [101,102,108].

Due to the code's efficiency VASP [101] is used to perform supercell calculations. The supercell approach is used in all result chapters of this thesis.

Frozen phonon calculations

Ferroelectricity appears as the centrosymmetric structure becomes unstable and deforms to ferroelectric active structures. Lattice dynamic calculations of the phonon dispersion in materials can be used to identify a materials resistance against deformation. A disappearing frequency signifies a disappearing restoration force against the corresponding deformation. To perform full phonon dispersion calculations independent distortions are modeled that are used for DFT calculations. According to the symmetry of the analyzed system the results are combined and form the phonon dispersion relation of the material. Such calculations have been published, for example, for $BaTiO_3$ [37–39], $KNbO_3$ [40] and PZT [41].

To gather information about ferroelectric perovskites a simplified phonon analysis is also useful [43]. The ferroelectric distortion is a process involving all atoms of the unit cell. In a simplified manner it can be illustrated as a displacement of one of the cation types from its high symmetry position. As mentioned before the tolerance factor can be used to identify which cation has space to displace in the cubic prototype structure. Calculations displacing the cations give a more accurate picture. Ghita *et al.* performed displacement calculations on $(Pb,Cd)TiO_3$ [42], $BaTiO_3$, $BaZrO_3$, $PbTiO_3$ and $PbZrO_3$ [43]. Based on their calculations they were able to state that a material is ferroelectrically active, and whether it is A-site or B-site active.

2.2 Classical simulation methods

2.2.1 Interatomic potentials

In classical atomistic simulation methods the interaction of atoms in a system are governed by rules. These rules are often expressed in terms of potential functions [93,109]. The potential function describes how the potential energy of a system of atoms depends on the coordinates of the atoms. An equation that does not include any electronic degrees of freedom, where all electronic effects are incorporated in the function, is called interatomic potential [93,109].

The potential functions are generated from theory, quantum mechanic calculations, experiments or a combination of those [93,110,111]. For perovskite ferroelectrics a number of potential parameters have to be optimized intricately for each

new material comparing to experimental results [112]. Interatomic potentials were used for Molecular dynamics (MD) simulations on ferroelectric materials by Tinte *et al.* [113]. Crystal structure, polarization and phase transition sequence of $BaTiO_3$ exist that show qualitative agreement using a shell model potential [113].

Interatomic potentials can also be used within the construction of an Hamiltonian used for Monte-Carlo (MC) calculations presented in the following subsection. It has to be considered that interatomic potentials are always the result of simplifications, which is why for the analysis of more complex behavior, such as prediction of material behavior or prediction of new materials, quantum mechanic methods are preferred.

In this thesis interatomic potentials are used to calculate the Madelung energy of a material. In Section 4.1 the General Utility Lattice Program (GULP) [114] is used to perform calculations using purely electrostatic atomic potentials.

2.2.2 Monte-Carlo calculations

In materials modeling Monte-Carlo (MC) simulation often refers to the generation of a random sequence of states in a phase space. From the sampled states thermodynamic equilibrium-properties are obtained by calculating ensemble averages of the property of interest, according to statistical mechanics [94].

To reduce computational time, sampling can be focused on high weight points of the phase space, called importance sampling MC. In the algorithm proposed by Metropolis [115] a trajectory through phase space is constructed by starting from an initial configuration and randomly generating trial states. The transition to a trial state is accepted depending on the Metropolis probability,

$$
\omega = \begin{cases} 1 & \text{for} \quad \Delta E \leq 0 \\ \exp\left(-\dfrac{\Delta E}{k_B T}\right) & \text{for} \quad \Delta E > 0 \,, \end{cases}
\tag{2.4}
$$

where ΔE is the change of internal energy in the system associated with the transition. Thus, a transition to a lower energy is always accepted, while the transition to a higher energy is accepted with a certain probability, and more readily accepted if higher temperatures are modeled. The property of interest can be calculated by averaging over the trial states [94].

The main ingredient in Metropolis MC calculations is the Hamiltonian used to calculate the energy of a trial state. The Hamiltonian used to calculate the energy of a trial state has a strong influence on the accuracy and computational time of the MC simulations.

In the field of ferroelectric materials MC calculations have, for example, been used to analyze the morphotropic phase boundary (MPB) of $PbZr_{1-x}Ti_xO_3$ (PZT). Bellaiche and co-workers constructed an effective Hamiltonian fitted to structural parameters from virtual crystal approximation (VCA) calculations, finding a monoclinic phase [59]. Based on the same Hamiltonian, it was found that short-range order has an effect on the width of the MPB [60]. The MPB region is wider if clustering occurs, and smaller in rocksalt order. Kornev incorporated also ferroelectric and antiferrodistortive degrees in the effective Hamiltonian [116]. It was used to study finite-temperature properties of PZT solid solutions near the MPB.

In this study MC calculations employing lattice based Hamiltonians are used to assist the analysis of chemical order in Chapter 3.

2.2.3 Lattice based Hamiltonians

Lattice based Hamiltonians are model Hamiltonians that restrict the description of atomic interactions to a rigid lattice [94]. Such models are typically used to analyze various configurations, and the lattice based Hamiltonian defines the energy of these arrangements [117,118]. In the case of a binary alloy one atom is assigned to every site in the lattice [117]. It is not required that atoms lie directly on the lattice sites, but that the assignment is unambiguous [117].

Methods that construct the lattice Hamiltonian by a series expansion over site energies, three-body and higher order interaction energies are usually denoted as cluster expansions [119],

$$E_{\text{config}}(\sigma) = J_0 + J_1 \sum_i S_i + \sum_{i<j} J_{ij} S_i S_j + \sum_{i<j<k} J_{ijk} S_i S_j S_k + \dots , \qquad (2.5)$$

where i, j and k are lattice sites S_i is the pseudo-spin at the i-th lattice site that takes the value 1 or -1 depending on the atom type it is occupied with, J are characteristic energies, σ describes a particular configuration and E_{config} is the configuration energy of the relaxed configuration (see [118] and references therein).

The cluster expansion is usually fitted to total lattice energies of certain lattice configurations obtained by, *e.g.*, density functional theory (DFT) calculations. To practically use cluster expansion only a finite number of so called effective cluster interactions (ECIs) can be included [120]. When M free parameters are included in the cluster expansion fit, then the energy of at least M independent lattice configurations has to be known. Therefore, the approach depends on a sufficiently rapid convergence with respect to the number of ECIs. To generate the lattice configurations presented in Section 3.2 the computer code Cluster-Assisted Statistical Mechanics (CASM) [121] is used. Prof. Anton van der Ven (University of Michigan) is gratefully acknowledged for providing this code.

If the cluster expansion is truncated after pair interactions, and only nearest (NN) and second nearest (NNN) neighbors are included in the summation, the Ising-type model description is obtained [94],

$$E_{\text{Ising}} = h \sum_i S_i + J_1 \sum_{NN<i,j>} S_i S_j + J_2 \sum_{NNN<i,j>} S_i S_j , \qquad (2.6)$$

here h, J_1 and J_2 denote characteristic energies of the Ising model. In the second and third sum i runs over all atoms while j runs over all nearest neighbor atoms and all second nearest neighbor atoms of i respectively. The Ising model was originally proposed as a model for ferromagnetism. Nowadays, the model is also employed for various other applications, such as the binary alloys just described and the description of the disorder-order ferroelectric phase transition [6,11] that was mentioned in the previous chapter.

In Section 3.4 the configurational energy of the perovskite solid solution PZT is analyzed. To use lattice based Hamiltonian calculations the solid solution is considered to be a primitive cubic lattice on whose lattice positions the perovskite formula unit of either $PbTiO_3$ or $PbZrO_3$ is positioned. An Ising type model is then used to describe the mixing energy. The model is fitted to DFT results of the mixing energy.

CHAPTER 3

Chemical order in lead zirconate titanate

PbZr$_{1-x}$Ti$_x$O$_3$ (PZT) is a homovalent mixed perovskite solid solution. The B-site atoms Ti and Zr are generally considered to be disordered, due to the lacking electric driving force [29]. However, experimental and theoretical studies have found evidence for local order. An experimental study observed the formation of {110} titanium planes in epitaxial films [56]. First-principles calculations found evidence for B-site cation arrangement in {111} planes together with negative mixing energies [57].

In this chapter this discrepancy, between what is generally considered and some experimental and theoretical studies on the cation ordering and mixing energies of PZT, is investigated. The chapter starts with a discussion of how chemical order is modeled for PZT. In Section 3.2 cation ordering in PZT is qualitatively analyzed, in Section 3.3 and 3.4 order is quantitatively analyzed. Preferred structural motifs are identified and presented, the reason for the preference is analyzed, and the thermodynamics of the PZT are system investigated. Finally, the obtained results are summarized and a conclusion is given.

3.1 Modeling chemical order in PZT

Chemical ordering can disrupt the symmetry of a structure. Due to the arrangement of different elements on the same crystallographic site the local symmetry of each atom is influenced. Depending on their local symmetry different atomic displacements can occur. In atomistic simulations a statistical occupation of a crystal site can only be approximated, all model structures are ordered [91,93,94]. In the previous chapter chemical order was proposed as one possible parameter to influence the results in approaches predicting the composition of the morphotropic phase boundary (MPB). Thus, chemical ordering should also be analyzed to assess how the materials are modeled best. In this chapter chemical ordering is analyzed in PZT.

Phase equilibria installed above the Curie temperature are relevant for the materials composition and structure in the ferroelectric regime. PZT ceramics are mostly processed at elevated temperatures [34] and then rapidly cooled down into the ferroelectric phase. Density functional theory (DFT) calculations of vacancy migration [32,33] suggest, that diffusion in perovskites is kinetically hindered and can be considered negligibly small below the Curie temperature. Therefore, ordering, decomposition or phase separation achieved at high temperatures will be frozen and the thermodynamic limit is experimentally never reached in the ferroelectric phase. Due to this reasoning chemical ordering is analyzed in the high temperature cubic structure.

Experimental studies of high temperature PZT showed local polar arrangements [122,123]. However, the local environments are homogeneously distributed such that the symmetry of the structure is cubic. To correctly model the structure, different polarization directions need to be modeled in micro-domains, taking into account domain wall energies. This can be done by fitting an effective Hamiltonian to DFT calculations of one particular cation-order or by virtual crystal approximation (VCA) calculations [116]. However, to analyze chemical order, various cation arrangements have to be calculated in supercells. Thus, a structure of averaged cubic symmetry is best chosen neglecting local polar arrangements.

In Section 2.1.2 it was presented, that the input structure in first-principles methods imposes symmetry constraints on the calculations, and that DFT calculations in different symmetry constraints might obtain different structures [101,102,108]. Therefore, two different approaches are used to model the PZT system in this chapter.

PZT is modeled in varying supercell sizes, built from one to six formula units (f.u.) of the ideal perovskite structure, in Section 3.2. All possible geometries are used, thus, a total of 161 configurations are modeled. The usage of various geometries allows for the sampling of various symmetry constraints. The configurations are used for a qualitative analysis. Preferred structural motifs are identified and pre-

sented. A quantitative analysis is omitted, to avoid comparing structures obtained from calculations in different symmetry constraints.

In Section 3.3 PZT is modeled in a 2×2×2 supercell, using all possible B-site occupations. The restriction to one specific supercell leads to similarities in the symmetry of the modeled configurations. Although the symmetry of the structure is determined in part by the B-site occupation, the symmetry constraints due to the supercell size and geometry are the same. In a 2×2×2 supercell modeling a B-site mixed perovskite, each crystallographic B-site is positioned at an inversion center, due to periodic boundary conditions independently from cation site occupation. In the experimentally observed high temperature cubic perovskite structure the B-site is also positioned at an inversion center. Thus, B-site occupations calculated in a 2×2×2 supercell are considered to be pseudocubic, and similar enough for the structures to be quantitatively comparable.

The different approaches are used for different aims. The calculations in Section 3.2 are used to identify preferred structural motifs, while the calculations in Section 3.3 are used to analyze the reasons why some structural motifs are preferred. Both sections present total energy calculations that can provide a hint towards order or disorder in the cubic phase of PZT. However, the cubic perovskite structure exists at elevated temperatures. To assess how entropy effects influence order tendencies at those temperatures Monte-Carlo (MC) calculations are used in Section 3.4.

3.2 Qualitative analysis

3.2.1 Computational setup

DFT calculations were performed using the Vienna ab-initio simulation package (vasp) [101] within the local density approximation (LDA) using projector augmented wave (PAW) potentials [124] including the Pb $6s^2$ $6p^2$, Ti $3d^2$ $4s^2$ $3p^6$, Zr $4s^2$ $4p^6$ $4d^2$ $5s^2$ and O $2s^2$ $2p^4$ electrons. Integration in reciprocal space was performed on a Gamma point centered Monkhorst Pack mesh adapted to each supercell from a $8 \times 8 \times 8$ mesh in the unit cell. The energy cutoff used was $700\,\text{eV}$.

Neglecting the B-site occupation, all calculations are started from the ideal cubic structure. Cell parameters are relaxed in steps, alternating between internal cell-parameter relaxation and volume relaxation. The lattice parameters are held at a pseudo-cubic ratio.

The cell consisting of one formula unit is used to calculate pure $PbTiO_3$ and $PbZrO_3$. Using two formula units, three additional supercell symmetries are re-

alized at 50 %PbTiO$_3$. The supercells built from three formula units add six more configurations. With increasing number of formula units an increasing number of cell geometries and configurations are accessible. Supercells built from up to six formula units are constructed using the computer code Cluster-Assisted Statistical Mechanics (CASM) [121] from Prof. Anton van der Ven, University of Michigan. The providing of this code is gratefully acknowledged.

The energies of the pure phases are used as a reference for calculating the mixing energy E_{mix}:

$$E_{\text{mix}} = E_{\text{PbZr}_{1-x}\text{Ti}_x\text{O}_3} - (1-x)E_{\text{PbZrO}_3} - xE_{\text{PbTiO}_3}, \qquad (3.1)$$

where $E_{\text{PbZr}_{1-x}\text{Ti}_x\text{O}_3}$ is the total energy of the mixed structure, E_{PbZrO_3} the total energy of lead zirconate and E_{PbTiO_3} the total energy of lead titanate.

3.2.2 Results

Figure 3.1 shows the formation energies for all supercells that could be calculated from up to 6 formula units. About one fifth of the data points show a negative formation energy, while the other formation energies are positive. For easier viewing, supercells that contain the same number of formula units are marked by points of the same color. The lowest formation energies that can be obtained with 1 to x numbers of formula units are connected with lines in the color of x. Three chosen configurations are marked additionally.

For an increasing number of formula units used to construct the supercells more negative formation energies are found. This indicates that the supercell with the lowest energy was not yet calculated. It has to be expected, that in calculations modeled from more formula units, lower formation energies will still be found. Thus, the most stable structure cannot be identified. However, as discussed before, a direct comparison of these structures with different symmetry constraints is questionable.

The obtained diagram is asymmetric: The structure with lowest formation energy obtained for low Ti content is not the inverted structure with the lowest formation energy for high Ti content. The lowest formation energy is observed for a Ti content of 66 %PbTiO$_3$ (ti66L), which is marked with a circle in Figure 3.1. The most remarkable configuration is the most favored structure at 16 %PbTiO$_3$ (ti16L), marked with a triangle in the figure. Its formation energy is considerably lower than the other structures calculated at this concentration, indicating the presence of a favored structural motif.

Figure 3.2 shows the B-site cation configurations of three preferred structures. In addition to the already mentioned cation configurations "ti66L" and "ti16L", the configuration with the lowest energy at 50 %PbTiO$_3$ (ti50L), marked with a square
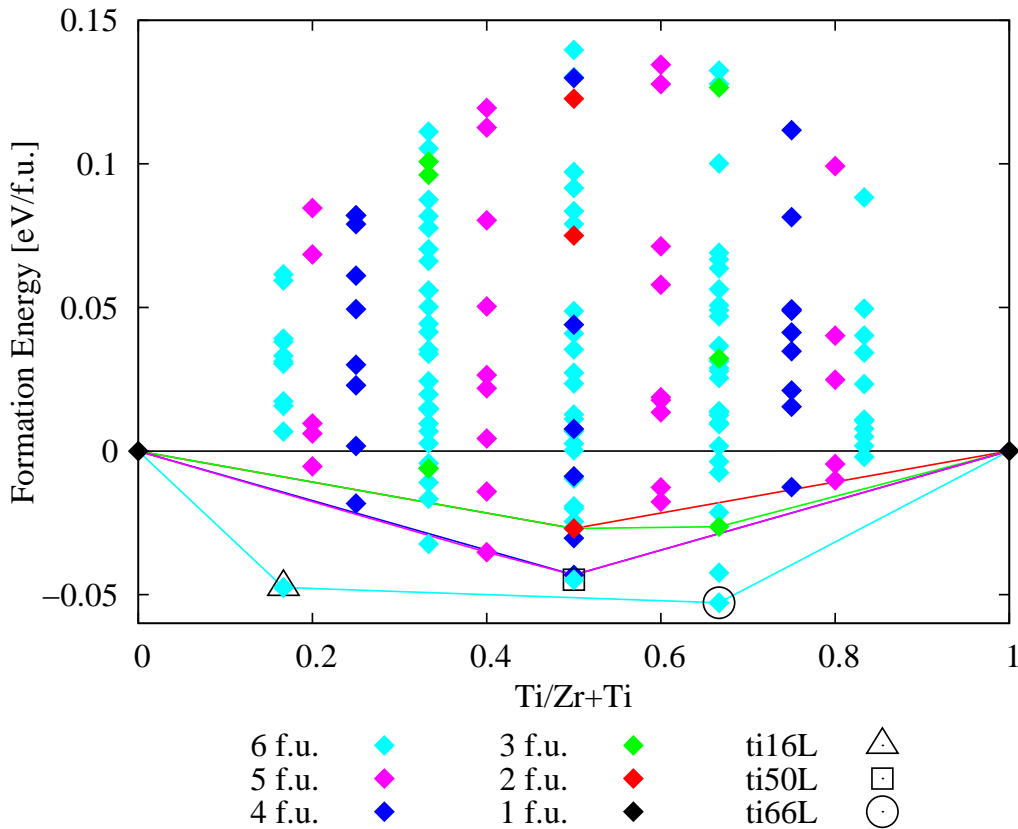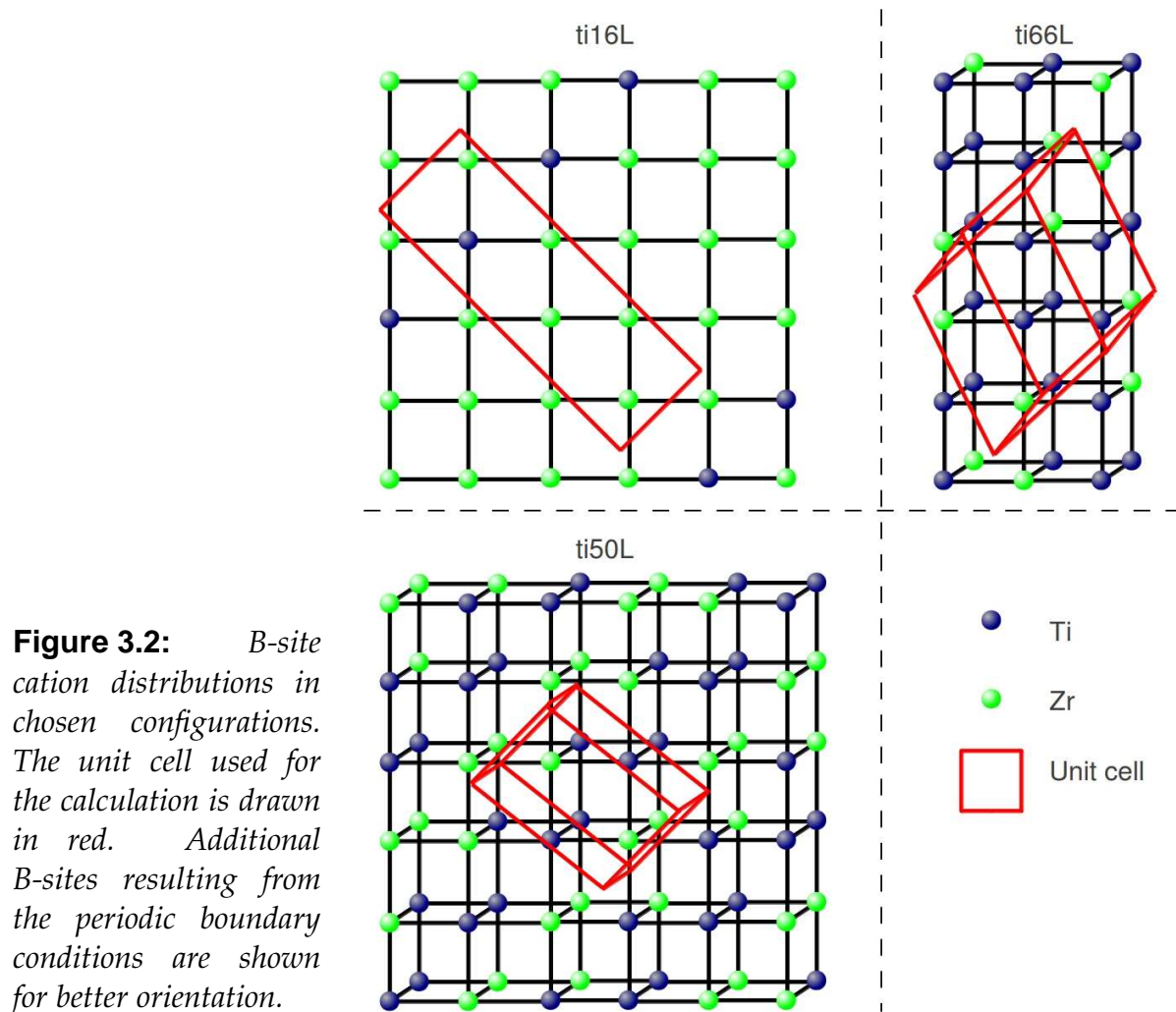
Figure 3.1: *PZT formation energies in varying supercells. Configurations built from the same number of unit cells are marked in the same color.*

in Figure 3.1, is shown. The boundaries of the calculated unit cell are drawn in red, additional B-site cations resulting from the periodic boundary condition are shown for better orientation. Structure "ti16L", which is strongly favored over the other configurations at $16\%\text{PbTiO}_3$, is a layered structure. The B-site sublattice is built out of one (110) titanium plane and five (110) zirconium planes. Structure "ti66L" is a more complex layered structure. One (110) Ti plane is followed by two Ti/Zr (110) planes that are ordered in a checkerboard pattern; afterwards another Ti (110) plane follows, that is itself followed by two Zr/Ti (110) planes that are ordered in a checkerboard pattern inverted in reference to the other mixed planes. The structure can also be explained as forming (120) Zr planes that are arranged along zigzag folded (111) planes. Structure "ti50L" is built from one Ti (110) plane, followed by a Zr (110) plane and a mixed Ti/Zr (110) plane that is ordered along [110] columns; afterwards follows another Ti (110) plane and another Zr (110) plane, followed by a mixed Zr/Ti plane that is ordered along [110] columns inverted from the other

Figure 3.2: *B-site cation distributions in chosen configurations. The unit cell used for the calculation is drawn in red. Additional B-sites resulting from the periodic boundary conditions are shown for better orientation.*

mixed plane. Thus, the (110) planes observed are arranged along (111) planes that are folded in a zigzag pattern.

As {111} and {110} motifs can be identified in the three favored structures Figure 3.3 identifies structures built from {110} or {111} planes. The figure shows the calculated formation energies. Marked with a triangle are configurations that are completely built from {111} planes, while calculations marked with a square are completely built from {110} planes. Additionally, the most stable structure for each composition calculated is marked with a circle. It can be seen from the figure, that structures completely built from {111} planes are distributed closely to the zero line of formation energy. The deviation from zero tends equally towards negative and positive values and is largest at $50\,\%PbTiO_3$ with a value of about $-0.03\,eV/f.u.$. Configurations that are completely built out of {110} planes are only favored for
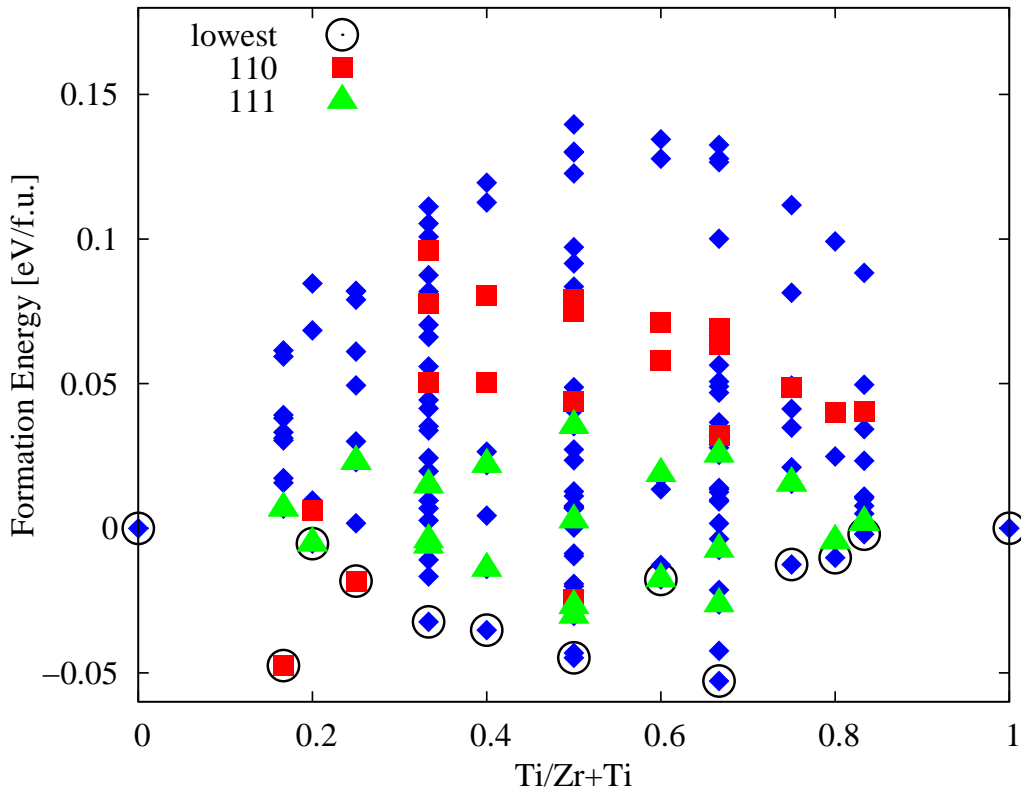
Figure 3.3: *PZT formation energies in varying supercells. B-site configurations built from {110} and {111} planes are marked as well as the most stable structure for each concentration.*

very low titanium contents. However, one of these structures, the "ti16L" structure, is strongly favored over the other structures at this concentration.

To identify additional preferred patterns, the B-site sublattice of the most stable configuration was analyzed for each concentration calculated. The configurations are marked with a circle in Figure 3.3. At 16 % $PbTiO_3$, the structure "ti16L" is observed; it is built from {110} planes. The most stable structure at 20 % $PbTiO_3$ shows {111} planes, while the structure at 25 % $PbTiO_3$ shows again {110} planes. For 33 % $PbTiO_3$, {110} planes are observed in {111} zigzag, while at 40 % $PbTiO_3$ 120 layers are seen. The preferred structure at 50 % $PbTiO_3$ is the already mentioned structure "ti50L", in which {110} planes are ordered along {111} zigzag folded planes. For 60 % $PbTiO_3$, {111} planes are seen again. At 66 % $PbTiO_3$, the structure "ti66L" is preferred. It can be described as Ti and mixed {110} planes, or as 120 layers that are arranged along zigzag folded {111} planes. Summarizing, the preferred structures show the already mentioned {110} and {111} patterns, and rarely also 120 patterns.

The formation of {110} Ti planes is seen in many favored structures, but structures entirely built from {110} planes are only favored for very low Ti content. From 25 %PbTiO$_3$ to 33 %PbTiO$_3$ the formation energy of structures built from one Ti (110) plane and three Zr (110) planes and the structure built from one Ti (110) plane and two Zr (110) planes rises from -0.018 eV/f.u. to 0.096 eV/f.u.. The two structures differ in their titanium content, but also in the size of the supercell they are calculated in. To assess the influence of relaxation possibilities in differently sized supercells, calculations of the structure built from one Ti (110) plane and two Zr (110) planes were repeated in a larger pre-relaxed cell. The supercell symmetry in this configuration is deliberately more reduced than necessary. Thus, the results calculated from it are not used for direct comparison, but only as indication. For the pre-relaxed cell a formation energy lower than the other structures for the same concentration and even lower than the "ti16L" structure is observed. Thus, the calculations provide a further indication that Ti {110} planes are a preferred motif. It also serves as a verification of the first observation that lower formation energies can be observed in larger supercells.

3.2.3 Summary and discussion

The presented results indicate a preference of PZT to show {110} planes and {111} patterns, and an influence of relaxation possibilities on formation energies.

The preference of {110} planes is strongest for low titanium content where {110} B-site planes that are only occupied by either zirconium or titanium are observed. For higher Ti contents pure {110} planes are still observed, but also mixed planes. In addition, the tendency to built Ti-planes is stronger than Zr planes, as indicated by the preferred structure "ti66L" where no pure Zr {110} plane is formed. This observation of a preference of {110} Ti planes is supported by experimental work on epitaxial films [56].

The tendency to form {111} patterns is observed in favored structures of all concentrations. These patterns are often associated with {110} planes.

The calculations indicated an influence of relaxation possibilities. It was observed that for concentrations modeled with a different number of formula units, the configurations modeled in larger supercells were preferred. Also, in the calculation of a layered cation configuration in two cell sizes, the larger supercell obtained lower energies.

Based on these results, the thermodynamic equilibrium structure of PZT could be a mixture of {111} patterns in combination with {110} Ti planes. The reasons for the preference of structural motifs is analyzed in the following section.

3.3 Quantitative analysis

The calculation of PZT in various supercell geometries was used to identify fa-vored motifs. However, a quantitative analysis why these motifs are preferred had to be omitted as the cells were calculated in different symmetry constraints influencing the calculation results. In this section first-principles calculations of the pure phases and solid solutions of PZT are performed in a 2×2×2 supercell. The modeled struc-tures are considered to be pseudocubic, and similar enough for the structures to be quantitatively comparable. The structures are used to quantify energetic differences of structural motifs, while keeping in mind that the analyzed phase field is restricted.

3.3.1 Computational setup

DFT calculations were performed using the VASP [101] within the LDA using PAW potentials [124] including the Pb $5d^{10}$ $6s^2$ $6p^2$, Ti $3d^2$ $4s^2$ $3p^6$, Zr $4s^2$ $4p^6$ $4d^2$ $5s^2$ and O $2s^2$ $2p^4$ electrons. All possible 22 permutations in a 2×2×2 supercell that can be built from the ideal perovskite structure are used for calculations. Integration in reciprocal space was performed on a Gamma point centered $4 \times 4 \times 4$ Monkhorst Pack mesh, an energy cutoff of 700 eV was used. Internal cell parameters were allowed to relax and the cell volume was held fixed, calculations were performed at different volumes. The obtained energies were fitted to the Birch-Munaghan equation of state [125], and the obtained minimum energy was used for further analysis.

For simulating the solid solution system, a $2 \times 2 \times 2$ ideal perovskite supercell is constructed and all possible compositions and B-site occupancies are modeled. As
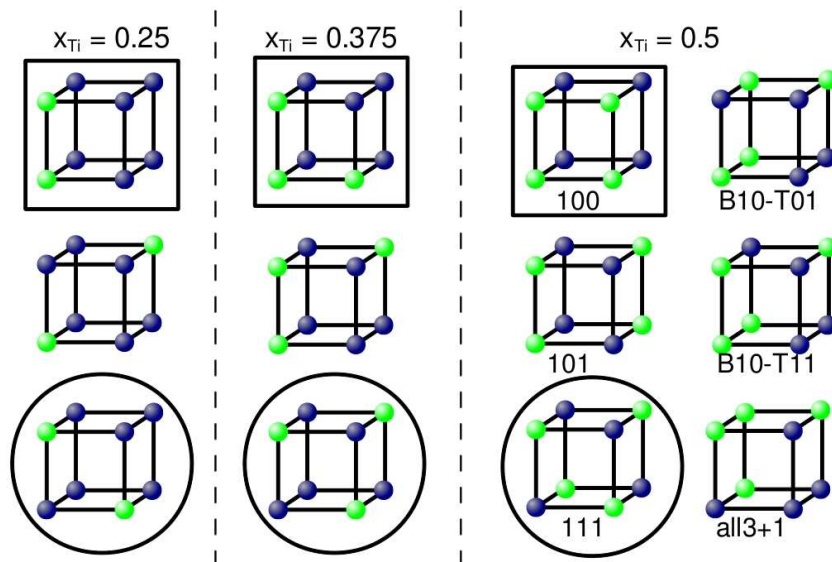

Figure 3.4: *B-site configuration of PZT in a 2×2×2 supercell; for each composition the least stable structure is marked with a square, the most stable with a circle.*

a preparatory step, the energy of the pure phases are calculated in cubic structure, to be used as a reference for the mixing energy according to equation 3.1. For the compositions $x_{Ti} = 0.125$ and 0.875 ($x_{Ti} = \frac{n(Ti)}{n(Ti)+n(Zr)}$) only one possible permutation exists; for the compositions $x_{Ti} = 0.25$, 0.75, 0.375 and 0.625, three permutations can be calculated. Six permutations are possible at the concentration $x_{Ti} = 0.5$. Figure 3.4 shows the permutations.

3.3.2 Results

Figure 3.5 shows the energies of mixing for all compositions and permutations accessible within a $2\times2\times2$ supercell. For all but one calculated structure the mixing energies are positive. The positive mixing energies at composition $x_{Ti} = 0.125$ and $x_{Ti} = 0.875$ correspond to the formation of one anti-site in the supercell. The compositions, where multiple permutations are possible, show that the calculated energies depend on the atomic order of the B-site atoms. In the least stable configurations (marked with a square), the Zr and Ti atoms are inhomogeneously arranged and
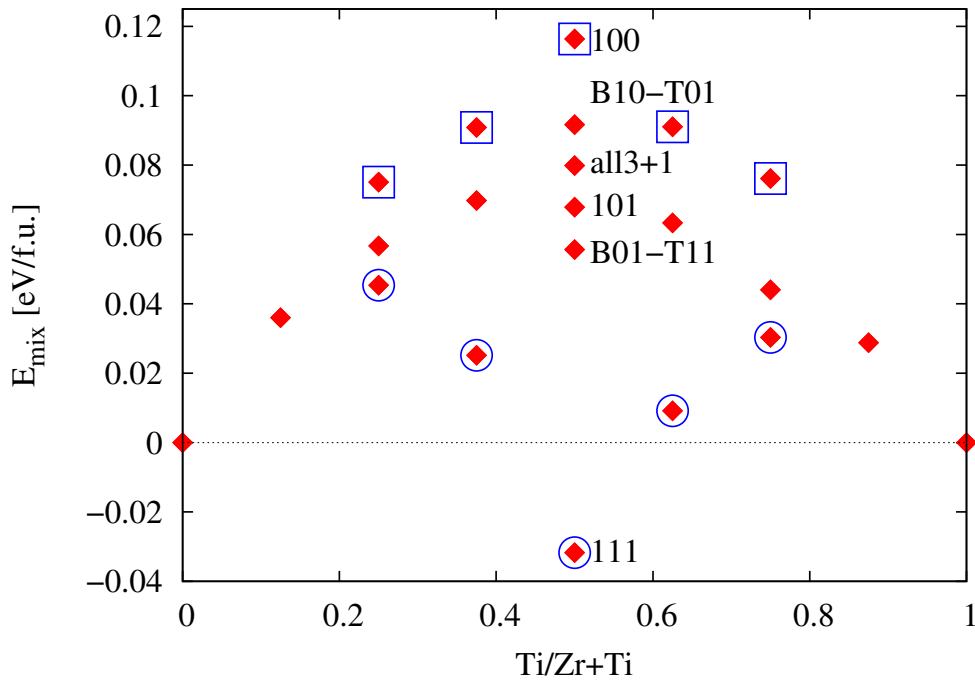

Figure 3.5: *PZT mixing energies of different configurations in a $2\times2\times2$ supercell. The different configurations are shown in Figure 3.4.*

Order	a [Å]	O-Ti-O [Å]	O-Zr-O [Å]
{111}	4.006	3.870	4.142
{100}	4.020	3.799/4.020	4.241/4.020

Table 3.1: *Oxygen octahedra in {111}- and {100}-ordered $PbZr_{0.5}Ti_{0.5}O_3$.: Given are the lattice constant, edge length and tip distance of the octahedron.*

form clusters. In the most stable permutations (marked with a circle), B-sites are alternately occupied by Zr and Ti atoms along the $\langle 100 \rangle$ direction.

The permutation "111" for $x_{Ti} = 0.5$ is a special case, being the only one with a negative mixing energy. In this case, B atoms are arranged homogeneously with alternating occupation along the $\langle 100 \rangle$ direction. To understand the energetic differences, the local structure at $x_{Ti} = 0.5$ is analyzed in more detail. Titanium is smaller than zirconium and slightly more electronegative. Therefore, oxygen atoms are pulled towards the Ti atoms and the oxygen octahedra surrounding Ti are smaller than the ones surrounding Zr. In the {111}-ordered structure this size difference can be compensated best, as smaller and larger octahedra form an alternating sequence (see Figure 3.6).

From the calculated structures with {111} and {100} ordering the size of the oxygen octahedra surrounding Ti and Zr (see Table 3.1) is extracted by measuring the edge length of and the distance between the tips. In the {111}-ordered case, ideal octahedra are observed, while in the {100}-ordered structure the octahedra surrounding Ti and Zr are compressed or stretched.

Based on these structural data, it can be shown by simple model calculations that the difference in mixing energies for both cation arrangements is essentially due to the strained oxygen octahedra. The strain energy for pure $PbTiO_3$ and $PbZrO_3$ is
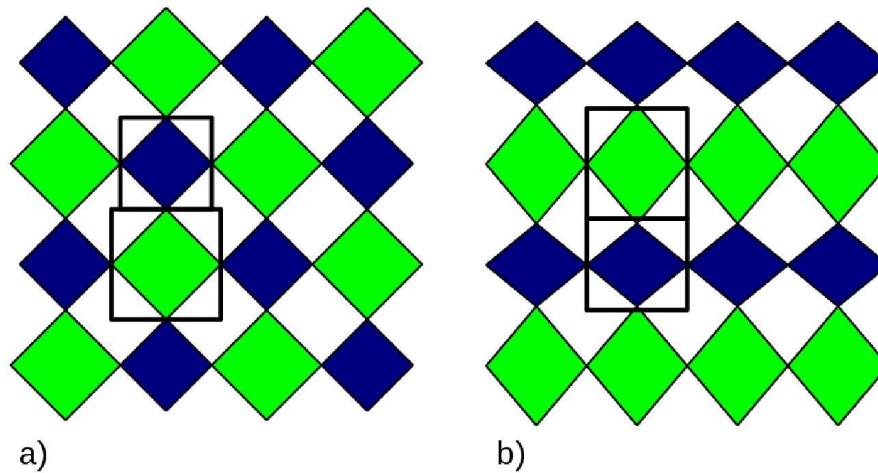

a)   b)

Figure 3.6: *Schematics illustrating the consequences of oxygen octahedra of different sizes for the example of {111} and {100} ordered $PbZr_{0.5}Ti_{0.5}O_3$.*

Table 3.2: *Mixing energy of the {111} and {100} ordered phases in comparison to the pure strain contributions to the mixing energies.*

Structure	ΔE [eV/f.u.]	$\Delta E100$- $-\Delta E111$ [eV/f.u.]
pure phases	0	
$PbZr_{0.5}Ti_{0.5}O_3$ {111}-Ordered	-0.032	
$PbZr_{0.5}Ti_{0.5}O_3$ {100}-Ordered	0.116	0.148
virtual superstructure (111)	0.027	
virtual superstructure (100)	0.167	0.140

calculated at lattice constants that correspond to the octahedra sizes found for the supercells with {111} and {100} cation ordering as depicted in Figure 3.6 by black lines. The superposition describes the case that the structure would be composed of lead zirconate at lattice constants obtained from the zirconium octahedra in the {111}-ordered structure and lead titanate at lattice constants obtained from the titanium octahedra in the {111}-ordered structure. Thus, the calculated mixing energies obtained by superposing these data represent the energy of a virtual superstructure, where only strain effects are considered. Table 3.2 shows the results of the supercell calculations in comparison to the energies of the virtual superstructures. It can be seen that the mixed structures are at lower energies than the superposed data. The energy difference between {111} and {110} ordered $PbZr_{0.5}Ti_{0.5}O_3$ (0.148 eV/f.u.) is almost the same as the energy difference between the virtual superstructure (111) and (100) (0.140 eV/f.u.). This indicates that the energy difference between the mixed structures is due to size differences and related stresses in the oxygen octahedra. Therefore, it provides a rational explanation for the energetic preference of the {111} ordered configuration over all other cation arrangements.

3.3.3 Discussion

The quantitative calculations presented in this section reveal the permutation "111" as the most stable. The results are in line with another comparative DFT study [57] and calculations within a semi-empirical ionic-crystal [58] model which find {111} ordered $PbZr_{0.5}Ti_{0.5}O_3$ to be the most stable mixture.

In permutation "111", B-site atoms are arranged homogeneously with alternating occupation along the $\langle 100 \rangle$ direction, thus, size difference of Ti and Zr can be compensated best. The difference in mixing energies for the calculated cation ar-

rangements is essentially due to strained oxygen octahedra. This provides evidence that the energy difference between the mixed structures is due to size differences and related stresses in the oxygen octahedra. It is noteworthy that DFT calculations on aliovalent B-site mixed lead based materials $(Pb(B,B')O_3)$ show similar energy differences between the {100} and {111} ordered structures [30]. Because the size difference of the mixed ions is similar to the size difference of Ti and Zr, the similarity in energy could be seen as another indication that the energy difference between different mixed structures is due to the size mismatch.

The quantitative calculations give additional indication of the influence of relaxation possibilities already proposed from qualitative calculations presented in Section 3.2. The comparison of mixed calculations in the $2 \times 2 \times 2$ supercell to superposed calculations of deformed pure materials revealed a discrepancy. The mixed structures are at lower energies than the superposed data. This is most probably due to missing local relaxation and long-range interaction in the case of the virtual superposed structures.

From the qualitative calculations is was assumed, that the thermodynamic equilibrium structure of PZT is a mixture of {111} patterns in combination with {110} Ti planes. The calculations of this section have shown that {111} planes are preferred due to size differences of Ti and Zr. The preference of {110} Ti planes could not be observed in this section. The qualitative calculations showed that the preference was only observed for larger cells with less symmetry constraints. Patterns formed by {110} Ti planes introduce a symmetry break. In this lower symmetry the B-site positions are no longer inversion centers and further cation relaxation, allowing for lower formation energies, is possible. The configurations modeled for this section show an inversion center coinciding with the B-site. Thus, it can be inferred that the calculations presented in this section were performed in a too restricted symmetry to show the preference of {110} Ti planes.

3.4 Thermodynamic assessment

The total energy calculations presented in the previous sections indicated the preference of {111} patterns and {110} Ti planes in cubic PZT. However, one has to keep in mind that the cubic perovskite structure exists at elevated temperatures. At such temperatures the Gibbs free energy could be dominated by entropy rather than by energy contributions due to ordering and phase decomposition.

Metropolis MC calculations are a viable tool to analyze order effects and phase stability at finite temperatures. The prerequisite for Metropolis MC simulations is a

valid, computationally efficient Hamiltonian. The qualitative calculations presented in Section 3.2 indicate that deriving an Hamiltonian valid for the whole phase field of PZT from Cluster expansion is an enormous challenge.

To still assess how entropy effects influence order tendencies at higher temperatures PZT can be modeled in a restricted phase field. It is possible to model only cation order which is characterized by an inversion center at the B-site. The respective data calculated in 2×2×2 supercells in Section 3.3 is in itself consistent and can be modeled with an effective Hamiltonian. However, it should be stressed, that the analyzed phase field is severely restricted. For example, the preference of the structural motif of {110} Ti planes cannot be modeled in this phase field. Only effects occurring due to size mismatch are analyzed.

3.4.1 Computational setup

To perform Metropolis MC calculations, a model Hamiltonian is fitted to the mixing energies. The configuration energies presented in Section 3.3 are fairly symmetric with respect to cation concentration. Therefore, a simple lattice based Ising model including nearest and second-nearest neighbor interaction on the B-site sublattice is used. As a simplification, the interactions between atoms of the same type are neglected in calculating the mixing energy:

$$E_{\mathrm{mix}} \quad = \quad N_1 J_1 + N_2 J_2. \tag{3.2}$$

Here, N_1 is the number of different nearest neighbors, N_2 is the number of different second nearest neighbors, J_1 is the interaction parameter between different nearest neighbors and J_2 is the interaction parameter between different second-nearest neighbors.

Equation 3.2 is fitted to the DFT results. As expected from the results in Section 3.3, the interaction parameter obtained for different nearest neighbors is negative ($J_1 = -1.2241 \cdot 10^{-2}$) and positive for different second nearest neighbors ($J_2 = 2.6040 \cdot 10^{-2}$). Figure 3.7 shows the accuracy of the fit by comparing the mixing energies calculated from DFT to those calculated using the Hamiltonian for all configurations the fit is based on.

In Section 3.3 the main energy difference of the varying permutations is because of size differences between zirconium and titanium. Therefore, the usage of an Hamiltonian fitted to these results has to assume a similar temperature expansion of $PbTiO_3$ and $PbZrO_3$. A similar value of B' is obtained fitting the Birch-Munaghan [125] equation to energy calculations of cubic $PbTiO_3$ and $PbZrO_3$. Thus, the indication of a similar temperature expansion coefficient validates the assumption.
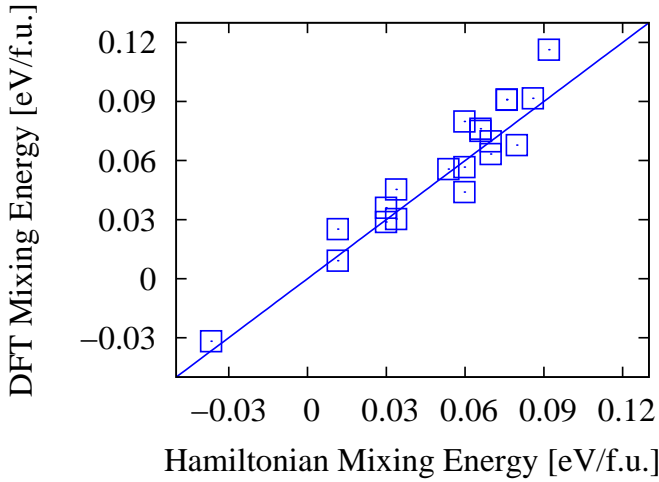
Figure 3.7: *Comparison of DFT mixing energies to Hamiltonian mixing energies.*

3.4.2 Results and discussion

Mixing energies at finite temperature

MC-calculations are started from fully random cation distributions at 2500 K. The systems are subsequently cooled down in steps of 100 K. 600 MC steps were performed at each given temperature. Due to the slow cooling, the simulations converged within the first 100 MC steps. The parameters extracted from the calculations are the energy E and an order parameter O, which is defined as

$$O = \frac{N_1^{\text{same}} - N_1}{N_1^{\text{all}}} \, . \tag{3.3}$$

In this expression, N_1^{all} is the number of nearest neighbors, N_1^{same} the number of nearest neighbors that are of the same atom type and N_1 is the number of nearest neighbors that are of different atom type. The energy and order parameter for a given temperature and composition were calculated as the mean value taken over the last 100 MC steps.

The energy and order parameter for a given concentration are plotted in Figure 3.8 as a function of temperature. The figure shows a second-order phase-transition at about 1950 K, where an order-disorder transition occurs. For higher temperatures, the cation distribution is random. Below the transition, an additional phase is observed which is rocksalt ordered. Also, a small peak can be seen in the temperature dependent energy. It coincides with the disappearance of the disordered phase.

Figure 3.9 shows results of the Monte Carlo calculations for various temperatures as a function of concentration together with experimental data and the case of a random alloy. Since the Hamiltonian (equation 3.2) is symmetric with respect to the exchange of cations, the calculated mixing energies at finite temperature are also symmetric. The calculation at 1000 K might serve as an example to explain
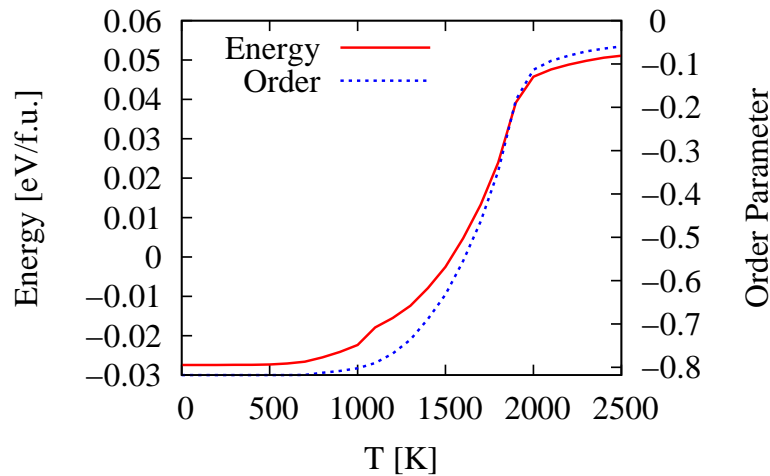
Figure 3.8: *Order parameter and energy as a function of temperature for $x_{Ti} = 0.45$ obtained by Monte Carlo calculations*

the relation between the energy-composition plots and the cation distribution. The curve shows a global minimum at $x_{Ti} = 0.5$, two maxima and abrupt changes in the gradient. Starting from $x_{Ti} = 0$, adding Ti leads to defects in lead zirconate marked by an energy increase of the system and a disordered structure. At the energy maximum, a more stable phase starts to form. The more stable phase shows rocksalt ordering on the B-site lattice. This leads to a lowering of energy and a phase separation into the disordered and the rocksalt ordered phase. From that point, the energy of the system decreases while the amount of the rocksalt ordered phase increases and the amount of the disordered phase decreases. Then the disordered phase vanishes and the energy decrease becomes steeper, seen in an abrupt change in the gradient. The structure is now completely rocksalt ordered {111}.

Figure 3.9 also compares selected calculated mixing energies to experimental results. The random alloy corresponds to a temperature above 2000 K, which in reality is already beyond the stability range of the cubic perovskite. A comparison of the data corresponding to 1000 K to measurements of the mixing energy at 973 K by Rane [63] does not show agreement. The calculation for a random alloy, on the other hand, is mostly within the errors of Rane's measurements. This suggests that the experimental samples were fully disordered. Excess Gibbs energies from derived thermodynamic activities by Jacob [64] at 1373 K and MC calculations of 1400 K are, however, within the same range.

The discrepancies between calculations and experiments can be attributed to two factors. Firstly, the calculations analyze the phase field of PZT in thermodynamic equilibrium; secondly, the calculations are based on very restricted data. Cation mobility is slow to reach the thermodynamic limit even in this temperature regime.
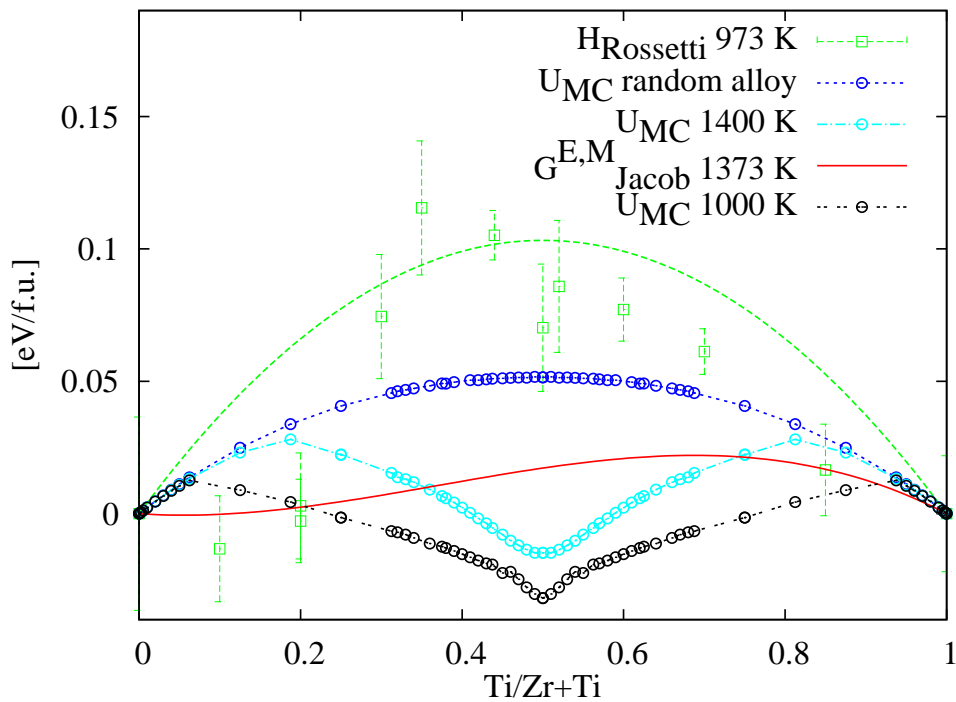
Figure 3.9: *Monte Carlo energies (U_{MC}) for selected temperatures in comparison to experimental results ($G_{Jacob}^{E,M}$ [64] and $H_{Rossetti}$ [63])*

Therefore, not all experimental samples might be fully equilibrated. It can be assumed, that most samples analyzed by Rane [63] are far away from thermodynamic equilibrium, as their measured energy is close to the energies calculated for a random alloy. For low and high Ti contents some samples might be better equilibrated, as they are energetically closer to the values calculated for the same temperature. The materials measured by Jacob [64] might not be far from thermodynamic equilibrium, because the measured values are in the same range as the calculated values for the same temperature. It is assumed that the experimental and calculated results are in the same range but still differ considerably, due to the very restricted data the MC calculations are based on.

High temperature phase diagram

The phase diagram for the cubic phase is assessed based on the MC results in a restricted symmetry. This is achieved by analyzing the order parameter and mixing energy as a function of temperature and composition. Figure 3.10 shows the proposed phase diagram of a restricted phase field of PZT. The high and low temperature parts are taken from literature [126,127], as the results presented in this
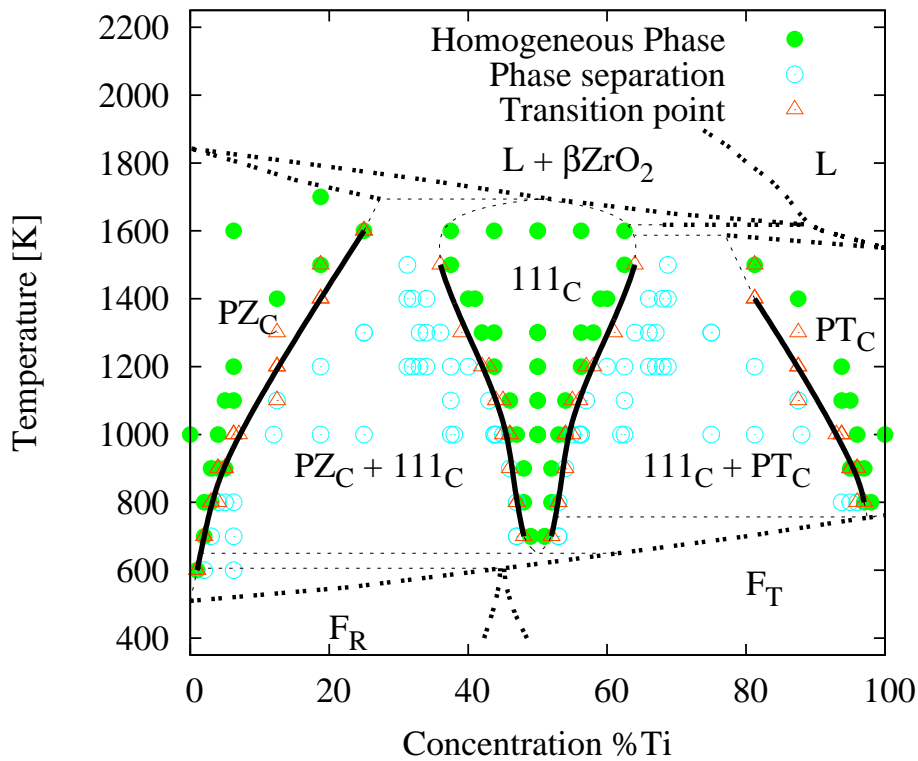
Figure 3.10: *Possible phase-diagram of PZT. Thick solid line are drawn according to the presented results. Thick dotted lines are taken from literature [126,127]. Thin dotted lines are a possible way to connect the presented results to the existing literature data.*

chapter only apply to the cubic solid phase. In the high temperature solid solution a homogeneous Zr-rich, a homogeneous Ti-rich, and a homogeneous {111} ordered phase field are separated by two-phase-fields. Thick solid lines are drawn as phase boundaries between the observed phase fields on the transition points described in Section 3.4.2. For small concentrations, the lines coincide with the solubility limit of the anti-site defect described in Section 3.3. Thin dotted lines are a possible way to connect the three parts of the phase diagram according to the laws of thermodynamics.

The presented phase diagram shows the influence of entropy on a specific cation order. The diagram shows that order induced due to size differences is still favored at elevated temperatures. However, the analysis in Section 3.2 indicated that several types of ordering occur, with a smaller difference in formation energy between them. Therefore, the driving force for one particular ordering is smaller. Due to the slow B-site cation diffusion, the areas of order might be too small to be observed in experimental samples.

3.5 Summary and conclusion

In this chapter chemical order in PZT was analyzed based on DFT calculations.

Qualitative calculations show a preference to form {110} planes and {111} patterns. The preference of {110} planes is strongest for low titanium content. For higher Ti contents, pure {110} planes are still observed, but also mixed planes. In addition, the tendency to build Ti-planes is stronger than the tendency to build Zr planes. An experimental work also showed a preference of {110} Ti planes [56]. The tendency to form {111} patterns is observed in favored structures of all concentrations. These patterns are often associated with {110} planes.

Quantitative calculations reveal, that the tendency to form {111} patterns is due to size differences of the B-site cations. The calculations show, that in a restricted phase field characterized by symmetry centers on the B-sites, the rocksalt ordered permutation "111" is the most stable. In this permutation the size difference between Ti and Zr can be compensated best. It was shown that the differences in mixing energies for cation arrangements is essentially due to size differences and related stresses in the oxygen octahedra. MC calculations based on the data obtained from the quantitative calculations showed the "111" rocksalt structure to be stable at elevated temperatures. This indicates that the entropy of mixing at elevated temperature does not destroy local ordering.

Quantitative and qualitative DFT calculations showed an influence of relaxation possibilities on the mixing energies. It was observed, that concentrations modeled with a different number of formula units, obtained lower energies in the larger supercells.

Based on these calculations, it is assumed that the thermodynamic equilibrium structure of PZT is a mixture of {111} patterns in combination with {110} Ti planes. {111} planes are preferred due to size differences between Ti and Zr. Long range patterns formed by {110} Ti planes introduce a symmetry break, as a result, further cation relaxation is possible, allowing for lower formation energies.

Experimental observation of the expected patterns will, however, be difficult. Calculations in varying supercell geometries show various configurations whose negative formation energy differ only by small amounts. Therefore, the driving force towards a specific ordered structure will not be sufficient to allow for diffusion in PZT where it is kinetically hindered. In addition, the assumed combination of {111} patterns and {110} Ti planes might result in locally ordered areas, disrupting a long range order that is easier observed experimentally. In this reasoning, the experimental study showing a preference of {110} Ti planes would be an exception [56]. As a thin film is analyzed, diffusion might be accelerated. In addition, the constraints of the substrate might favor the formation of {110} Ti planes additionally [56].

In thermodynamic equilibrium, B-site cation arrangement of PZT is characterized by {111} patterns and {110} Ti-planes. However, the driving force towards one particular order is very small. Therefore, ordered regions will remain too small to be observed in bulk materials. Under conditions of enhanced diffusion and additional forces favoring a particular order, such as epitaxial films, order can be observed.

The favored order is the result of the size difference between Ti and Zr octahedra, and cation relaxation. The size effect can be quantified by simple model calculations and favors a rocksalt order of the B-site cations. Ti {110} planes introduce an asymmetry that allows for energy gain due to cation relaxation. Previously published first-principles work was performed in supercells with too restricted symmetry to observe the favoring of {110} Ti planes. MC calculations indicated that even at elevated temperatures the favoring of ordered structures is not overcome by entropy.

CHAPTER 4

Chemical order in
bismuth sodium titanate - barium titanate

In $Na_{1/2}Bi_{1/2}TiO_3$ (BNT) and the solid solution $(Na_{1/2}Bi_{1/2}TiO_3)_{1-x}$-$(BaTiO_3)_x$ (BNT-BT) [65] the A-site of the perovskite structure is occupied by cations that are nominally charged +1 (Na), +2 (Ba) and +3 (Bi). For A-site mixed perovskites this charge difference alone is not sufficient to cause ordering [7,25]. However, authors reported on chemical order in BNT and BNT-BT [31,71,77–79]. Also anomalies in X-ray diffraction, dielectric measurements, Raman and infrared spectroscopy were reported in the composition range of the morphotropic phase boundary (MPB) of BNT-BT [65,71–75]. These anomalies could be due to chemical ordering.

In this chapter chemical ordering in the BNT-BT system is analyzed. The influences of charge difference and local structure are analyzed on BNT in Section 4.1. Afterwards it is investigated whether peculiarities observed in transmission electron microscopy (TEM) images close to the morphotropic region can be explained by atomistic effects, such as chemical ordering. In Section 4.2 chemical ordering in BNT-BT close to the MPB is analyzed using density functional theory (DFT) calculations. In the following section the analysis is combined with high resolution transmission electron microscopy (HRTEM) imaging. Finally, the results are concluded.

4.1 Chemical order and local structure in bismuth sodium titanate

4.1.1 Electrostatic results

In $Na_{1/2}Bi_{1/2}TiO_3$ (BNT) the A-site of the perovskite structure is occupied by equal amounts of sodium and bismuth. As bismuth and sodium are aliovalent cations, it is a good example to analyze the influence of electrostatic effects on cation ordering.

The BNT structure is modeled as a $2 \times 2 \times 2$ supercell of the cubic perovskite. To assess the influence of electrostatics, the Madelung energy is calculated in a simple ionic model. For the calculations the General Utility Lattice Program (GULP) [114] is used with purely electrostatic potentials. At the atomic positions the nominal charge of the atoms is placed. Thus, the O site is taken as -2, the B-site +4 (Ti) and the A-site by +1 (Na) or +3 (Bi) depending on the permutation, or by +2 as a reference. In Figure 4.2 the energies calculated for different BNT permutations are plotted, the electrostatic energy of the reference calculation is taken as zero. Figure 4.1 shows the used A-site occupations. It can be seen that the most stable configuration is the 111-ordered structure while the 001-ordered structure is the least stable one. Thus, electrostatics predict the rocksalt ordered structure to be favored.

In literature rocksalt ordering has been observed for B-site mixed perovskites [29,76], but for A-site mixed perovskites {100} ordering is observed [7,25]. Thus, to understand ordering tendencies in A-site mixed perovskites, electrostatic considerations alone are not sufficient.

4.1.2 Density functional theory results

Density functional theory (DFT) calculations were performed using the Vienna ab-initio simulation package (VASP) [101] within the local density approximation (LDA) using projector augmented wave (PAW) potentials [124] including the Bi $5d^{10}6s^26p^3$, Na $2p^63s^1$, Ti $3s^23p^64s^23d^2$ and O $2s^22p^4$ electrons. Integration in reciprocal space was performed on a $8 \times 8 \times 8$ Monkhorst Pack mesh, an energy cutoff of $750\,eV$ was used. Calculations were performed with relaxation of atomic positions at the
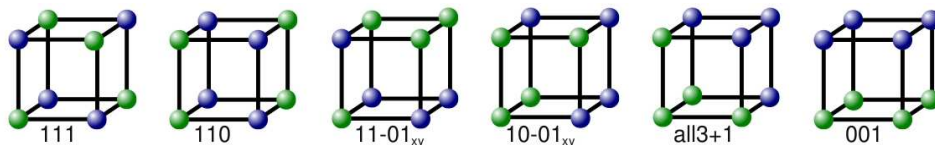

Figure 4.1: *Possible A-site occupations in a $2 \times 2 \times 2$ supercell of BNT.*
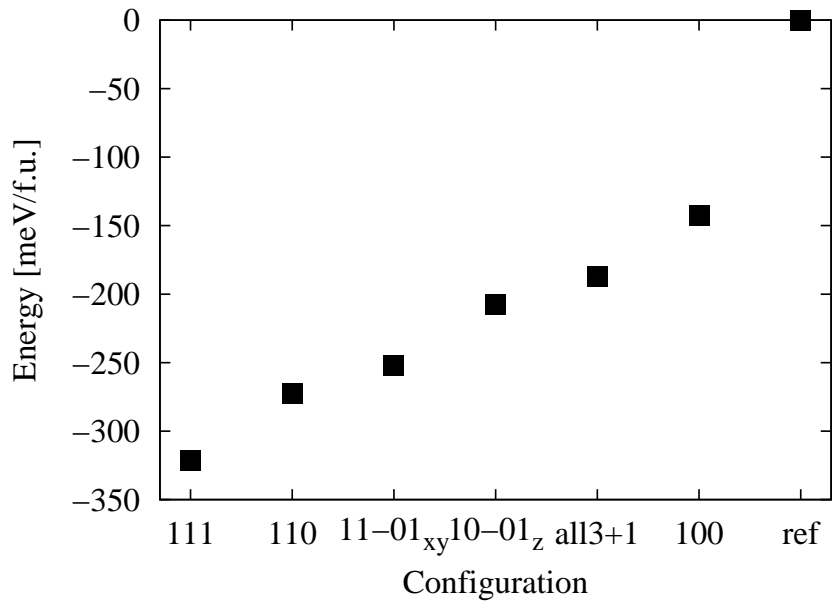
Figure 4.2: *Madelung energies ($\varepsilon_r = 10$), calculated for the different A site occupancy pictured in Figure 4.1. Formal charges are placed on the A-sites (+1 and +3 ions), an average charge (+2) is used for the reference.*

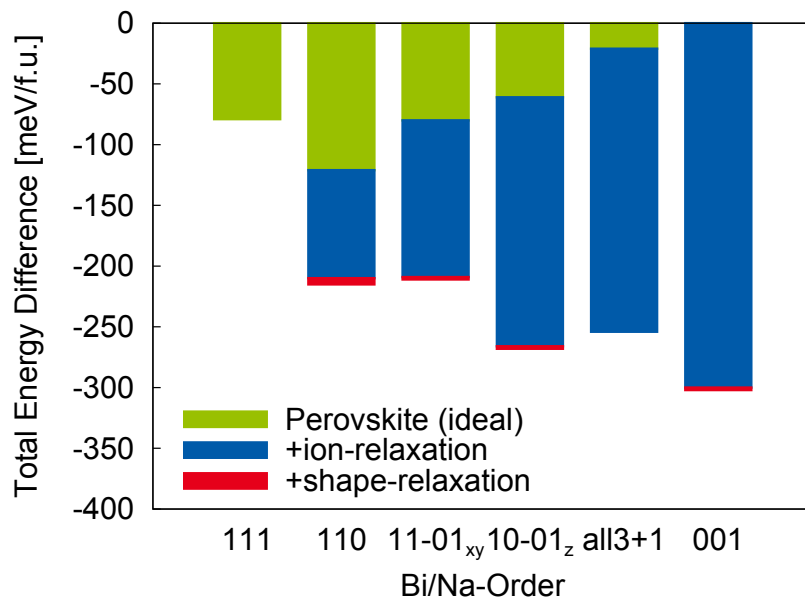**Figure 4.3:** *DFT energies of BNT, calculated for the different A site occupations pictured in Figure 4.1. Energies in the ideal perovskite structure are green, blue and red marks energy gain due to relaxation. The picture is taken from [128].*
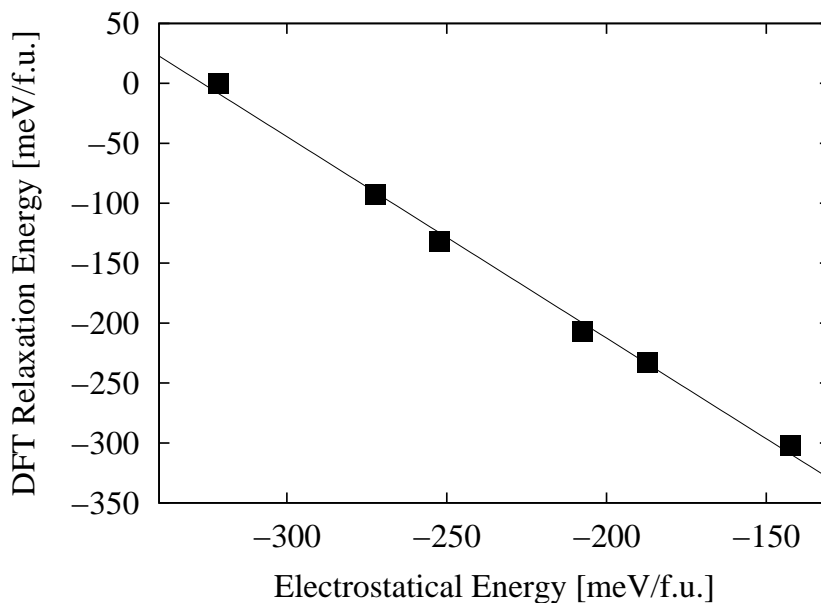
Figure 4.4: *Relation between Coulomb energies pictured in Figure 4.2 and DFT relaxation energies pictured in Figure 4.3.*

experimental cell volume (lattice constant $a = 3.9137$ Å). All A-site configurations possible for BNT in a $2 \times 2 \times 2$ perovskite supercell are used for the calculations. The calculations presented in this subsection were carried out by Melanie Gröting. The interpretation was done in cooperation.

Figure 4.3 shows DFT energies of the different permutations (contributions from ionic and cell shape relaxation are given separately). In the calculations of the ideal perovskites the ranking is similar to the ranking observed in the electrostatic calculations. However, structural relaxations result in variation of the energetic hierarchy. In Figure 4.4, the relaxation energy is plotted as a function of electrostatic energy. It can be observed that the more unstable a structure is in the electrostatic calculations the more energy it can gain from structural relaxation. The rocksalt ordered structure shows no relaxation.

4.1.3 Discussion

To understand the different energy gain through relaxation it is helpful to take a look at the oxygen environment in BNT. In the perovskite structure the oxygen anion is situated in the center of a flattened octahedron formed by four A atoms in one plane and two B atoms on opposite sites of that plane (see Section 1.1.2). For BNT

six oxygen environments are possible: All A-sites are occupied by Na or Bi (4Na and 4Bi); the four A-sites are occupied by three Na and one Bi or vice versa (3Na/1Bi and 1Na/3Bi); two A-sites are occupied by Na and two by Bi (2Na/2Bi), arranged either in a checkerboard pattern (trans) or along corners (cis). The oxygen anion can displace, if it is not situated at an inversion center. Thus, in three of the possible environments the oxygen ion cannot displace, namely 4Na, 4Bi and 2Na/2Bi(trans). In the environments 3Na/1Bi, 1Na/3Bi and 2Na/2Bi(cis) oxygen displacement is possible. The oxygen environments 2Na/2Bi(cis) and 2Na/2Bi(trans) and their relaxation possibilities were shown in Figure 1.3.

In the rocksalt ordered structure all oxygen anions are in the 2Bi/2Na (trans) coordination, thus, the structure has no possibilities for local relaxation that allow for energy gain. In the "001" structure, that shows the highest relaxation energy, the majority of oxygen anions can be found in the 2Bi/2Na(cis) coordination. The other structures show relaxation energies between those two cases. The less oxygen environments are of the 2Bi/2Na(trans) the higher the energy gain through relaxation. Comparing the environments that allow for relaxation the 2Bi/2Na(cis) is preferred.

For a more detailed analysis of the local structure of BNT see the work by M. Gröting [128].

4.1.4 Summary and conclusion

In this section chemical ordering and the local structure of BNT was analyzed in a $2 \times 2 \times 2$ supercell using electrostatic and DFT calculations.

It was shown that structural relaxation plays an important role, it is related to the local symmetry of the atoms. The energetic differences calculated between ordered structures are comparable to the differences observed in the $2 \times 2 \times 2$ supercell calculations of $PbZr_{1-x}Ti_xO_3$ (PZT) in Section 3.3. Likewise it is assumed that local order in BNT might occur, in small regions.

4.2 Chemical order and structure distortions in $(Bi_{1/2}Na_{1/2}TiO_3)_{0.94}$-$(BaTiO_3)_{0.06}$

In this section, different configurations of $(Na_{1/2}Bi_{1/2}TiO_3)_{0.94}$-$(BaTiO_3)_{0.06}$ (BNT6BT) are modeled in DFT calculations. The results will be used to investigate peculiarities observed in high resolution transmission electron microscopy (HRTEM) images close to the morphotropic phase boundary (MPB).

The section starts with a presentation of the modeling of an approximate structure to perform calculations close to BNT6BT. Afterwards, the different configurations are analyzed and a preferred configuration is presented. Finally, it is summarized which DFT calculations will be used for HRTEM image simulations, and the calculations are concluded.

4.2.1 Modeling $(Bi_{1/2}Na_{1/2}TiO_3)_{0.94}$-$(BaTiO_3)_{0.06}$

The commonly used arrangement of atoms of a 1:1 ratio, as in BNT, is the {111} ordered rocksalt structure. However, this structure is unfavored in A-site mixed perovskites [7,25] like BNT (Section 4.1). X-ray diffraction studies of BNT6BT single crystals by Chiang [71] suggested the existence of an ordered phase described in a $2 \times 2 \times 2$ supercell of the perovskite structure. In this supercell the A-site atoms are ordered in a $Pm\bar{3}m$ symmetry. The A-site atoms are positioned on the corners, the edge centers, the face centers and the body centers of a cube. These positions are nonequivalent and have different average concentrations of Bi, Na and Ba. Figure 4.5 shows the proposed order. It corresponds to the composition $Bi_{0.4463}Na_{0.4913}Ba_{0.0625}TiO_3$.

To calculate $(Na_{1/2}Bi_{1/2}TiO_3)_{1-x}$-$(BaTiO_3)_x$ (BNT-BT) close to its MPB, it is modeled in five supercells, constructed out of $2 \times 2 \times 4$ subcells, and one supercell, constructed out of $2 \times 4 \times 4$ subcells. In the smaller cell, one A-site is occupied by Ba,
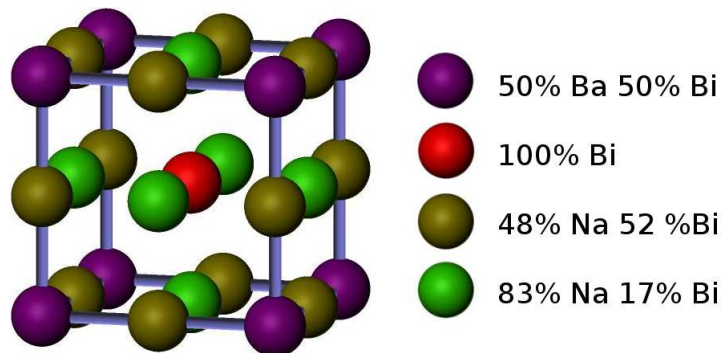

Figure 4.5: *Order proposed from X-ray diffraction studies of BNT6BT single crystals [71].*
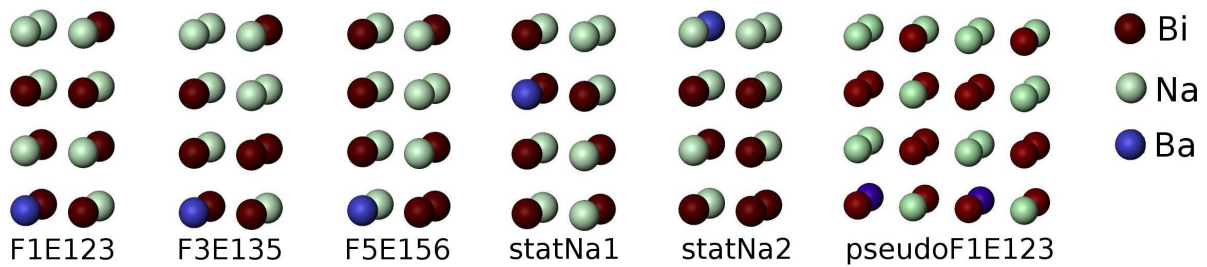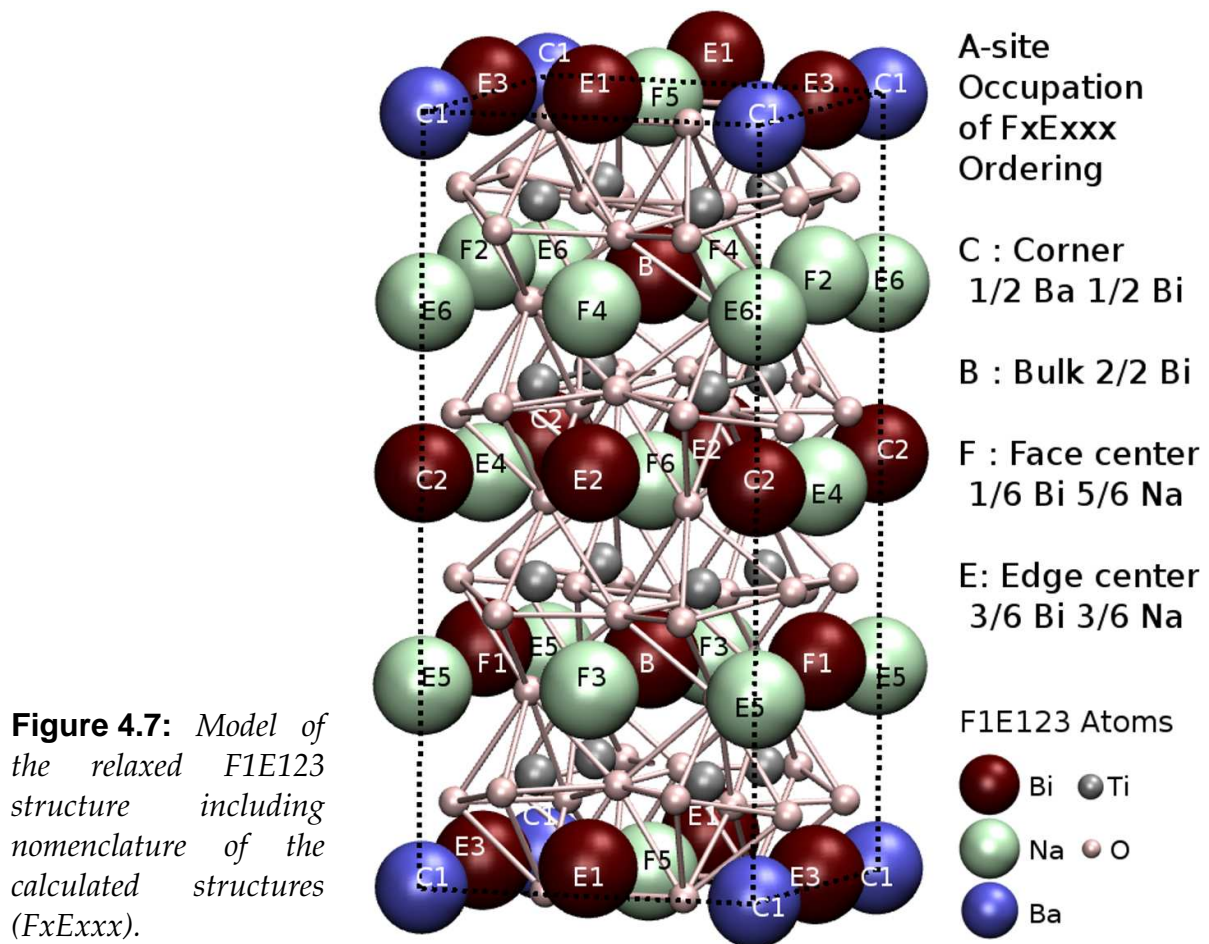
50% Ba 50% Bi

100% Bi

48% Na 52 %Bi

83% Na 17% Bi

Figure 4.6: *A-site occupations of the calculated permutations; only the A-atoms are shown.*

and 15 A-sites are occupied by Bi or Na. Thus, the $BaTiO_3$ content is close to 6 % but BNT has the wrong stoichiometry. The small size is chosen because more calculations can be performed in reasonable timescales, which allows for the calculation of different occupations. Additionally, in this supercell the exact concentration is $Bi_{0.4375}Na_{0.5}Ba_{0.0625}TiO_3$, close to the concentration for which order was proposed from single crystals [71]. To balance the Bi/Na inequality, calculations with electric compensation are performed. Also, calculations using a $2 \times 4 \times 4$ supercell are performed, avoiding the inequality between Bi and Na. The A-site occupations of the tested supercells are shown in Figure 4.6. In two of the supercells (statNa1 and statNa2) the A-site occupation is arbitrary. Three permutations are based on the ordering proposed by Chiang *et al.* [71] (F1E123, F3E135 and F5E156).

A direct application of Chiang's order would necessitate half a barium atom, thus, the unit cell of the proposed order is doubled along the z axis. Figure 4.7 shows one of the permutations with enlarged A-site atoms. In this structure, two body-centered sites called bulk (B), two corner-sites (C), six face-center sites (F) and six edge-center sites (E) have to be occupied by one barium atom, seven bismuth atoms and eight sodium atoms. The occupation of the bulk and corner sites is fixed. The bulk sites are occupied by bismuth. One of the corner sites is occupied by bismuth, the other by barium. The site occupied by the barium atom is called C1. In the occupation of the face-center sites and edge-center sites some liberties exist. These sites are named in reference to their position to the barium atom. Of the six face-center sites one is occupied by bismuth and five by sodium. The site occupied by bismuth is used in the permutations name. Half of the six edge-center sites are occupied by bismuth the other by sodium. The sites occupied by bismuth are again used in the permutation names. Thus the permutation name (FxExxx) identifies one specific permutation. The $2 \times 4 \times 4$ (pseudoF1E123) supercell is constructed based on permutation F1E123. First, F1E123 is doubled along the y-axis, doubling all atomic sites, then a sodium atom occupying one of the E4 sites is replaced by bismuth.

A-site
Occupation
of FxExxx
Ordering

C : Corner
1/2 Ba 1/2 Bi

B : Bulk 2/2 Bi

F : Face center
1/6 Bi 5/6 Na

E: Edge center
3/6 Bi 3/6 Na

F1E123 Atoms

● Bi ● Ti

● Na ● O

● Ba

Figure 4.7: *Model of the relaxed F1E123 structure including nomenclature of the calculated structures (FxExxx).*

4.2.2 Results and discussion

The described structures are used to perform DFT calculations, using the VASP [101]. All calculations are performed within the LDA and PAW pseudo-potentials [124] including the Ba $5s^25p^66s^2$, Bi $6s^26p^3$, Na $3s$, Ti $3d^24s^2$ and O $2s^22p^4$ electrons. As the supercells were relatively large, the reciprocal space is sampled at the Γ point only.

In the $2 \times 2 \times 4$ supercells an inequality of bismuth and sodium atoms occurs that might influence the calculation results. To check its effect, the calculations are treated as defect calculation of a barium atom on one A-site of BNT. The "defects" are calculated without balancing the Na/Bi inequality, and at nominal charge, *i.e.* balancing the Na/Bi inequality. Cell parameters and ionic positions were allowed to relax at different fixed volumes.

Figure 4.8 compares the calculated energies of the configurations modeled in a $2 \times 2 \times 4$ at nominal charge. Like in BNT, the calculated energies differ depending on the A-site occupation. The most stable calculated permutation is F1E123, which is
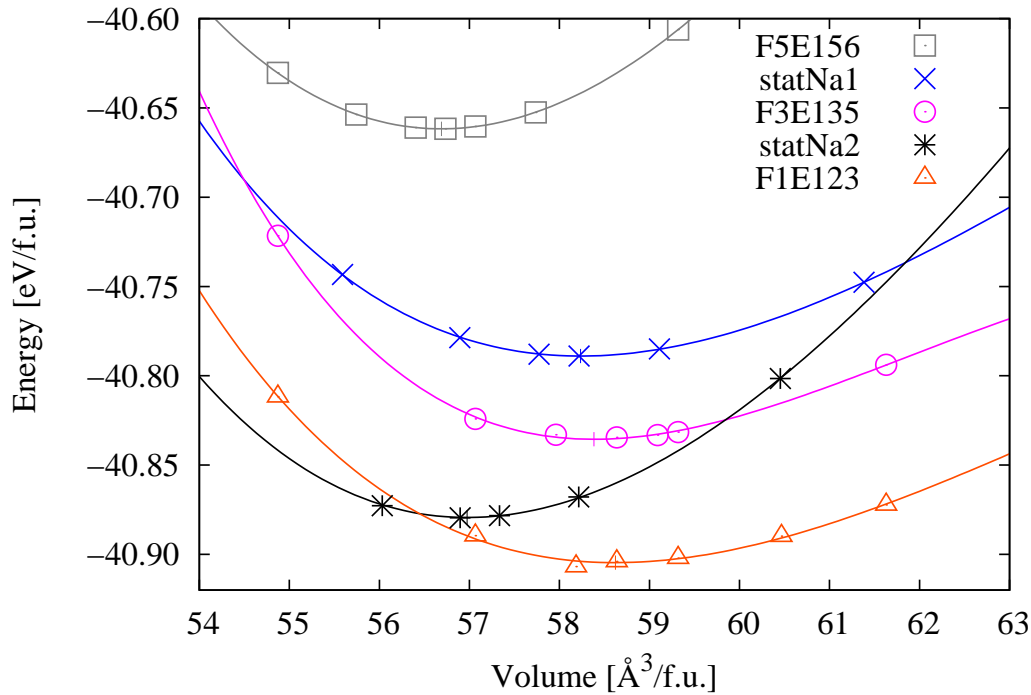
Figure 4.8: *Calculated energy as a function of volume for the five different permutations.*

based on the ordering proposed from single crystals. It shows the lowest calculated energy at a stable volume of about 58 Å^3/f.u.. It can be seen from the figure, that the stable volume is also dependent on the calculated configuration, however, permutation F1E123 and F3E135 have a similar stable volume. The calculations without compensation of the Bi/Na inequality display the same ranking and tendencies. The permutation pseudoF1E123 in the $2 \times 4 \times 4$ supercell models a different concentration, which is why the energy and volume cannot be compared to $2 \times 2 \times 4$ supercell calculations.

Figure 4.7 showed the structure of the permutation F1E123, which is the most stable structure calculated. Along columns of the coordinate axises the A-sites are occupied rather homogeneously. Along the z-axis the sodium occupation of all columns is 1/2. Along the x- and y-axis six of the eight columns are occupied by one sodium and one bismuth. All atoms are displaced from their high symmetry positions. The movement of the oxygen atoms results in octahedral tilting. The octahedra tilt in such a fashion that it allows most oxygen atoms to move towards sodium atoms while the octahedra show a minimum of deformation. The B-site cations displace mainly in x or y direction in alternating c-layers. The A-site cations sublattice is noticeably deformed, with no discernible regularities.
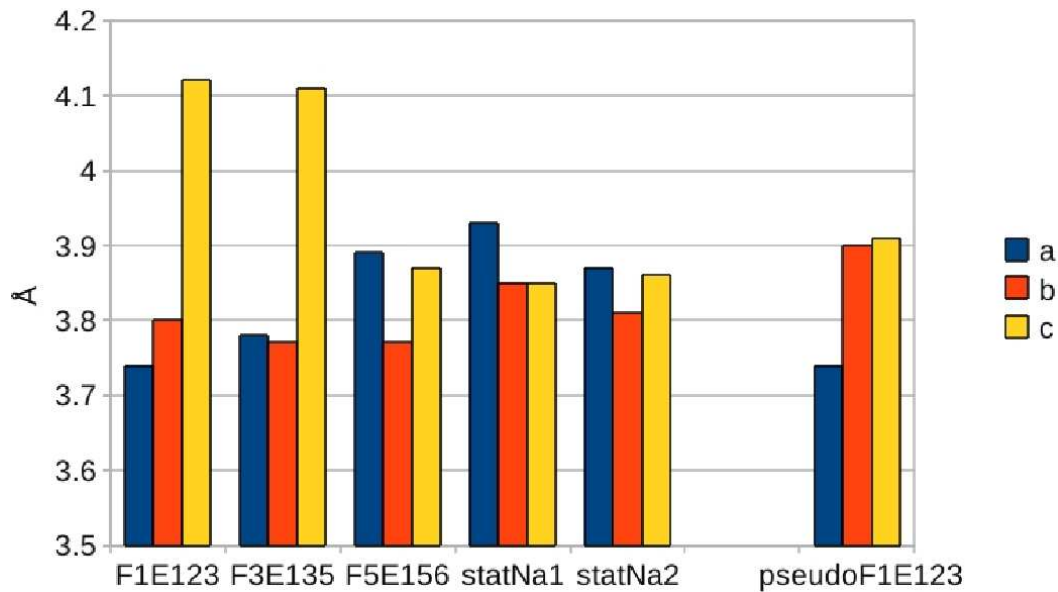
Figure 4.9: *Lattice parameters for charged* $2 \times 2 \times 4$ *permutations and the* $2 \times 4 \times 4$ *permutation.*

To compare the different structures, the structural changes are quantified by the lattice parameters and by the radial displacement. Figure 4.9 shows the lattice parameters of the configurations calculated in the small supercells with Bi/Na compensation and the configuration calculated in the large supercell. Permutation F1E123 and F3E135 show similar lattice parameters and a similar cell volume. In permutation F1E123, the lattice parameter c is considerably elongated compared to the a and b lattice parameters. This might be due to the different directions not being equivalent. In permutation F1E123 four subcells are modeled along the z direction and two along the x and y direction. The lattice parameters of the non-compensated supercells exhibit the same tendencies in the lattice parameters. Permutation pseudoF1E123 shows a similar lattice parameter a as permutation F1E123. On the other hand, b and c are the mean value of the respective parameters in F1E123. In this calculation the directions are also not equivalent, two subcells are modeled along the x direction and four along the y and z direction.

Figure 4.10 shows the radial displacements of the ions from their ideal perovskite positions for the compensated small supercells and the large supercell, taking the overall atomic movement as zero. The non-compensated supercells exhibit the same tendencies in the radial displacements. The largest displacement in all calculated structures is observed for the bismuth and oxygen atoms. The radial displacements of the pseudoF1E123 structure are similar to those of F1E123, but smaller. The observed displacements are large compared to displacements in lead based per-
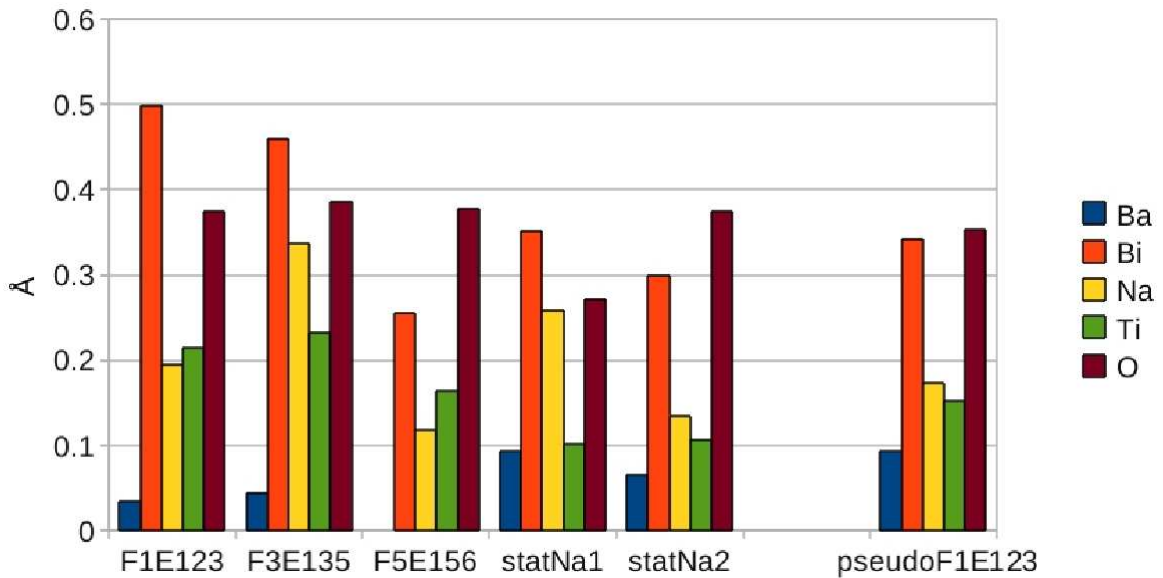
Figure 4.10: *Radial displacements of the ions from the ideal perovskite positions for charged* $2 \times 2 \times 4$ *permutations and the* $2 \times 4 \times 4$ *permutation.*

ovskites. The calculated displacements might be too large due to finite size effects, which might already be reflected in the observation that the displacements of the F1E123 are similar, but larger than those in pseudoF1E123. However, large atomic displacements also might be an intrinsic property of lead-free perovskites.

4.2.3 Summary and conclusion

BNT6BT was calculated considering different A-site occupations. Comparison of calculations in a $2 \times 2 \times 4$ supercell with or without balancing the Bi/Na inequality have shown no differences in ranking, lattice parameters or radial displacements. A $2 \times 4 \times 4$ supercell with equal amounts of Bi and Na reveals the same displacement characteristics. The different asymmetries of the $2 \times 2 \times 4$ and the $2 \times 4 \times 4$ supercells show no discernible influence on the characteristics of atomic displacements. Therefore, the calculated permutations in a $2 \times 2 \times 4$ supercell, including a compensation to balance the Bi/Na difference, are used to model BNT6BT for HRTEM image simulation.

Permutation F1E123 is the preferred configuration calculated in a $2 \times 2 \times 4$ supercell. It was constructed according to an ordering proposed from single crystals. The permutation shows a homogeneous distribution of heavy (Bi/Ba) and light (Na) atoms on the A-sites along [001] columns.

4.3 Correlation to HRTEM imaging observations

In this section HRTEM imaging on BNT6BT is analyzed. Atomistic effects are analyzed by comparing experimental images to images simulated from the configurations presented in Section 4.2.

The section is started by the presentation of an experimental HRTEM image. Afterwards the simulation of an HRTEM image from a calculated structure is shown on the example of the F1E123 configuration. Different contrasts found in the experimental image are analyzed and, if possible, correlated to simulated images from different structures, or of a slight structure misorientation. Finally, the results are summarized and conclusions given.

The HRTEM images and all modeled images shown in this subsection were made by Jens Kling, Division of Geo-Material-Science. The interpretation was done in close cooperation.
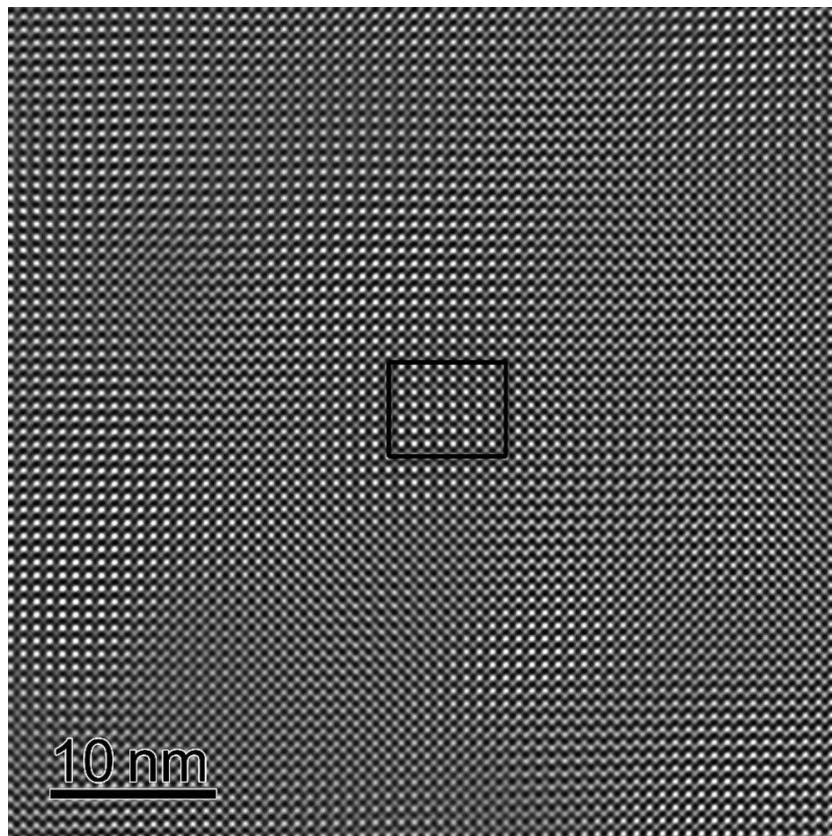

Figure 4.11: *Inverse Fourier transformed image of the taken HRTEM image. Areas of approximately 10-20 nm with uniform contrast variation were detected. The detail in the black rectangle is taken for comparison with the simulated structures. Picture taken from [129].*

4.3.1 Experimental HRTEM image

Figure 4.11 depicts the inverse Fourier transformed image of the experimental HRTEM image. For the transformation, reflections up to {110} without the primary beam were chosen. As can be seen from Figure 4.11, areas of approximately 10 to 20 nm with uniform contrast exist, but the local intensity distribution is not homogeneous over the entire region. The material consists of areas of different contrast. These nanosized regions can be due to, for example, different chemical ordering, different crystal structures or slightly tilted regions with respect to the incident electron beam. Local variations in sample thickness can cause contrast modulations as well.

4.3.2 Simulation of HRTEM images

Different configurations modeling BNT6BT in a $2 \times 2 \times 4$ supercell (presented in subsection 4.2) are used to simulate HRTEM images. The viewing direction is [001] and the cell is doubled in a and b direction to receive a larger simulated image. The values taken for the thickness are assumed to represent the real sample thickness imaged by transmission electron microscopy (TEM). A thickness of about 5 to 20 nm is realistic. The following figures are details of the whole defocus-thickness maps calculated from the DFT models.

Atomic relaxation has a strong effect on material stability (Section 4.1). To assess its visibility in HRTEM imaging, image simulations were performed at ideal atomic positions and with relaxed atomic positions. Structures with ideal atomic positions are called unrelaxed, structures obtained from DFT calculations are called relaxed.

Figure 4.12 shows an HRTEM image simulation of the F1E123 permutation compared to a part of the experimental image. It can be seen that the patterns for the unrelaxed and relaxed structures differ. Variations in intensity are a consequence of variations in atomic position and occupancy. This proves that the unrelaxed and relaxed state can be distinguished.

The simulated HRTEM images of the unrelaxed (a) and the relaxed (c) F1E123 model are compared with the experimental HRTEM image. The contrast peculiarities observed in the figure simulated from the unrelaxed structure stem solely from the A-site occupation of the ideal perovskite. The image simulated from the relaxed structure reflects also information from cation displacement and octahedral tilting. At first sight, both simulated images seem to match the experimental image. The intensity ratio between brighter and weaker spots is better reproduced by the unrelaxed structure, but its tendency can be observed in both. They show a brighter spot with a weaker one in-between. Due to the off-centering of the ions and octahedral tilting, some spots are elongated in the relaxed structure. In the real image
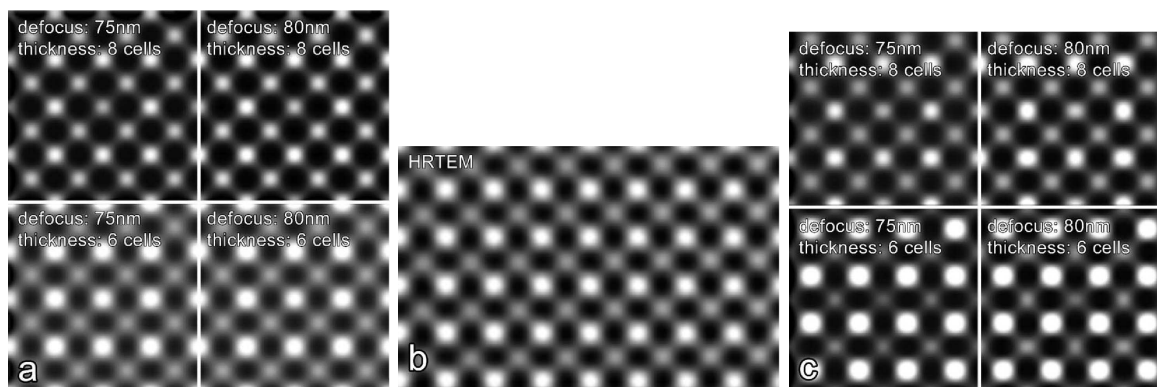
Figure 4.12: *Comparison between HRTEM measurements and image simulation from calculated DFT data of F1E123. (a) Simulation of unrelaxed structure, (b) inverse Fourier transformed experimental image (black rectangle in Figure 4.11), and (c) simulation of relaxed structure. Picture taken from [129].*

this cannot be observed, but some weaker spots are slightly off-centered. This is not reproduced by the simulations. It is assumed that displacements similar to the calculated one occur with smaller values.

4.3.3 Analysis of anomalies in HRTEM images

Chemical ordering

The experimental HRTEM image does not appear homogeneous, but shows areas of different contrast. Hence, there are areas that reveal a better fit and others that deviate more from the before modeled structure. Moreover, there are also areas that fit worse than the ones shown here.

To check for possible order effects, HRTEM image simulations were also performed for other A-site occupancies.

The resulting patterns differ considerably, which allows one to distinguish different structural models. Figure 4.13 shows the pattern for the unrelaxed structures F3E135 (a), F5E156 (b), statNa1 (c) and statNa2 (d). All these structures show a different pattern. Thus, it is concluded that the occupation of the atom columns in beam direction mainly affect the calculated images. In direction [001] of F1E123 each atomic column consists of two light A-atoms (Na) and two heavy A-atoms (Bi and/or Ba). This A-site occupancy matches the real structure best of all calculated structures, as depicted in Figure 4.12. The other configurations in the unrelaxed and relaxed state show different intensity patterns, that are not observed in the experimental
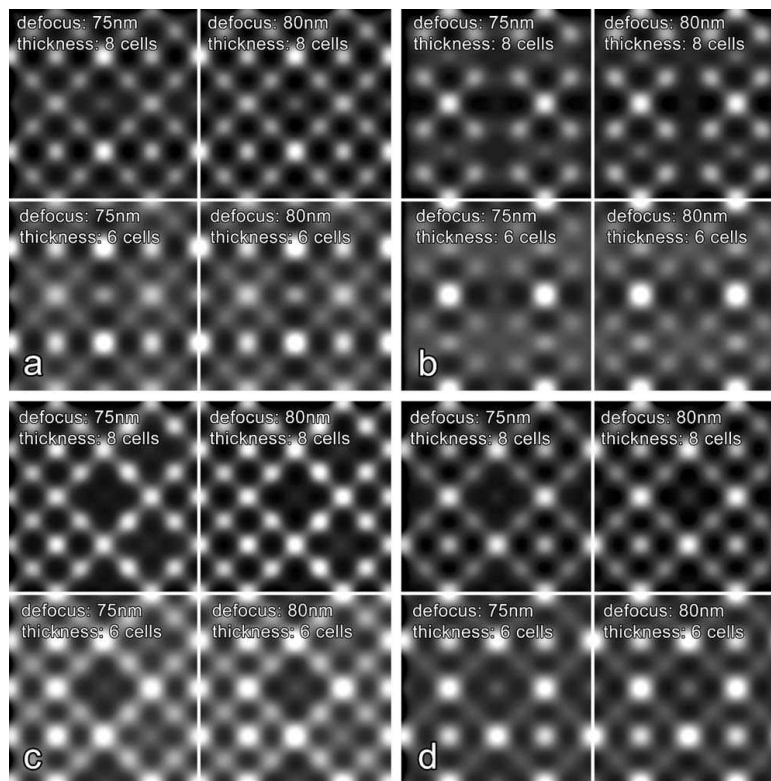
Figure 4.13: *Comparison of the images simulated from unrelaxed structures. (a) F3E135, (b) F5E156, (c) statNa1, and (d) statNa2. The patterns look different for all structures and can be distinguished. Picture taken from [129].*

image. Therefore, it can be concluded that the local variations in image contrast are due to another effect than the chemical ordering analyzed in this paragraph.

Crystal misorientation

Another possible reason for different contrast in HRTEM images might be a slightly different structure. It is theorized, that the bulk material consists of small regions with slightly different crystal structure or slightly different orientation of the lattice with respect to the incident electron beam. A misorientation can be simulated by changing the viewing direction. Figure 4.14 shows two different details of the inverse Fourier transformed HRTEM image of Figure 4.11 and two simulated images. The HRTEM pattern in (a) can be reproduced by simulation of the relaxed F1E123 configuration tilted by $0.19\,°$ towards $[0\bar{2}0]$. Thickness and defocus are the same as in previous simulations. Simulation of a tilt of $0.26\,°$ towards $[220]$ of the initial F1E123 structure produces a pattern close to the real HRTEM image (b). Thickness and defocus are slightly different, but realistic for the specimen.
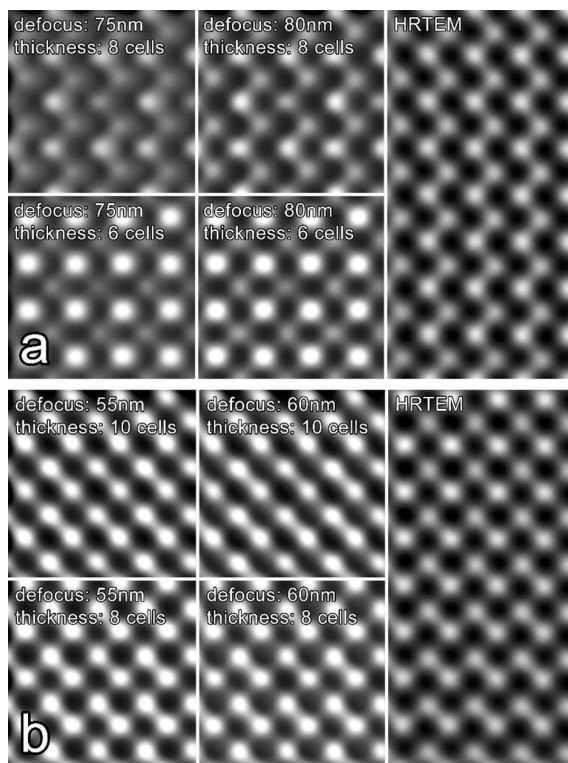
Figure 4.14: *Tilting from the ideal [001] and comparison to different areas of Figure 4.11. (a) Relaxed F1E123 tilted 0.19° toward [0$\bar{2}$0]. The pattern matches the HRTEM image, (b) unrelaxed F1E123 tilted 0.26° toward [220]. The pattern matches the HRTEM image. Slight tilting reproduces different areas of the real image. Picture taken from [129].*

4.3.4 Summary

HRTEM images were simulated from calculated structures and compared to the experimental HRTEM images. The images simulated from the structure F1E123 fitted best to the experimental image. A difference between the unrelaxed and the relaxed structures is visible in the simulated structures. Images simulated from different A-site occupations showed no similarities to the experimental image. However, different misorientations of the F1E123 structures in the simulated images resulted in images that matched different areas of the experimental image. Simulations from unrelaxed and relaxed structures can reproduce patterns similar to the real image. It is assumed that the calculated atomic displacements and octahedral tilting occur with smaller values.

4.4 Summary and conclusions

Chemical ordering in the BNT-BT system was analyzed, using electrostatic calculations, DFT calculations and HRTEM imaging.

The analysis of BNT using simulations showed that the energetic differences calculated between differently ordered structures are small. Structural relaxation plays an important role. It is assumed that local order in BNT might occur, in small regions.

The DFT calculations of differently ordered structures for BNT6BT showed similar energy differences as the BNT calculations. Likewise, it is assumed that the energetic differences are too small to be responsible for long range order. The most stable configuration in the BNT6BT calculation was constructed according to an order proposed for single crystals [71]. The permutation is characterized by a homogeneous distribution of heavy (Bi/Ba) and light (Na) atoms on the crystallographic A-site along [001] columns. This permutation produces a simulated HRTEM image close to the experimental image observed. As HRTEM imaging is done along the [001] direction, it is taken as another indication that the A-site distribution in BNT6BT is homogeneous.

HRTEM image simulation of BNT6BT configurations verified that relaxation plays an important role. The usage of relaxed and ideal (so called unrelaxed) structures resulted in different images. However, both fit to the experimental image. It is possible that the atomic displacements observed in the calculations are too large due to finite size effects. Therefore, it is assumed that the observed displacements occur, but with smaller values.

The different areas that are observed in the experimental image of BNT6BT could not be matched to different permutations. However, they could be matched by a slight tilting of the simulated preferred structure.

The following is concluded from the above analysis: In BNT-BT the crystallographic A-site atoms are on average homogeneously distributed. Small regions of BNT might show short range order. BNT6BT might obey an order proposed from single crystals measurements, while the overall distribution of atoms is homogeneously. The BNT-BT structure shows relaxation. Samples consists of regions that are oriented slightly differently, which is possibly due to slightly different structures.

CHAPTER 5

Ferroelectric instability in bismuth sodium titanate - barium titanate

The ferroelectric properties of a material are directly connected to distortions of the centrosymmetric prototype structure [1]. Lattice dynamic calculations can be used to identify the resistance against deformation of a material [37–41]. A simplified illustration of the ferroelectric distortion is a displacement of one of the cation types from its high symmetry position [42,43]. Calculations modeling such a displacement can be used to analyze if a material is ferroelectrically active, and whether it is A-site or B-site active.

In this chapter the dependencies of ferroelectric cation site instabilities are investigated for $(Na_{1/2}Bi_{1/2}TiO_3)_{1-x}$-$(BaTiO_3)_x$ (BNT-BT).

5.1 Analyzing cation site stabilities

In this chapter cation site stabilities are analyzed as a function of composition and volume. The composition-pressure relation of the ferroelectric instability and characteristics of the morphotropic phase boundary (MPB) position are assessed.

The MPB signifies a material composition at which the structural changes from a ferroelectric structure to another structure are facilitated [22]. Calculations analyzing the ferroelectric instability might be useful to identify such a composition.

Ferroelectricity is caused by the instability of the cubic prototype structure [130]. Variation in ferroelectric properties have been observed due to composition changes and hydrostatic pressure. It has been proposed that these effects are comparable [15,16,23,24,52]. An atomistic analysis of the stability of the cation site in the cubic perovskite structure can help to understand dependencies of ferroelectric properties [6,36,42,43].

In the perovskite structure the A- and B-sites can become ferroelectrically active by displacing in certain directions. A displacement in $\langle 100 \rangle$ direction mimics tetragonal displacement, displacement in $\langle 111 \rangle$ direction mimics rhombohedral displacement and displacement in $\langle 110 \rangle$ direction mimics orthorhombic displacement. Density functional theory (DFT) calculations of the perovskite structure including these displacements analyze the ferroelectric activities of the cations with suppressed inter-atomic cooperation.

Calculations are performed on $(Bi_{1/2}Na_{1/2}TiO_3)_{1-x}(BaTiO_3)_x$ with $x = 0$, 0.0625, 0.25, 0.75 and 1. For most calculations a supercell constructed of $2 \times 2 \times 2$ ideal perovskite subcells was used. In the supercells the B-sites are occupied by Ti, the O sites by oxygen and the A-sites by Na, Bi or Ba, depending on the desired composition.

From the work presented in Chapter 4 it is deduced that the A-site distribution in the BNT-BT system might be characterized by local order, but is in average homogeneous. An adequate choice to model a homogeneous 1:1 occupation is the rocksalt order, it is used for the calculations of pure $Na_{1/2}Bi_{1/2}TiO_3$ (BNT). For the composition $Bi_{3/8}Na_{3/8}Ba_{2/8}TiO_3$ the A-sites are occupied by Na and Bi atoms in rocksalt ordering with one Bi and one Na atom replaced by Ba. The two possible permutations are calculated. The composition $Bi_{15/32}Na_{15/32}Ba_{2/32}TiO_3$ is calculated in a $2 \times 4 \times 4$ supercell. Na and Bi are arranged in rocksalt ordering and one Bi and one Na atom are replaced by Ba. Two of the possible permutations are calculated. At the composition $Bi_{1/8}Na_{1/8}Ba_{6/8}TiO_3$ all three possible A-site occupations are tested.

DFT calculations were performed using the Vienna ab-initio simulation package (VASP) [101] within the local density approximation (LDA) using projector augmented wave (PAW) potentials [124] including the Bi $5d^{10}$ $6s^2$ $6p^3$, Na $2p^6$ $3s^1$, Ba $5s^2$ $5p^6$ $6s^2$, Ti $3p^6$ $3d^2$ $4s^2$ and O $2s^2$ $2p^4$ electrons. Integration in the reciprocal space

was performed on a Gamma point centered $3 \times 3 \times 3$ Monkhorst Pack mesh [131], and an energy cutoff of $600\,\mathrm{eV}$ was used. Convergence showed an accuracy of $1\,\mathrm{meV}$ for the k-point mesh and $3\,\mathrm{meV}$ for the energy cutoff. In all calculations internal cell parameters were not allowed to relax and the cell volume was held fixed.

5.2 Pure phases of BNT-BT

5.2.1 Concept of cation site stability - BaTiO$_3$

For analyzing the cation-site stability of BaTiO$_3$, all Ba or all Ti atoms are displaced from their ideal positions in the cubic perovskite structure and the resulting energy is calculated. The energy difference to the ideal cubic structure is then plotted as a function of cation displacement in units of the lattice constant used in the calculations. Only small displacements are shown. A positive energy change signifies that a cation displacement is unfavored and that the cation site is stable. A negative energy change shows that the material gains energy by displacing the cation. Thus, the material is not stable in the cubic structure and will adopt a distorted structure. Ferroelectricity can exist in the distorted perovskite structures, but not in the cubic perovskite structures. Thus, the cation-site instability is called ferroelectric instability and the cation showing an instability is called ferroelectric active cation. Due to the absence of atomic relaxation in the calculations, inter-sublattice cooperation is suppressed. Thus, the calculations can be used to discern the stability of the cation sites, but a direct connection to ferroelectric active structures cannot be made.
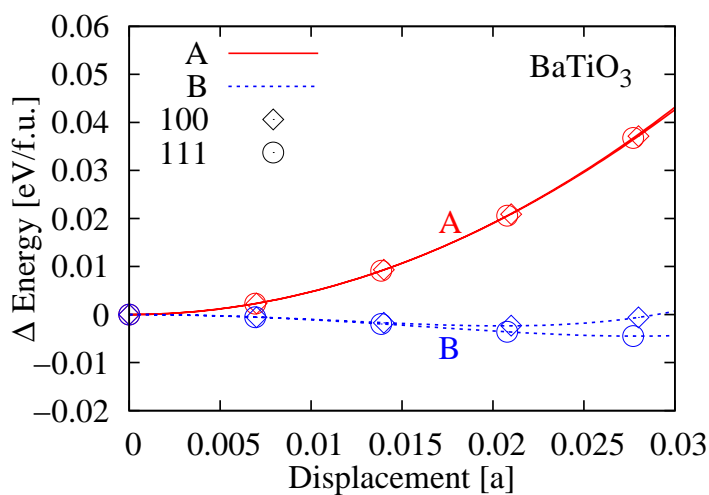

Figure 5.1: *BaTiO$_3$ at experimental volume. Energy difference to the ideal cubic structure as a function of cation displacement, given in reference to the lattice constant $a = 4.009$ Å.*

Figure 5.1 shows the energy of $BaTiO_3$ at its experimental volume as a function of cation displacement. The obtained values are in very good agreement with those calculated in the work by Ghita *et al.* [43]. The graph shows that the A-site cation is stable in its highly symmetric position, while the B-site is unstable. Therefore, it can be concluded that the B-site cation is ferroelectrically active at the experimental volume. The displacement along the [111]-direction is favored over the [100]-direction for the B-site cation. No difference in direction is noticeable for the A-site displacement in the range displayed.

5.2.2 Volume dependence of cation site stability - BNT

BNT is modeled in a $2 \times 2 \times 2$ supercell. The A-sites are occupied by equal amounts of bismuth and sodium in rocksalt order. Figure 5.2 shows the variation of the total energy as a function of cation displacement at the theoretical cell volume. Bi and Na are displaced by the same value and in the same direction to represent A-site displacement. The figure shows that the B-site is stable in BNT, while the A-site is unstable, and thus, ferroelectrically active. At larger displacements, the energy difference due to the A-site cation displacement reaches a minimum and eventually becomes positive (not depicted).

The calculations presented in Figure 5.2 are performed at the theoretical volume, which is smaller than the experimentally observed volume. As previous DFT calculations have shown that the ferroelectric distortion is sensitive to volume changes,
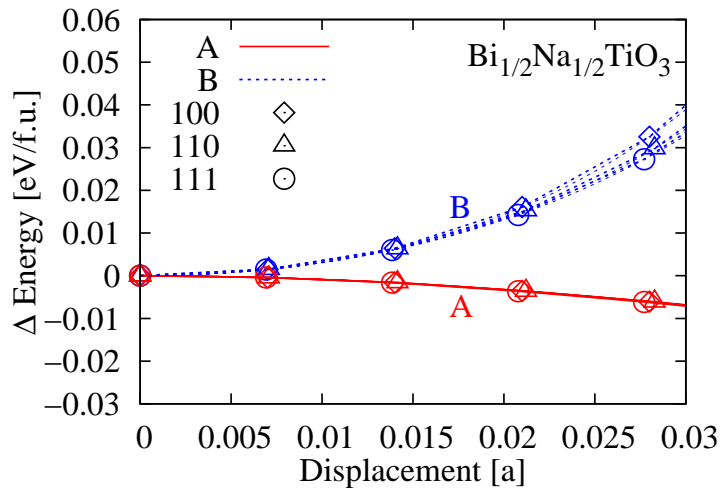

Figure 5.2: *Rocksalt ordered $Bi_{1/2}Na_{1/2}TiO_3$. The energy difference to the cubic structure is plotted as a function of cation displacement in units of the lattice constant at theoretical cell volume a=3.825Å.*
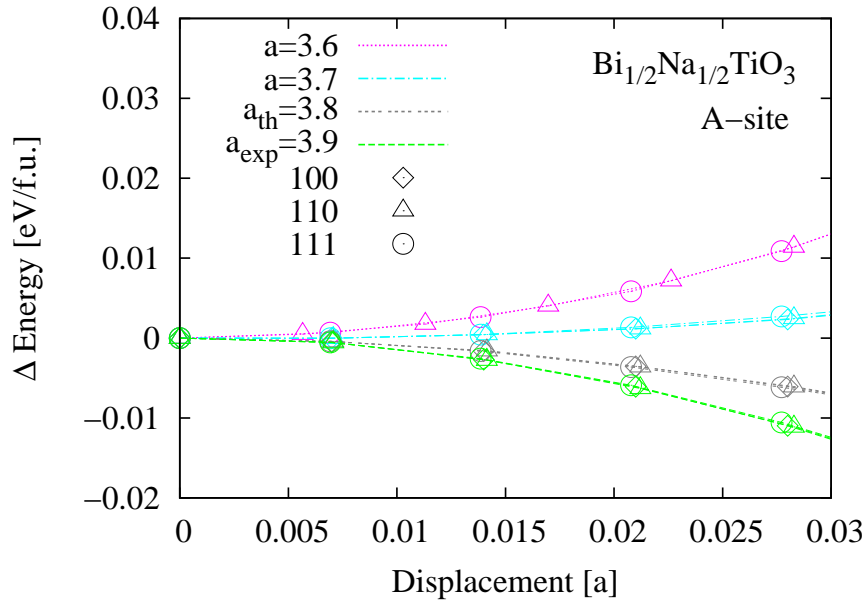
Figure 5.3: *Energy of rocksalt ordered BNT plotted as a function of A-site cation displacement for different volumes, in reference to the respective lattice constants.*

and to test the influence of hydrostatic pressure, the cation site stabilities are calculated for various volumes.

In Figure 5.3 the energy difference to the ideal cubic structure is plotted for the A-site stability as a function of cation displacement for different volumes in reference to the respective lattice constants *a*. It can be seen that the A-site is stabilized at smaller volumes and no longer ferroelectrically active, while at higher volumes the A-site is destabilized and the ferroelectric activity is increased.

5.3 Cation site stability of the BNT-BT solid solution

5.3.1 Results

BaTiO$_3$ is a B-site active, while BNT is an A-site active ferroelectric. Thus, the possible cross-over is analyzed in the solid solution. In addition, it is investigated whether changes in the cation site stability can be described as chemical pressure similar to hydrostatic pressure.
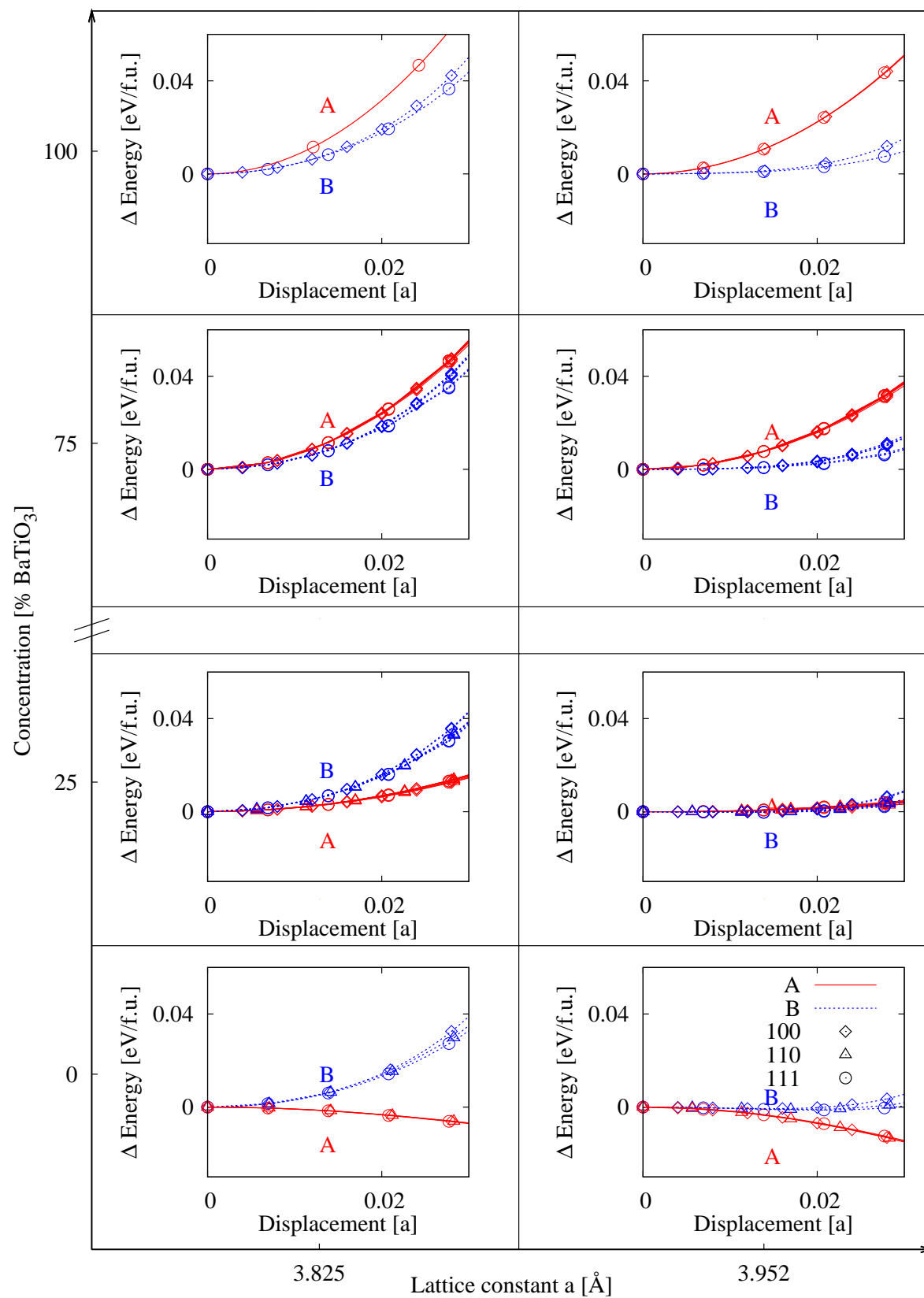
Figure 5.4: *Energy change as a function of cation displacement for different concentrations and volumes in the BNT-BT system.*

Cation site stabilities were calculated at different volumes and concentrations in the solid solution system BNT-BT. Figure 5.4 shows the cation site stabilities at two volumes and four concentrations. The energy difference to the ideal cubic structure is given as a function of cation displacement in reference to the respective lattice constants. Different permutations were considered for the concentrations $x = 0.25$ and 0.75, and are shown in the respective plots, but no significant energy difference can be discerned. From the graphs the following trends can be observed. The A-site stability mainly depends on concentration and less on volume. The B-site stability mainly depends on volume and almost not on concentration.

To quantify the results, the Landau theory is used to describe the data (see Section 1.1.3). Strain variables are omitted, as the calculation in this section were performed inhibiting structural relaxation. The Landau expansion is truncated after the fourth order term.

$$G(\eta) = G_0 + \frac{1}{2}\alpha\eta^2 + \frac{1}{4}\beta\eta^4 \; , \tag{5.1}$$

as order parameter η the atomic displacement Δx is used. Therefore, the following equation is used to describe the energy difference to the ideal cubic structure ΔE_i:

$$\Delta E_i = \frac{1}{2}\alpha_i \cdot \Delta x_i^2 + \frac{1}{4}\beta_i \cdot \Delta x_i^4 \; .$$

The second parameter β_i (scaling the fourth order term) becomes important at larger displacements. It can be considered as a geometric parameter that scales the inter-
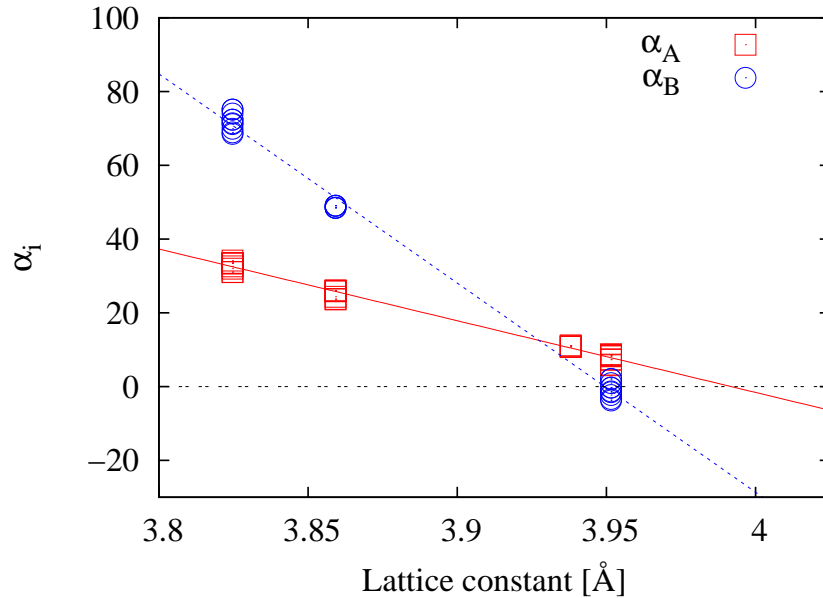

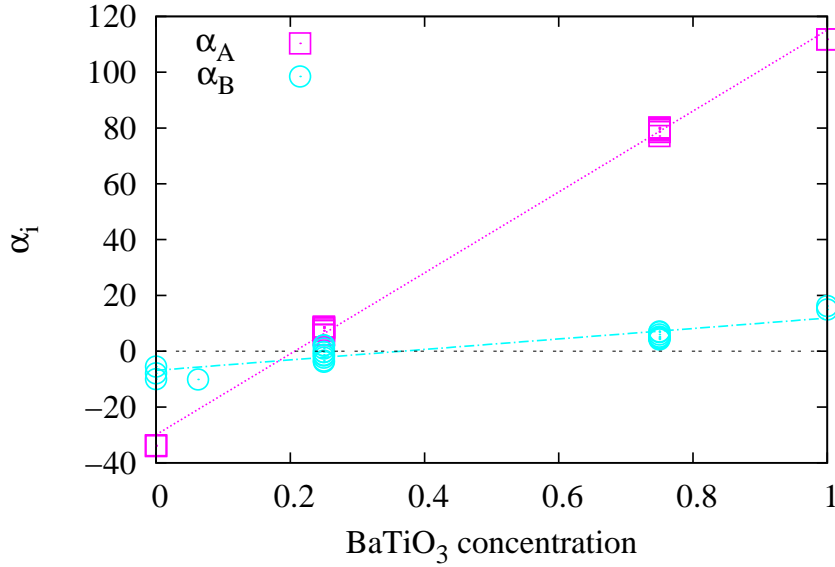**Figure 5.5:** *Volume dependence of α_A and α_B for $Ba_{0.25}Bi_{0.375}Na_{0.375}TiO_3$.*

Figure 5.6: *Concentration dependence of α_A and α_B at theoretical volume of BaTiO$_3$ (a=3.952Å).*

atomic repulsion as the cations advance towards surrounding oxygen atoms.

Figure 5.5 shows the dependence of α_i on the lattice parameter for Ba$_{0.25}$Bi$_{0.375}$Na$_{0.375}$TiO$_3$. It can be seen that α_i is a linear function of the lattice parameter. This linear character can be observed for all compositions. Figure 5.6 shows the dependence of α_i on the BaTiO$_3$ concentration at the theoretical volume of BaTiO$_3$ with $a = 3.952$ Å. A linear relation can also be observed at other volumes, for example the theoretical volume of BNT. Therefore, α_i is a linear function of both the lattice constant and the composition.

Figure 5.7 shows α_A and α_B as a function of lattice parameter and BaTiO$_3$ concentration. The cation site activities can be described as a linear function of lattice parameter and BaTiO$_3$ concentration, including a bilinear term coupling both parameters:

$$\alpha_A = 517 + 1029 \cdot x_{\text{BT}} - 138 \cdot a_{\text{lat}}/\text{Å} - 223 \cdot x_{\text{BT}} \cdot a_{\text{lat}}/\text{Å}$$
$$\alpha_B = 2206 + 46.7 \cdot x_{\text{BT}} - 560 \cdot a_{\text{lat}}/\text{Å} - 6.41 \cdot x_{\text{BT}} \cdot a_{\text{lat}}/\text{Å} \,,$$

where x_{BT} is the concentration of BaTiO$_3$ and a_{lat} is the lattice constant. A negative α_i represents a ferroelectric active cation site. It can be seen that the A- and B-sites become more active for higher volumes and lower BaTiO$_3$-content. Figure 5.9 shows a projection of α_A and α_B onto the lattice composition plane. Lines represent the same value, only negative values are shown.
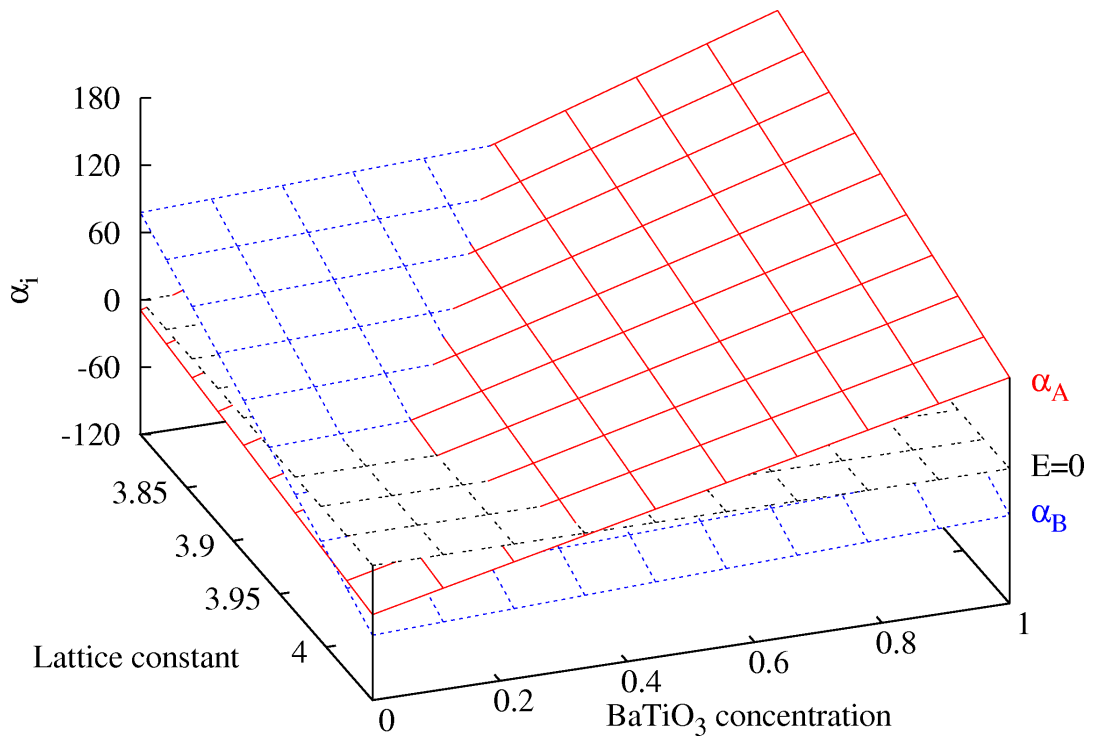
Figure 5.7: *Dependence of α_A and α_B on the lattice constant and concentration.*
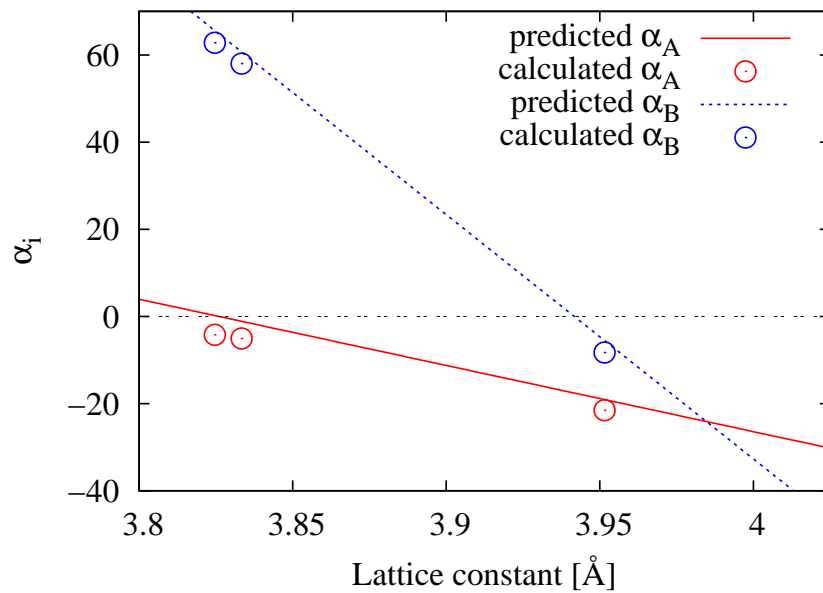

Figure 5.8: *Volume dependence of α_i of $Ba_{0.0625}Bi_{0.46875}Na_{0.46875}TiO_3$.*

The established relation between α_i, composition and volume can now be used to predict the cation site stabilities at different compositions and volume. For example, the cation-site instabilities of $Ba_{0.0625}Bi_{0.46875}Na_{0.46875}TiO_3$ and their volume dependence can be predicted. The composition is close to the systems MPB. Figure 5.8 compares the predicted α_A and α_B to calculated results. $Ba_{0.0625}Bi_{0.46875}Na_{0.46875}TiO_3$ has to be calculated in a larger supercell, which makes its calculation more time consuming. Therefore, only selected arrangements are calculated. The calculated α_i fit well to the predicted lines. This validates the method.

Figure 5.10 shows the predicted α_A and α_B as a function of $BaTiO_3$ concentration. The lattice parameter is not held fixed, but changes with composition. Two different scenarios for the variation of lattice parameters with $BaTiO_3$-concentration are used (also shown in Figure 5.9). In the first scenario the lattice parameters are based on experimental lattice parameters of the cubic phases. Cubic lattice parameters are used, because the cation site stabilities of the cubic perovskite phase are ana-
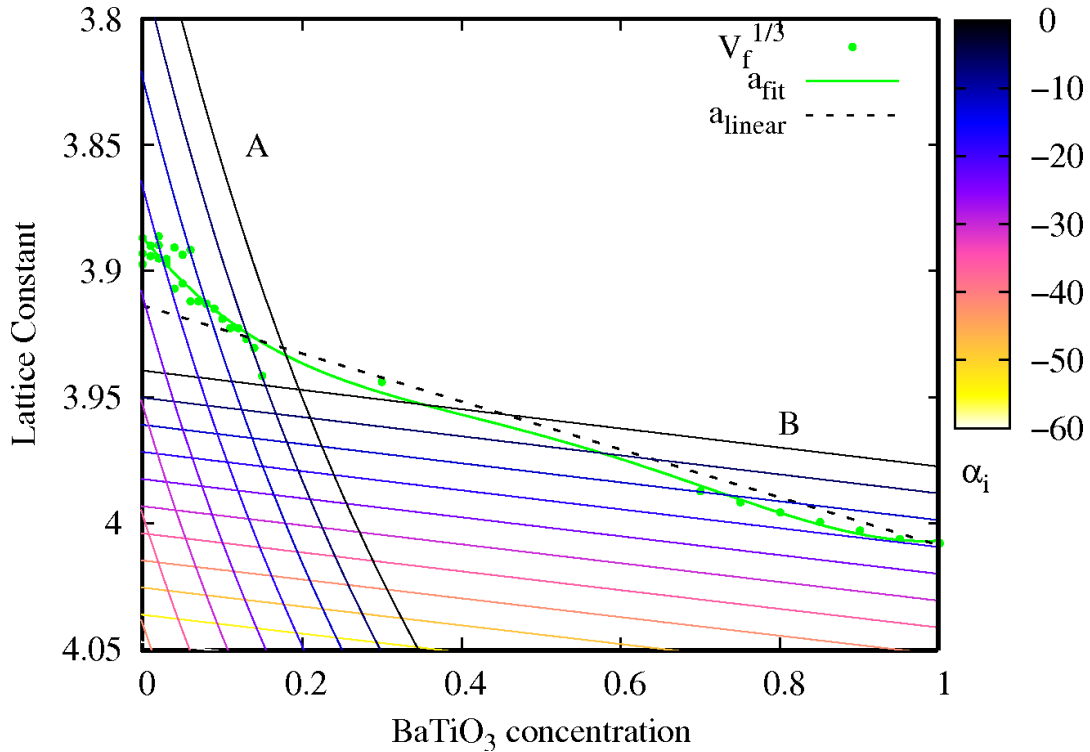
Figure 5.9: *Projection of the α_A and α_B dependence on the lattice concentration plane. Lines of same α_i are indicated in the color coding, positive values are omitted. Marked with a_{linear} is the linear interpolation between the cubic lattice parameters of the pure phases. Marked with $V_f^{1/3}$ is the cube root of experimentally obtained volumes at room temperature [66,132–134], a_{fit} denotes the fit of a polynomial of 4th grade to the $V_f^{1/3}$ data.*
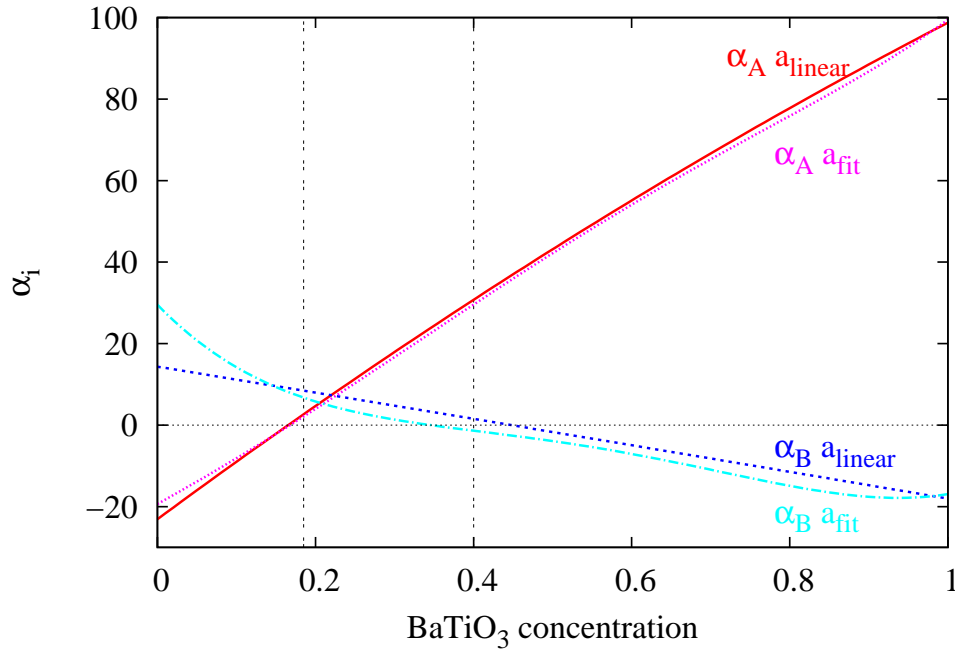
Figure 5.10: *α_i at lattice parameters changing with BaTiO$_3$ concentration. Dependence of the lattice parameters on the BT concentration a_{linear} and a_{fit} are marked in Figure 5.9.*

lyzed. For the pure phases experimental values of the lattice parameters of the cubic phase can be used. For the solid solution calculations the lattice parameters are taken from a linear interpolation according to Vegard's law, since an experimental lattice parameter of the cubic phase is only available for one other composition [133]. Ferroelectric activities α_i corresponding to these lattice parameters are denoted with a_{linear} marked in Figure 5.10. In the second scenario lattice parameters of the polar room temperature phases are used as an estimate for the lattice parameter of the pseudocubic phase [66,132–134]. Ferroelectric activities α_i corresponding to these lattice parameters are marked with a_{fit} in Figure 5.10.

5.3.2 Discussion

The most interesting region in Figure 5.7 and 5.9 is situated at low BaTiO$_3$-content and large volume. In this region, both cation sites are ferroelectrically active, according to the calculations. Experimentally, a large volume and low BaTiO$_3$-content cannot be realized easily in the BNT-BT solid solution, because pure BNT has a

smaller volume than $BaTiO_3$. However, this region might be accessible in strained epitaxial films.

Figure 5.10 shows calculated ferroelectric instabilities that are better comparable to experimental observations. In the figure the volume is changed with the $BaTiO_3$ concentration, as both parameters cannot be separated easily in experiments. Figure 5.10 can be divided into three regions: A BNT-rich region up to about 19 %$BaTiO_3$ in which an A-site instability is calculated. An intermediate region between 19 %$BaTiO_3$ and 34-43 %$BaTiO_3$, where the calculations show no ferroelectric instable cation. A $BaTiO_3$-rich region above 34-43 % $BaTiO_3$ that is predicted to be B-site active. The same trends are observed independent of whether a linear interpolation of the cubic lattice parameters or a fit to lattice parameters of the ferroelectric phase is used. For the A-site instability both approximations of the lattice parameter result in similar ferroelectric activities, while the B-site instability is more sensitive to the choice of the lattice parameter, especially in the BNT rich region.

In the $BaTiO_3$-rich region ($BaTiO_3$-content $>$ 34-40 %) the B-site becomes more instable with increasing $BaTiO_3$-content, while the A-site is clearly stable. Experimental work analyzing the structure of this concentration region showed a decrease of the Ti displacement with decreasing $BaTiO_3$ content to 85 % $BaTiO_3$ [134], which agrees with the presented results. Another finding of this experimental work was an increase of tetragonality with decreasing $BaTiO_3$-content, which is attributed to an effect of decrease in oxygen octahedral volume. A decreased oxygen octahedral volume is expected from the calculations. However, the tetragonality of the system is not analyzed. It has been suggested that the tetragonal distortion is stabilized by inter-atomic cooperation suppressed in the calculations [43].

In the compositional range between 19 %$BaTiO_3$ and 34-43 %$BaTiO_3$, no ferroelectrically active cation is found. However, the stability of the B-site cations is not as pronounced as the A-site stability in the $BaTiO_3$-rich region. As experimental studies identify the material as tetragonal at 30 % BT [133], it is assumed that tetragonality is stabilized by inter-atomic cooperation [43].

Ferroelectrically most active is the BNT-rich region ($BaTiO_3$-content $<$ 19 %). Here, the B-site is slightly stabilized, while the A-site is clearly instable. The ferroelectric activity of the B-site is small in the entire solid solution. Thus, the site is either slightly ferroelectric active or slightly stabilized. It is assumed that interatomic cooperation might further activate the B-sites. Such an activation is most likely in the BNT rich region, because the A-site is clearly active.

It has been postulated in literature that chemical substitution can be regarded as introduction of a chemical pressure, equivalent to an external hydrostatic pressure [24] (see Section 1.2.1). In the case of BNT-BT it has been proposed that the introduction of a larger cation on the A-site, i.e. Ba^{2+} replacing Bi^{3+} and Na^+,

can be described as negative (tensile) chemical pressure [24]. Transferring this idea to the presented calculations, hydrostatic pressure can be obtained from volume changes at fixed $BaTiO_3$-concentrations, while chemical pressure can be obtained by changing volume and composition simultaneously (at the respective experimental volumes). Therefore, since negative hydrostatic pressure (increased volume) results in an enhanced ferroelectric activity, one could postulate that the same is true for negative chemical pressure (addition of $BaTiO_3$). The presented observations of the B-site stability support this hypothesis, as B-site cations become less stable at both negative hydrostatic pressure (large volumes in Figure 5.5) and negative chemical pressure (high $BaTiO_3$-content in Figure 5.10). However, the A-site stability shows a more complex behavior, as A-site cations are destabilized at negative hydrostatic pressure (large volumes in Figure 5.5) but stabilized at negative chemical pressure (high $BaTiO_3$-content in Figure 5.10).

In this thesis the discrepancy is explained by attributing the chemical pressure to two effects. First, there exists a misfit effect due to different ionic radii of the substituted cations. Second, a change in the local moduli occurs due to the different chemical bondings, resulting from different polarizabilities, electronegativities or ionic compressibilities of the cations. The different cation sites show different dependence on the misfit and modulus effect.

The activity of the A-site is sensitive to the misfit effect, but depends more on the modulus effect. The force constants acting on the A-site cation mainly result from A-O interactions. With chemical substitution, the character of the A–O bonds changes. When the two small cations, hard ionic Na^+ and soft polarizable Bi^{3+}, are replaced by the large hard ionic Ba^{2+}-cations, A-O hybridization (mainly Bi-O) is reduced with increasing $BaTiO_3$-content.

On the other hand, the activity of the B-site is strongly sensitive to the misfit effect, but shows only a weak modulus effect. The latter can be explained by an indirect substitution effect on Ti–O bonds. As the A–O bonds change their character from partly covalent to purely ionic with increasing $BaTiO_3$-content, the effective electronegativity of oxygen changes and hence Ti–bonds can only indirectly "sense" the chemical A-site substitution.

To summarize, the changes of ferroelectric cation site activity with chemical substitution are determined by a superposition of both effects. The misfit effect influences mainly the ferroelectric B-site activity, while the modulus effect dominates the ferroelectric activity of the A-site.

5.4 Summary and conclusions

Ferroelectric instabilities of both cation sites were analyzed in the lead-free perovskite solid solution system BNT-BT, which is a mixture of the B-site ferroelectric BaTiO$_3$ and the A-site ferroelectric BNT.

The instabilities of the cation sites can be quantified as a function of volume and composition using DFT calculations. Linear relations to both the lattice constant and BaTiO$_3$ concentration are found. The experimental composition of the MPB lies within the region of BaTiO$_3$-content of less than 20 %. In this composition region the A-site is unstable, while the B-site is only slightly stabilized and might be activated by inter-sublattice cooperation.

The correlation of ferroelectric activity to volume and concentration is explained by the superposition of a misfit and a modulus effect. The misfit effect results from different ionic radii of Na/Bi and Ba, while the modulus effect has its origin in the different chemical properties of these cations (polarizability, electronegativity, ionic compressibility). The ferroelectric B-site activity is dominated by the misfit effect, leading to its increase upon BT-addition. The ferroelectric A-site activity is dominated by the modulus effect suppressing the A-site displacements upon increasing BT-content.

Efficient stability calculations of the BNT-BT solid solution could be used to identify a concentration region in which improved ferroelectricity is expected. In this region, in which the MPB is also situated, one cation site is active, while the other is only slightly stabilized. It remains to be seen whether this technique is transferable to other systems, where it could be used to identify interesting composition ranges in new solid solutions showing enhanced ferroelectric properties.

Conclusion

In this thesis the structure and stability of different ferroelectric perovskite materials was analyzed, using atomistic computer simulation. The aim was to improve the understanding of lead-free ferroelectrics and their differences to $PbZr_{1-x}Ti_xO_3$ (PZT), to help in the search for new ferroelectric materials.

Cation order and relaxation possibilities were analyzed in the cubic structure of homovalent PZT, qualitatively comparing configurations in different supercells and quantitatively within a specific supercell. The thermodynamics of cubic PZT were assessed from first-principles to validate the assumption of a fully miscible solid solution with positive heat of mixing in the paraelectric regime.

The favored chemical order is the result of the size difference between Ti and Zr octahedra, and cation relaxation. The size effect can be quantified by simple model calculations and was found to favor a rocksalt order of the B-site cations. The influence of relaxation possibilities is reflected in the formation of Ti {110} planes. These planes introduce an asymmetry, that allows for cation relaxation and subsequent energy gain. The formation of {110} planes can only be observed in large supercells with less symmetry constraints. Monte-Carlo (MC) calculations indicated that even at elevated temperatures the favoring of ordered structures is not overcome by entropy.

According to the calculations B-site cation arrangement of PZT in thermodynamic equilibrium is characterized by {111} patterns and {110} Ti-planes. However, the driving force towards one particular order is very small, and cation diffusion is kinetically hindered in perovskite materials. Thus, in PZT bulk materials ordered regions will most likely be too small to be observed. Under enhanced diffusion and additional forces favoring a particular ordering, e.g. in epitaxial films, chemical order can be observed.

The cation order in heterovalent $(Na_{1/2}Bi_{1/2}TiO_3)_{1-x}$-$(BaTiO_3)_x$ (BNT-BT) was analyzed for $Na_{1/2}Bi_{1/2}TiO_3$ (BNT) and BNT-BT close to the morphotropic region, combining electrostatic calculations, density functional theory (DFT) calculations and experimental transmission electron microscopy (TEM) imaging.

The results indicate, that the crystallographic A-sites in BNT-BT are homogeneously occupied. However, it is possible that local ordering occurs, while the overall distribution of A-site atoms is homogeneous. Samples analyzed by high resolution transmission electron microscopy (HRTEM) consist of regions that show different orientation, possibly due to slightly different structures.

The ferroelectric instability of the BNT-BT system was analyzed by investigating the stability of both cation sites. The influences of composition and volume were analyzed modeling a homogeneous A-site occupation as seen for BNT-BT mentioned above.

The presented DFT calculations confirmed $BaTiO_3$ to be a B-site active ferroelectric, while BNT is an A-site active ferroelectric. Calculations of the mixture quantify the instabilities of the cation sites as a bilinear function of the lattice constant and $BaTiO_3$ concentration.

In this thesis the correlation of ferroelectric activity to volume and concentration is explained by the superposition of a misfit and a modulus effect. The misfit effect was found to result from different ionic radii of Na/Bi and Ba, while the modulus effect has its origin in the different chemical properties of these cations (polarizability, electronegativity, ionic compressibility). The ferroelectric B-site activity is dominated by the misfit effect leading to an increase upon BT-addition. The ferroelectric A-site activity is instead dominated by the modulus effect suppressing the A-site displacements upon increasing BT-content.

The calculations show the composition of the morphotropic phase boundary (MPB) within a concentration region which is characterized by an unstable A-site and an only slightly stabilized B-site that might be activated by inter-sublattice cooperation. This work demonstrates that efficient stability calculations of the BNT-BT solid solution can be used to narrow the concentration region showing improved ferroelectricity.

Ferroelectric instability calculations are a very promising tool for the prediction of materials with strong ferroelectric behavior and should be further analyzed. The method could be further refined on the BNT-BT system allowing for interatomic cooperation. It could be tested, whether the B-site becomes instable when the A-site is instable close to the morphotropic region, as proposed in this thesis. Additional effects might also be observed.

In addition cation site stability calculations could be used to screen material systems for ferroelectric activity. The proposed method is simple enough to be used on a variety of material system, while gathering useful information on the whole system analyzed. Cation site stability calculations could mainly be used to identify the traits of the morphotropic region of a material system or an otherwise preferred material composition. In this work the morphotropic region of BNT-BT coincides with an area that is active in one site and possible to be activated in the other site. As the morphotropic region of PZT also shows this behavior, it could be theorized that this is the characteristic trait of the morphotropic region. Different ferroelectric material systems could be analyzed to test that theory.

Contributions

The results presented in section 4.1 which were published in one article [128], originate from a joint project and include data from M. Gröting. M. Gröting contributed the DFT results, while my contributions include the electrostatic calculations. The interpretation of the data was done in close cooperation.

The results presented in section 4.3 which were published in one article [129], originate from a joint project and include data from J. Kling. J. Kling contributed the experimental and simulated HRTEM images, while my contributions include the configurations, which were used by J. Kling to perform HRTEM image simulations. Also here, the interpretation of the data was done in close cooperation.

Acknowledgements - Danksagung

An dieser Stelle möchte ich mich bei allen bedanken, die zum Gelingen dieser Arbeit beigetragen haben.

Zuerst gilt mein Dank Prof. Karsten Albe, der es mir ermöglicht hat, im Rahmen des Projekts C1 im SFB 595 diese Arbeit anzufertigen und mich während dieser Zeit betreut hat. Des Weiteren bedanke ich mich bei Prof. Rödel für sein Interesse an meiner Arbeit und der Übernahme des Zweitgutachtens.

Als nächstes bedanke ich mich bei Melanie Gröting für Diskussionen über Ferroelektrika, deren Simulation und für die gemeinsame Arbeit an Publikationen. Bei Dr. Jens Kling bedanke ich mich für die gemeinsame Arbeit zur Ordnung in BNT6BT, für die HRTEM Simulationen meiner Strukturen und die gemeinsame Arbeit an einer verbindenden Publikation. Bei Prof. Kleebe bedanke ich mich für die Unterstützung dieser Publikation. Ein weiterer Dank geht an Dr. Torsten Granzow, dessen Vorlesung mein Interesse an Ferroelektrika geweckt hat.

Außerdem bedanke ich mich bei Dr. Peter Ágoston für Diskussionen zur Modellierung von Oxiden, bei Johan Pohl für seine Hilfe bei Monte Carlo Simulationen und Cluster Expansion und bei Dr. Paul Erhart, der mich an die DFT herangeführt hat. Für hilfreiche Kommentare zu Publikationen danke ich Dr. Yvonne Ritter und Manuel Diehm, bei dem ich mich auch für technische Unterstützung bedanke. Für Hilfe bei der englischen Sprache und wissenschaftlicher Ausdrucksweise bedanke ich mich bei Christine Hayn.

Bei den Kollegen der Materialmodellierung, des zweiten Stocks im CSI Gebäude und des SFB's bedanke ich mich für die angenehme Arbeitsatmosphäre und gemeinsam verbrachte Freizeit. Ganz besonders bedanke ich mich bei meiner Familie und meinen Freunden für die Hilfe und Unterstützung.

Thank you for your interest in my topic and support to Dr. Wook Jo. For technical support a thank you to Dr. Jani Kotakoski and Dr. Antti Tolvanen whom I also thank for his clear comments helping my understanding of DFT.

Disclaimer - Erklärung

Die vorliegende Arbeit wurde im Zeitraum von Januar 2008 bis Juli 2012 im Fachgebiet Materialmodellierung am Institut für Materialwissenschaft der Technischen Universität Darmstadt bei Herrn Prof. Dr. rer. nat. Karsten Albe angefertigt.

Hiermit versichere ich an Eides statt, dass ich die vorliegende Arbeit selbstständig und nur unter Verwendung der angegebenen Hilfsmittel angefertigt habe. Von mir wurde bisher weder an der Technischen Universität Darmstadt noch an einer anderen Hochschule ein Promotionsversuch unternommen.

Darmstadt, den 28.09.2013

Silke Hayn

Curriculum Vitae

Der Lebenslauf ist in der Online-Verison aus Gründen des Datenschutzes nicht enthalten.

Publications based on this dissertation

M. Gröting, S. Hayn, K. Albe, *Chemical order and local structure of the lead-free relaxor ferroelectric $Na_{1/2}Bi_{1/2}TiO_3$*, J. Solid State Chem. 184, 2041 (2011)

J. Kling, S. Hayn, L. Schmitt, M. Gröting, H.-J. Kleebe and K. Albe, *A-site occupancy in the lead-free $(Bi_{1/2}Na_{1/2}TiO_3)_{0.94}(BaTiO_3)_{0.06}$ piezoceramic: Combining first-principles study and TEM* J. Appl. Phys. 107, 114113 (2010)

S. Hayn, M. Gröting and K. Albe, *Thermodynamic and structural properties of lead-free ferro-electric materials: First-principles calculations on $Bi_{0.5}Na_{0.5}TiO_3$ and $(Bi_{0.5}Na_{0.5}TiO_3)_{0.94}$-$(BaTiO_3)_{0.06}$* Electroceramics XII Trondheim 2010, Talk

S. Hayn, M. Gröting and K. Albe, *Lead-free ferroelectric solid solutions from first-principles calculations* DPG Frühjahrestagung Sektion Kondensierte Materie Dresden 2009, Talk

Acronyms

ABINIT suite of programs implementing density functional theory

CASM Cluster-Assisted Statistical Mechanics

GULP General Utility Lattice Program

VASP Vienna ab-initio simulation package

BNT $Na_{1/2}Bi_{1/2}TiO_3$

BNT-BT $(Na_{1/2}Bi_{1/2}TiO_3)_{1-x}$-$(BaTiO_3)_x$

BNT6BT $(Na_{1/2}Bi_{1/2}TiO_3)_{0.94}$-$(BaTiO_3)_{0.06}$

DFT density functional theory

f.u. formula units

GGA generalized gradient approximation

HGH Hartwigsen-Goedecker-Hutter

HRTEM high resolution transmission electron microscopy

KNN $Na_{1-x}K_xNbO_3$

LDA local density approximation

MC Monte Carlo

MD Molecular dynamics

MPB morphotropic phase boundary

PAW projector augmented wave

PZT $PbZr_{1-x}Ti_xO_3$

TEM transmission electron microscopy

VCA virtual crystal approximation

Bibliography

[1] R. Resta and D. Vanderbilt. *Physics of Ferroelectrics A Modern Perspective; Theory of Polarisation: A Modern Approach*. Springer, 2007.

[2] A. E. Crawford. Lead zirconate-titanate piezoelectric ceramics. *Br. J. Appl. Phys.*, 12:529–534, 1961.

[3] J. Rödel, W. Jo, K. Seifert, E.-M. Anton, T. Granzow, and D. Damjanovic. Perspective on the development of lead-free piezoceramics. *J. Am. Ceram. Soc.*, 92(6):1153–1177, 2009.

[4] C. Kittel. *Einführung in die Festkörperphysik*. Oldenbourg Verlag München Wien, 2002.

[5] R. Resta. Macroscopic polarization in crystalline dielectrics: The geometric phase approach. *Rev. Mod. Phys.*, 66:899, 1994.

[6] M. Dove. Theory of displacive phase transitions in minerals. *Am. Mineral.*, 82:213, 1997.

[7] M. Knapp and P. Woodward. A-site cation ordering in AA'BB'O_6 perovskites. *J. Solid State Chem.*, 179(4):1076–1085, April 2006.

[8] B. Jaffe, W. R. Cook, and H. Jaffe. *Piezoelectric Ceramics*. Academic Press Limited, 1971.

[9] V. M. Goldschmidt. *Mat.-Natur*, 2:7, 1926.

[10] A. D. Bruce and R.A. Cowley. *Structural Phase Transitions*. Taylor and Francis, London, 1981.

[11] J. M. Yeomans. *Statistical mechanics of phase transitions*. Clarendon Press (Oxford), 1992.

[12] S. Radescu, I. Etxebarria, and J. M. Perez-Mato. The Landau free energy of the 3-dimensional Φ^4 model in wide temperature intervals. *J. Phys. Condens. Matter*, 7, 1995.

[13] Y. Yamada, G. Shirane, and A. Linz. Study of critical fluctuations in $BaTiO_3$ by neutron scattering. *Phys. Rev.*, 177:848, 1969.

[14] G. Shirane. Neutron scattering studies of structural phase transitions at brookhaven. *Rev. Mod. Phys.*, 46:437, 1974.

[15] R. Resta. Ab initio simulation of the properties of ferroelectric materials. *Modell. Simul. Mater. Sci. Eng.*, 11(4):R69, 2003.

[16] D. Berlincourt, H. H. A. Krueger, and B. Jaffe. Stability of phases in modified lead zirconate with variation in pressure, electric field, temperature and composition. *J. Phys. Chem. Solids*, 25(7):659–674, July 1964.

[17] M. Ahart, M. Somayazulu, R. E. Cohen, P. Ganesh, P. Dera, H. Mao, R. Hemley, Y. Ren, P. Liermann, and Z. Wu. Origin of morphotropic phase boundaries in ferroelectrics. *Nature*, 451(7178):545–548, January 2008.

[18] P. Ari-Gur and L. Benguigui. X-ray study of the PZT solid solutions near the morphotropic phase transition. *Solid State Commun.*, 15:1077, 1974.

[19] S. A. Mabud. The morphotropic phase boundary in PZT solid solutions. *J. Appl. Crystallogr.*, 13:211, 1980.

[20] K. Schönau, L. Schmitt, M. Knapp, H. Fuess, R. Eichel, H. Kungl, and M. Hoffmann. Nanodomain structure of Pb[$Zr_{1-x}Ti_x$]O_3 at its morphotropic phase boundary: Investigations from local to average structure. *Phys. Rev. B*, 75:184117, 2007.

[21] K. Rabe, M. Dawber, C. Lichtensteiger, C. Ahn, and J.-M. Triscone. *Physics of Ferroelectrics A Modern Perspective; Essential Background*. Springer, 2007.

[22] D. Damjanovic. A morphotropic phase boundary system based on polarization rotation and polarization extension. *Appl. Phys. Lett.*, 97(6):062906–3, August 2010.

[23] Y. L. Wang, Z. M. Cheng, Y.-R. Sun, and X.-H. Dai. Phase transition study of PZT 95/5 ceramics. *Physica B+C*, 150(1-2):168–174, May 1988.

[24] S. Trujillo, J. Kreisel, Q. Jiang, J. H. Smith, P. A. Thomas, P. Bouvier, and F. Weiss. The high-pressure behaviour of Ba-doped $Na_{1/2}Bi_{1/2}TiO_3$ investigated by Raman spectroscopy. *J. Phys. Condens. Matter*, 17(41):6587, 2005.

[25] G. King and P. Woodward. Cation ordering in perovskites. *J. Mater. Chem.*, 20(28):5785–5796, 2010.

[26] N. Setter and L. E. Cross. The role of B-site cation disorder in diffuse phase transition behavior of perovskite ferroelectrics. *J. Appl. Phys.*, 51(8):4356–4360, August 1980.

[27] B. P. Burton, R. P. McCormack, B. H. Toby, and E. K. Goo. Cation ordering in some ABO_3 perovskites. *Ferroelectrics*, 194(1):187–206, 1997.

[28] R. Liu, Y. Xuan, and Y. Q. Jia. A Simple Method for Judging Order or Disorder inA(B′B″)O$_3$ Perovskite Compounds. *J. Solid State Chem.*, 134(2):420–422, December 1997.

[29] L. Bellaiche and David Vanderbilt. Electrostatic model of atomic ordering in complex perovskite alloys. *Phys. Rev. Lett.*, 81(6):1318–, August 1998.

[30] B.P. Burton. Long-range versus short-range interactions and the configurational energies of Ba(B,B′)O$_3$ and Pb(B,B′)O$_3$ perovskites. *Modell. Simul. Mater. Sci. Eng.*, 8(3):211, 2000.

[31] S.-E. Park, S.-J. Chung, I.-T. Kim, and K. S. Hong. Nonstoichiometry and the Long-Range Cation Ordering in Crystals of (Na$_{1/2}$Bi$_{1/2}$) TiO$_3$. *J. Am. Ceram. Soc.*, 77(10):2641–2647, 1994.

[32] P. Erhart and K. Albe. Thermodynamics of mono- and di-vacancies in barium titanate. *J. Appl. Phys.*, 102:084111, 2007.

[33] M. S. Islam. Ionic transport in ABO(3) perovskite oxides: a computer modelling tour. *J. Mater. Chem.*, 10:1027, 2000.

[34] A. Kingon and B. Clark. Sintering of PZT Ceramics: I, Atmosphere Control. *J. Am. Ceram. Soc.*, 66(4):253–256, 1983.

[35] G. Gottstein. *Physikalische Grundlagen der Materialkunde*. Springer, 2001.

[36] S. Ghose. Lattice dynamics, phase transitions and soft modes. *Rev. Mineral. Geochem.*, 14:127, 1985.

[37] R. E. Cohen and H. Krakauer. Lattice dynamics and origin of ferroelectricity in BaTiO$_3$: Linearized-augmented-plane-wave total-energy calculations. *Phys. Rev. B*, 42(10):6416, October 1990.

[38] Ph. Ghosez, X. Gonze, and J. P. Michenaud. Lattice dynamics and ferroelectric instability of barium titanate. *Ferroelectrics*, 194(1):39–54, 1997.

[39] P.Sc. H. Ghosez, X. Gonze, and J. P. Michenaud. Ab-initio initio phonon dispersion curves and interatomic force constants of barium titanate. *Ferroelectrics*, 206(1):205–217, 1998.

[40] H. Krakauer, R. Yu, and C.-Z. Wang. Wavevector dependence of ferroelectric instabilities in KNbO$_3$. *J. Phys. Chem. Solids*, 57(10):1409–1412, October 1996.

[41] Ph. Ghosez, E. Cockayne, U. V. Waghmare, and K. M. Rabe. Lattice dynamics of BaTiO$_3$, PbTiO$_3$, and PbZrO$_3$: A comparative first-principles study. *Phys. Rev. B*, 60(2):836–, July 1999.

[42] S. V. Halilov, M. Fornari, and D. J. Singh. Lattice instabilities in $(Pb,Cd)TiO_3$ alloys. *Appl. Phys. Lett.*, 81(18):3443–3445, October 2002.

[43] M. Ghita, M. Fornari, D. J. Singh, and S. V. Halilov. Interplay between A-site and B-site driven instabilities in perovskites. *Phys. Rev. B*, 72(5):054114–, August 2005.

[44] P. Muralt. Ferroelectric thin films for micro-sensors and actuators: a review. *J. Micromech. Microeng.*, 10:136, 2000.

[45] Eu-directive 2002/95/ec: Restriction of the use of certain hazardous substances in electrical and electronic equipment (rohs),. *Off. J. Eur. Union*, 46, 2003.

[46] B. Noheda, J. A. Gonzalo, L. E. Cross, R. Guo, S.-E. Park, D. E. Cox, and G. Shirane. Tetragonal-to-monoclinic phase transition in a ferroelectric perovskite: The structure of $PbZr_{0.52}Ti_{0.48}O_3$. *Phys. Rev. B*, 61:8687, 2000.

[47] A. M. Glazer, P. A. Thomas, K. Z. Baba-Kishi, G. K. H. Pang, and C. W. Tai. Influence of short-range and long-range order on the evolution of the morphotropic phase boundary in $Pb(Zr_{1-x}Ti_x)O_3$. *Phys. Rev. B*, 70:184123, 2004.

[48] J. Frantti. Notes of the recent structural studies on lead zirconate titanate. *J. Phys. Chem. B*, 112(21):6521, May 2008.

[49] F. Cordero, F. Trequattrini, F. Craciun, and C. Galassi. Octahedral tilting, monoclinic phase and the phase diagram of pzt. *J. Phys.: Condens. Matter*, 23:415901, 2011.

[50] R. Schierholz and H. Fuess. Symmetry of domains in morphotropic $PbZr_{1-x}Tix O_3$ ceramics. *Phys. Rev. B*, 84:064122, 2011.

[51] M. Deluca, H. Fukumura, N. Tonari, C. Capiani, N. Hasuike, K. Kisoda, C. Galassi, and H. Harima. Raman spectroscopic study of phase transitions in undoped morphotropic $PbZr_{1-x}Ti_xO_3$. *J. Raman Spectrosc.*, 42:488, 2011.

[52] I. Grinberg and A. M. Rappe. Silver solid solution piezoelectrics. *Appl. Phys. Lett.*, 85(10):1760–1762, September 2004.

[53] I. Kornev, L. Bellaiche, P. Bouvier, P.-E. Janolin, B. Dkhil, and J. Kreisel. Ferroelectricity of perovskites under pressure. *Phys. Rev. Lett.*, 95(19):196804–, October 2005.

[54] P. Ganesh and R. E. Cohen. Pressure induced phase transitions in $PbTiO_3$. *J. Phys.: Condens. Matter*, 21:064225, 2009.

[55] P.-E. Janolin, P. Bouvier, J. Kreisel, P. A. Thomas, I. A. Kornev, L. Bellaiche, W. Crichton, M. Hanfland, and B. Dkhil. High-Pressure Effect on $PbTiO_3$: An Investigation by Raman and X-Ray Scattering up to 63 GPa. *Phys. Rev. Lett.*, 101(23):237601–, December 2008.

[56] L. C. Zhang, A. L. Vasiliev, I. B. Misirlioglu, R. Ramesh, S. P. Alpay, and M. Aindow. Cation ordering in epitaxial lead zirconate titanate films. *Appl. Phys. Lett.*, 93:262903, 2008.

[57] G. Sághi-Szabó and R. Cohen. Long-range order effects in $Pb(Zr_{1/2}Ti_{1/2})O_3$. *Ferroelectrics*, 194:287, 1997.

[58] V. I. Zinenko and S. N. Sofronova. Statistical mechanics of cation ordering and lattice dynamics of $PbZr_x Ti1 - xO_3$ solid solutions. *Phys. Solid State*, 46:1291, 2004.

[59] L. Bellaiche, Alberto García, and David Vanderbilt. Finite-Temperature Properties of $Pb(Zr_{1-x}Ti_x)O_3$ Alloys from First Principles. *Phys. Rev. Lett.*, 84:5427, 2000.

[60] A. M. George, J. Íñiguez, and L. Bellaiche. Effects of atomic short-range order on the properties of perovskite alloys in their morphotropic phase boundary. *Phys. Rev. Lett.*, 91:045504, 2003.

[61] G. Rossetti, Jr., W. Zhang, and A. Khachaturyan. Phase coexistence near the morphotropic phase boundary in lead zirconate titanate ($PbZrO_3$-$PbTiO_3$) solid solutions. *Appl. Phys. Lett.*, 88:072912, 2006.

[62] L.S. Palatnik and A.I. Landau. *Phase equilibria in multicomponent systems*. Holt, Rinehart and Winston, Inc, 1964.

[63] M. Rane, A. Navrotsky, and G. Rossetti. Enthalpies of Formation of Lead Zirconate Titanate (PZT) Solid Solutions. *J. Solid State Chem.*, 161:402, 2001.

[64] K.T. Jacob and L. Rannesh. Thermodynamic activities in the $Pb(Zr_{1-X}Ti_X)O_3$ solid solution at 1373 K. *Mater. Sci. Eng., B*, 140:53, 2007.

[65] T. Takenaka, K. Maruyama, and K. Sakata. $(Bi_{1/2}Na_{1/2})TiO_3$-$BaTiO_3$ System for Lead-Free Piezoelectric Ceramics. *Jpn. J. Appl. Phys.*, 30:2236–2239, 1991.

[66] W. Jo, J. Daniels, J. Jones, X. Tan, P. Thomas, D. Damjanovic, and J. Rödel. Evolving morphotropic phase boundary in lead-free $(Bi_{1/2}Na_{1/2})TiO_3$–$BaTiO_3$ piezoceramics. *J. Appl. Phys.*, 109:014110, January 2011.

[67] G. O. Jones and P. A. Thomas. Investigation of the structure and phase transitions in the novel A-site substituted distorted perovskite compound $Na_{0.5}Bi_{0.5}TiO_3$. *Acta Crystallogr. Section B*, 58(2):168–178, 2002.

[68] Y. Hiruma, H. Nagata, and T. Takenaka. Formation of Morphotropic Phase Boundary and Electrical Properties of $(Bi_{1/2}Na_{1/2})TiO_3$-$Ba(Al_{1/2}Nb_{1/2})O_3$ Solid Solution Ceramics. *Jpn. J. Appl. Phys.*, 48:09KC08, September 2009.

[69] V. Dorcet and G. Trolliard. A transmission electron microscopy study of the A-site disordered perovskite $Na_{0.5}Bi_{0.5}TiO_3$. *Acta Mater.*, 56(8):1753–1761, May 2008.

[70] R. E. Cohen. Origin of ferroelectricity in perovskite oxides. *Nature*, 358(6382):136–138, July 1992.

[71] Y.-M. Chiang, G. Farrey, and A. Soukhojak. Lead-free high-strain single-crystal piezoelectrics in the alkaline–bismuth–titanate perovskite family. *Appl. Phys. Lett.*, 73(25):3683–3685, December 1998.

[72] B. Chu, D. Chen, G.g Li, and Q. Yin. Electrical properties of $Na_{1/2}Bi_{1/2}TiO_3$-$BaTiO_3$ ceramics. *J. Eur. Ceram. Soc.*, 22(13):2115–2121, December 2002.

[73] R. Ranjan and A. Dviwedi. Structure and dielectric properties of $(Na_{0.50}Bi_{0.50})_{1-x}Ba_xTiO_3$: $0 <= x <= 0.10$. *Solid State Commun.*, 135(6):394–399, August 2005.

[74] Q. Xu, S. Chen, W. Chen, S. Wu, J. Lee, J. Zhou, H. Sun, and Y. Li. Structure, piezoelectric properties and ferroelectric properties of $(Na_{0.5}Bi_{0.5})_{1-x}Ba_xTiO_3$ system. *J. Alloys Compd.*, 381(1-2):221–225, November 2004.

[75] S.-T. Zhang, A. Kounga, E. Aulbach, and Y. Deng. Temperature-Dependent Electrical Properties of $0.94Bi_{0.5}Na_{0.5}TiO_3 0.06BaTiO_3$ Ceramics. *J. Am. Ceram. Soc.*, 91(12):3950–3954, 2008.

[76] P.K. Davies, H. Wu, A.Y. Borisevich, I.E. Molodetsky, and L. Farber. Crystal chemistry of complex perovskites: New cation-ordered dielectric oxides. *Annual Review of Materials Research*, 38(1):369–401, 2008.

[77] G. Trolliard and V. Dorcet. Reinvestigation of Phase Transitions in $Na_{0.5}Bi_{0.5}TiO_3$ by TEM. Part II: Second Order Orthorhombic to Tetragonal Phase Transition. *Chem. Mater.*, 20(15):5074–5082, July 2008.

[78] B. P. Burton and E. Cockayne. Prediction of the $[Na_{1/2}Bi_{1/2}]TiO_3$ ground state. In *AIP Conf. Proc.*, volume 582, pages 82–90, Williamsburg, Virginia (USA), August 2001. AIP.

[79] Y. N. Xu and W. Y. Ching. Electronic structure of $(Na_{1/2}Bi_{1/2})TiO_3$ and its solid solution with $BaTiO_3$. *Philos. Mag. B*, 80:1141–1151, June 2000.

[80] R. E. Eitel, T. R. Randall, C. A.and Shrout, P. W. Rehrig, Hackenberger W., and S. Park. New High Temperature Morphotropic Phase Boundary Piezoelectrics Based on $Bi(Me)O_3$ - $PbTiO_3$ Ceramics. *Jpn. J. Appl. Phys*, 40:5999–6002, 2001.

[81] R. E. Eitel, S. J. Zhang, T. R. Shrout, C. A. Randall, and I. Levin. Phase Diagram of the Perovskite System (1 - x)$BiScO_3$-x$PbTiO_3$. *J. Appl. Phys.*, 96(5):2828–2831, September 2004.

[82] M. R. Suchomel and P. K. Davies. Predicting the position of the morphotropic phase boundary in high temperature $PbTiO_3$ - $Bi(B'B'')O_3$ based dielectric ceramics. *J. Appl. Phys.*, 96(8):4405–4410, October 2004.

[83] P. Baettig, C.F. Schelle, R. LeSar, U.V. Waghmare, and N.A. Spaldin. Theoretical prediction of new high-performance lead-free piezoelectrics. *Chem. Mater.*, 17(6):1376–1380, 2005.

[84] J. Íñiguez, D. Vanderbilt, and L. Bellaiche. First-principles study of $(BiScO_3)_{1-x}$ - $(PbTiO_3)_x$ piezoelectric alloys. *Phys. Rev. B*, 67(22):224107–, June 2003.

[85] I. Grinberg, M. R. Suchomel, P.r K. Davies, and A. M. Rappe. Predicting morphotropic phase boundary locations and transition temperatures in Pb- and Bi-based perovskite solid solutions from crystal chemical data and first-principles calculations. *J. Appl. Phys.*, 98:094111, 2005.

[86] W.-C. Lee, C.-Y. Huang, L.-K. Tsao, and Y.-C. Wu. Chemical composition and tolerance factor at the morphotropic phase boundary in $(Bi_{0.5}Na_{0.5})TiO_3$-based piezoelectric ceramics. *J. Eur. Ceram. Soc.*, 29(8):1443–1448, May 2009.

[87] K. Miura and T. Furuta. First-Principles Study of Structural Trend of $BiMO_3$ and $BaMO_3$: Relationship between Tetragonal or Rhombohedral Structure and the Tolerance Factors. *Jpn. J. Appl. Phys.*, 49(3):031501, 2010.

[88] J. Bennett, I. Grinberg, P. Davies, and A. Rappe. Pb-free ferroelectrics investigated with density functional theory: $SnAl_{1/2}Nb_{1/2}O_3$ perovskites. *Phys. Rev. B*, 83(14):144112–, April 2011.

[89] S. Hayn. Ab-initio calculations on lead-free piezoelectric materials. Diplomarbeit, Technische Universität Darmstadt, 2007.

[90] Michel Rappaz, Michel Bellet, and Michel Deville. *Numerical Modeling in Materials Science and Engineering*. Springer, 2003.

[91] Robert G. Parr and Weito Yang. *Density-Functional Theory of Atoms and Molecules*. Oxford Science Publications, 1989.

[92] D. M. Ceperley and B. J. Alder. Ground state of the electron gas by a stochastic method. *Phys. Rev. Lett.*, 45(7):566–, August 1980.

[93] D. Frenkel and B. Smit. *Understanding Molecular Simulation: From Algorithms to Applications*. Academic, New York, 1996.

[94] D. Landau and K. Binder. *A Guide to Monte Carlo Simulations in Statistical Physics*. Cambridge University Press, 2000.

[95] M. C. Payne, M. P. Teter, D. C. Allan, T. A. Arias, and J. D. Joannopoulos. Iterative minimization techniques for ab initio total-energy calculations: molecular dynamics and conjugate gradients. *Rev. Mod. Phys.*, 64(4):1045–, October 1992.

[96] P. Hohenberg and W. Kohn. Inhomogeneous electron gas. *Phys. Rev.*, 136(3B):B864, November 1964.

[97] W. Kohn and L. J. Sham. Self-consistent equations including exchange and correlation effects. *Phys. Rev.*, 140(4A):A1133, November 1965.

[98] J. P. Perdew and Y. Wang. Accurate and simple analytic representation of the electron-gas correlation energy. *Phys. Rev. B*, 45(23):13244–, June 1992.

[99] Carsten Rostgaard. The projector augmented-wave method. *arXiv:0910.1921v2 [cond-mat.mtrl-sci]*, Oct 2009.

[100] P. E. Blöchl. Projector augmented-wave method. *Phys. Rev. B*, 50(24):17953, December 1994.

[101] G. Kresse and J. Furthmüller. Efficient iterative schemes for ab initio total-energy calculations using a plane-wave basis set. *Phys. Rev. B*, 54:11169, 1996.

[102] K. Rabe and P. Ghosez. *Physics of Ferroelectrics A Modern Perspective; First-Principles Studies of Ferroelectric Oxides*. Springer, 2007.

[103] J. P. Perdew, K. Burke, and M. Ernzerhof. Generalized gradient approximation made simple. *Phys. Rev. Lett.*, 77(18):3865–, October 1996.

[104] Z. Wu and R.E. Cohen. More accurate generalized gradient approximation for solids. *Phys. Rev. B*, 73:235116, 2006.

[105] L. Nordheim. *Ann. Phys. Leipzigg*, 9:607, 1931.

[106] L. Bellaiche and David Vanderbilt. Virtual crystal approximation revisited: Application to dielectric and piezoelectric properties of perovskites. *Phys. Rev. B*, 61(12):7877–, March 2000.

[107] N. J. Ramer and A. M. Rappe. Virtual-crystal approximation that works: Locating a compositional phase boundary in $pb(zr_{1-x}ti_x)o_3$. *Phys. Rev. B*, 62(2):R743–, July 2000.

[108] X. Gonze, B. Amadon, P.-M. Anglade, J.-M. Beuken, F. Bottin, P. Boulanger, F. Bruneval, D. Caliste, R. Caracas, M. Cote, T. Deutsch, L. Genovese, Ph. Ghosez, M. Giantomassi, S. Goedecker, D.R. Hamann, P. Hermet, F. Jollet, G. Jomard, S. Leroux, M. Mancini, S. Mazevet, M.J.T. Oliveira, G. Onida, Y. Pouillon, T. Rangel, G.-M. Rignanese, D. Sangalli, R. Shaltaf, M. Torrent, M.J. Verstraete, G. Zerah, and J.W. Zwanziger. Abinit : First-principles approach of materials and nanosystem properties. *Computer Phys. Commun.*, 180:2582, 2009.

[109] K. Albe. Methoden der atomistischen computersimulation in der materialwissenschaft. Wahlpflichtvorlesung WS 2005/2006, 2005/2006.

[110] J.D. Gale. Empirical potential derivation for ionic materials. *Phil. Mag. B*, 73:3, 1996.

[111] M. S. Daw and M. I. Baskes. Embedded-atom method: Derivation and application to impurities, surfaces, and other defects in metals. *Phys. Rev. B*, 29:6443, 1984.

[112] X.Q. Hua, G.F. Xiea, and Y. Maa. A new optimization method for shell model interatomic potential parameters of perovskite ferroelectrics. *Physica B*, 405(11):2577, June 2010.

[113] S Tinte, M G Stachiotti, S R Phillpot, M Sepliarsky, D Wolf, and R L Migoni. Ferroelectric properties of $Ba_xSr_{1-x}TiO_3$ solid solutions obtained by molecular dynamics simulation. *J. Phys. Condens. Matter*, 16(20):3495, 2004.

[114] J.D. Gale. Gulp - a computer program for the symmetry adapted simulation of solids. *JCS Faraday Trans.*, 93:629, 1997.

[115] M. N. Rosenbluth A. H. Teller N. Metropolis, A. W. Rosenbluth and E. Teller. Equation of state calculations by fast computing machines. *J. Chem. Phys.*, 21:1087, 1953.

[116] I. Kornev, L. Bellaiche, P.-E. Janolin, B. Dkhil, and E. Suard. Phase Diagram of $Pb(Zr,Ti)O_3$ Solid Solutions from First Principles. *Phys. Rev. Lett.*, 97:157601, 2006.

[117] R. McCormack, M. Asta, D. de Fontaine, G. Garbulsky, and G. Ceder. hcp Ising model in the cluster-variation appriximation. *Phys. Rev. B*, 48:6767, 1993.

[118] A. Zunger, L. G. Wang, G. L. W. Hart, and M. Sanati. Obtaining Ising-like expansions for binary alloys from first principles. *Model. Simul. Mater.*, 10:685, 2002.

[119] J.M. Sanchez, F. Ducastelle, and D. Gratias. Generalized cluster description of multicomponent systems. *Physica A*, 128(1â2):334, November 1984.

[120] A. Gonis, X. G. Zhang, A. J. Freeman, P. Turchi, G. M. Stocks, and D. M. Nicholson. Configurational energies and effective cluster interactions in substitutionally disordered binary alloys. *Phys. Rev. B*, 36(9):4630–4646, September 1987.

[121] A. Van der Ven, J. C. Thomas, Qingchuan Xu, and J. Bhattacharya. Linking the electronic structure of solids to their thermodynamic and kinetic properties. *Mathematics and Computers in Simulation*, 80:1393, 2010.

[122] K. Sato, T. Miyanaga, S. Ikeda, and D. Diop. XAFS study of local structure change in perovskite titanates. *Phys. Scr.*, T115:359–361, 2005.

[123] R. V. Vedrinskii, E. S. Nazarenko, M. P. Lemeshko, V. Nassif, O. Proux, A. A. Novakovich, and Y. Joly. Temperature dependent XAFS studies of local atomic structure of the perovskite-type zirconates. *Phys. Rev. B*, 73(13):134109–, April 2006.

[124] G. Kresse and D. Joubert. From ultrasoft pseudopotentials to the projector augmented-wave method. *Phys. Rev. B*, 59:1758, 1999.

[125] F. D. Murnaghan. The compressibility of media under extreme pressures. *Proc Natl Acad Sci U S A*, 30(9):244, 1944.

[126] M. Cancarevic, M. Zinkevich, and F. Aldinger. Thermodynamic Assessment of the PZT System. *J. Ceram. Soc. Jpn.*, 114:937, 2006.

[127] G. A. Rossetti, Jr., A. G. Khachaturyan, G. Akcay, and Y. Ni. Ferroelectric solid solutions with morphotropic boundaries: Vanishing polarization anisotropy, adaptive, polar glass, and two-phase states. *J. Appl. Phys.*, 103:114113, 2008.

[128] M. Gröting, S. Hayn, and K. Albe. Chemical order and local structure of the lead-free relaxor ferroelectric NBT. *J. Solid State Chem.*, 184(8):2041–2046, August 2011.

[129] J. Kling, S. Hayn, L. Schmitt, M. Gröting, H.-J. Kleebe, and K. Albe. A-site occupancy in the lead-free $(Bi_{1/2}Na_{1/2}TiO_3)_{0.94}$–$(BaTiO_3)_{0.06}$ piezoceramic: Combining first-principles study and TEM. *J. Appl. Phys.*, 107(11):114113–5, June 2010.

[130] G. Haertling. Ferroelectric ceramics: History and technology. *J. Am. Ceram. Soc.*, 82(4):797–818, 1999.

[131] H. Monkhorst and J. Pack. Special points for brillouin-zone integrations. *Phys. Rev. B*, 13(12):5188–, June 1976.

[132] W. Ge, H. Liu, X. Zhao, X. Pan, T. He, D. Lin, H. Xu, and H. Luo. Growth and characterization of $Na_{0.5}Bi_{0.5}TiO_3$-$BaTiO_3$ lead-free piezoelectric crystal by the TSSG method. *J. Alloys Compd.*, 456(1-2):503–507, May 2008.

[133] J. Suchanicz, J. Kusz, H. Bohm, H. Duda, J. P. Mercurio, and K. Konieczny. Structural and dielectric properties of $(Na_{0.5}Bi_{0.5})_{0.70}Ba_{0.30}TiO_3$ ceramics. *J. Eur. Ceram. Soc.*, 23(10):1559–1564, September 2003.

[134] K. Datta, K. Roleder, and P. A. Thomas. Enhanced tetragonality in lead-free piezoelectric $(1-x)BaTiO_3$-$xNa_{1/2}Bi_{1/2}TiO_3$ solid solutions where $x = 0.05 < 0.40$. *J. Appl. Phys.*, 106:123512, 2009.